University of Cape Town
Department of Physics

MEASUREMENT OF NEUTRON RADIOTHERAPY SPECTRA IN A TISSUE-EQUIVALENT PHANTOM

Mark Herbert

Thesis submitted to the University of Cape Town for the degree of Master of Science

December 1997

ABSTRACT

A new technique was investigated for determining the changes in neutron radiotherapy spectra with position within a tissue-equivalent phantom at the National Accelerator Centre in the energy range 0 to 63 MeV. An deuterated liquid scintillator (NE230) was used as the neutron spectrometer for these measurements. The pulse height spectra measured using the NE230 scintillator were unfolded to give the neutron spectra. The results show beam hardening with depth into the phantom, which are consistent with other reported findings. The unfolding procedures used are described and the results of the tests performed to verify reliability are also presented and discussed.

DEDICATION

I dedicate this work to **ANZIL TRAUT**, **JANINE TRAUT** and **DESIREE' AFRICA**, who I met during the course of this work. My interaction with them have change my views about life.

ACKNOWLEDGEMENTS

I wish to express my sincere appreciation and gratitude to:

Professor F.D. Brooks, my supervisor, for his selfless assistance, untiring encouragement and support. Also, for giving me the opportunity to complete this work.

Andy Buffler for his help with the HEPRO analysis, which made the completion of this work possible.

The staff and students of the Physics Department, University Cape Town, in particular Dr Saalih Allie, Rudolf Nchodu, Dr. Loveness Kaunda and Mark Marais.

Dr Dan Jones, Julian Symons and Tim Fulcher and the staff of the National Accelerator Centre for their co-operation and use of their facilities.

To my mother, Babie, and father, Sitaar, for their encouragement, support and for giving me the opportunity to study.

My sisters Mandy and Norma, brothers, Tony and David, Amy and Callen for their support and encouragement.

To the rest of my family, especially my grandmother, uncles and aunts for their encouragement.

To the staff and pupils of St Andrew's High School with whom I shared many joyful and happy moments during the completion of this work, in particular, Mrs. P. Brandt, Mr. G. Adams, Enrico, Jerome, Charlton, Yolanda, Rashieda, Peter, Ricardo, Melanie, Claudia, Maddie, Muffin, Ed, Daniel and Priscilla.

To my friend Phillip De Kock for his help and encouragement.

UCT Bursary office for financial assistance.

CONTENTS

LIST OF TABLES

LIST OF FIGURES

CHAPTER 1

INTRODUCTION

1.1 NEUTRON RADIOTHERAPY

Soon after the discovery of ionizing radiation in 1895, it was recognised that this radiation produced different effects on normal biological tissue [Wi93]. It was therefore a natural development to investigate the effects of this radiation on superficial tumours (tumours affecting the surface only), i.e. the start of radiotherapy. Today, radiotherapy is mainly used in the treatment of malignant diseases for which there is no other effective form of treatment [Bo78]. It has been found that many malignant tumours in humans are relatively resistant to X-ray and gamma radiotherapy [Ra80]. Gray [Gr57] was first to suggest that the presence of hypoxic cells (cells without free oxygen) in the tumours may be the major cause for the radioresistance. One way of overcoming this problem is to use radiation which deposits more energy per unit path length, i.e. higher linear energy transfer (LET), in the treatment region than X-rays or gamma rays. The cheapest and most readily available of these high LET radiations are neutrons.

To understand the role which neutrons play in radiotherapy, we must first consider the biological effects they produce on animal or human tissue. The biological effects of radiation are a consequence of energy deposition and are LET dependent. Therefore, equal doses of radiation of different LET will not produce the same

biological effect. In order to compare the biological effects of radiation of different LET, a factor called the relative biological effectiveness (RBE), is used. The relative biological effectiveness is defined as:

$$RBE_i = \frac{d_A}{d_B} \qquad (1.1)$$

where: d_A = *dose of X-rays or gamma rays (200=300 keV) producing a certain biological effect; and*

d_B = *dose of radiation of type i producing the same biological effect.*

It has been found that RBE increases with increasing LET *[Ra80]*. In mammal cells, RBE values for neutrons lie in the range 2 to 4 *[Dy81]*, meaning that neutrons would produce greater biological effects than X-rays on human or animal tissue. From the work of Gray it was expected that the radiosensitivity of human or animal tissue would be affected by the presence of dissolved oxygen. This is known as the oxygen effect and is expressed in a parameter called the oxygen enhancement ratio (OER), defined as:

$$OER = \frac{O_a}{O_p} \qquad (1.2)$$

where: O_a = *dose for a given effect in absence of oxygen; and*

O_p = *dose for a given effect in the presence of oxygen.*

Tumours have oxygenated as well as hypoxic cells but the oxygenated cells are not as well oxygenated as normal tissue because of poor blood supply. The work of Catterall and Bewley *[Ca79]* demonstrated that neutrons produce good results in the treatment of the poorly-

oxygenated tumours. Neutron radiation may therefore offer more advantages than X-rays and gamma rays to control tumours.

Fast neutrons were first used in radiotherapy for treating patients by Stone *[St40]* between 1938 and 1943. The motivation for using fast neutrons in radiotherapy at that time was that neutrons appeared to produce greater biological damage per unit energy absorbed by tissue than X-rays. Therefore, it was hoped that neutrons would be more effective in the treatment of human cancer. In 1948 Stone concluded that neutron therapy as administered by him should be stopped because of the severe late skin damage experienced by many patients treated during the period 1938-1943. These initial results discouraged further use of neutrons in radiotherapy. Much later, in a review of Stone's work by Sheline *[Sh71]*, it was concluded that many of his patients were given an overdose because the dependence of the RBE for neutrons on the quantity of neutron radiation given at a time was not known then.

Fast neutrons are used in radiotherapy at various centres around the world. At the Third Neutron Therapy Meeting at The Hague, Netherlands in September 1978, the normal tissue and tumour responses of approximately 3000 patients treated around the world with neutrons were presented. Duarte and Tubiana [Ra80] reviewed the data presented and concluded that the therapeutic benefits of neutrons appear encouraging for the upper respiratory and digestive tracts in the primary tumours as for cervical adenopathy and for advanced carcinoma of the cervix and soft-tissue sarcoma. In order to improve the cure rates in neutron radiotherapy while minimising the damage to normal tissue, requires controlled randomized studies. Such studies are in progress at various centres around

the world.

1.2 NATIONAL ACCELERATOR CENTRE NEUTRON RADIOTHERAPY UNIT

The National Accelerator Centre (NAC) in Faure, South Africa, is a centre where a research programme in neutron radiotherapy is in progress. It is a cyclotron facility capable of producing proton beams of energy up to 200 MeV. This facility is used for basic nuclear research, radionuclide production and radiotherapy with neutron and proton beams. The neutron radiotherapy system has been described in detail in the NAC Annual Reports [Nac87, Jo92].

Briefly, the system consists of an isocentric gantry capable of $\pm 185^{\circ}$ rotation. It includes a collimator with a continuously variable aperture providing fields from 5x5 cm^2 to 30x30 cm^2 at a source-to-axis distance (SAD) of 150 cm (see figure 1.1 and figure 1.2). The beam line components in the gantry include 70° and 160° dipole bending magnets, a quadrupole triplet between the bending magnets, a steering magnet and a beam wobbler system. Beam tuning is facilitated by the beam scanner fitted between the first two quadrupole magnets. Neutrons are produced by the reaction of 66 MeV protons on a 19.6 mm thick copper-backed ^{9}Be target, ($p + {}^{9}Be \longrightarrow n + {}^{9}B$ - 1.85 MeV plus several break-up reactions) in which the proton beam dissipates 40 MeV in the ^{9}Be target and the remaining energy is deposited on the copper backing and cooling water.

The neutron beam is moderated by 0.8 cm thick iron flattening filters (see below). One flattening filter

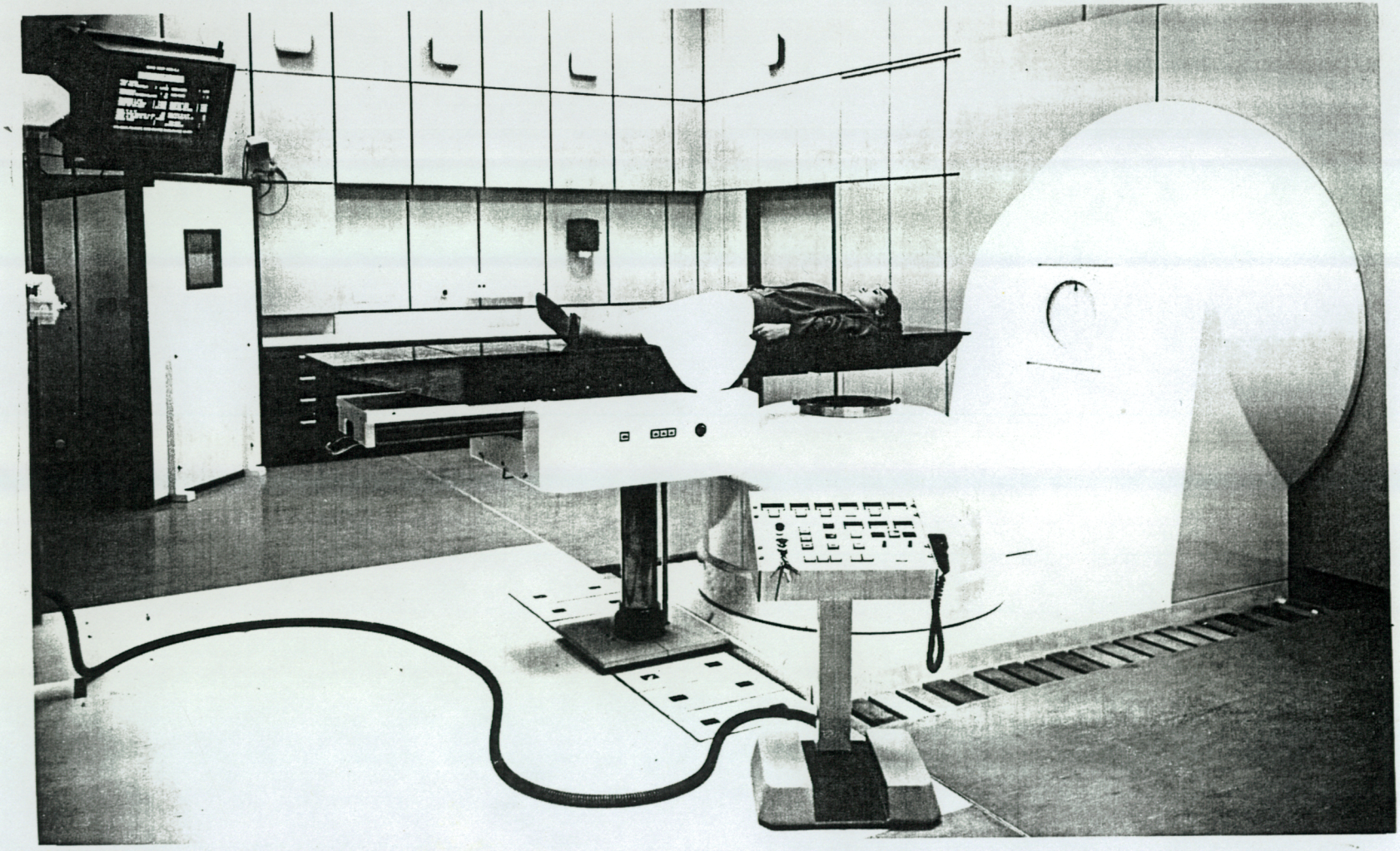

Figure 1.1 The neutron therapy system with the gantry positioned at 180°. The moving floor has been retracted [Na87].

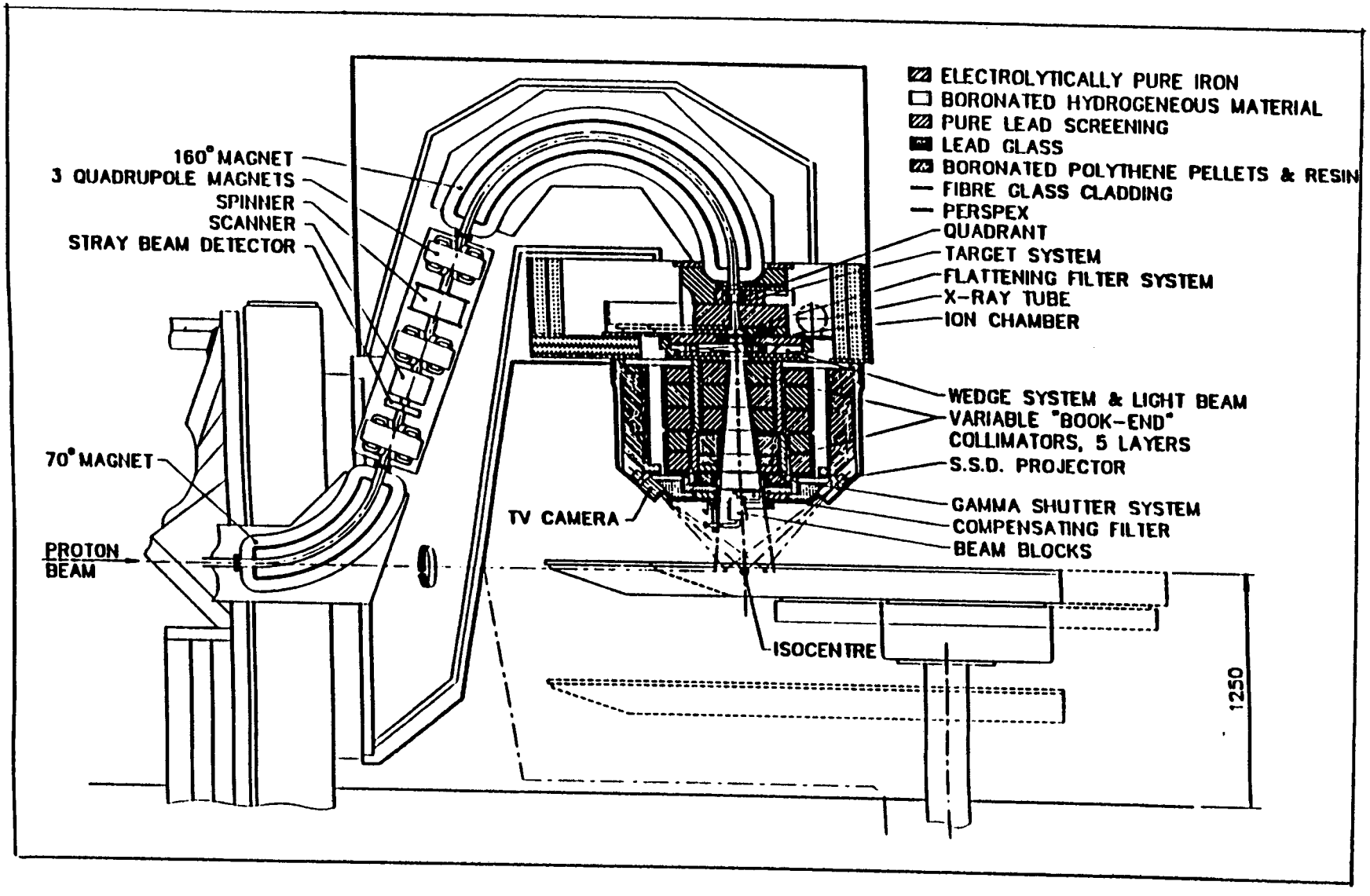

Figure 1.2 Schematic diagram of the NAC neutron therapy system [Na87].

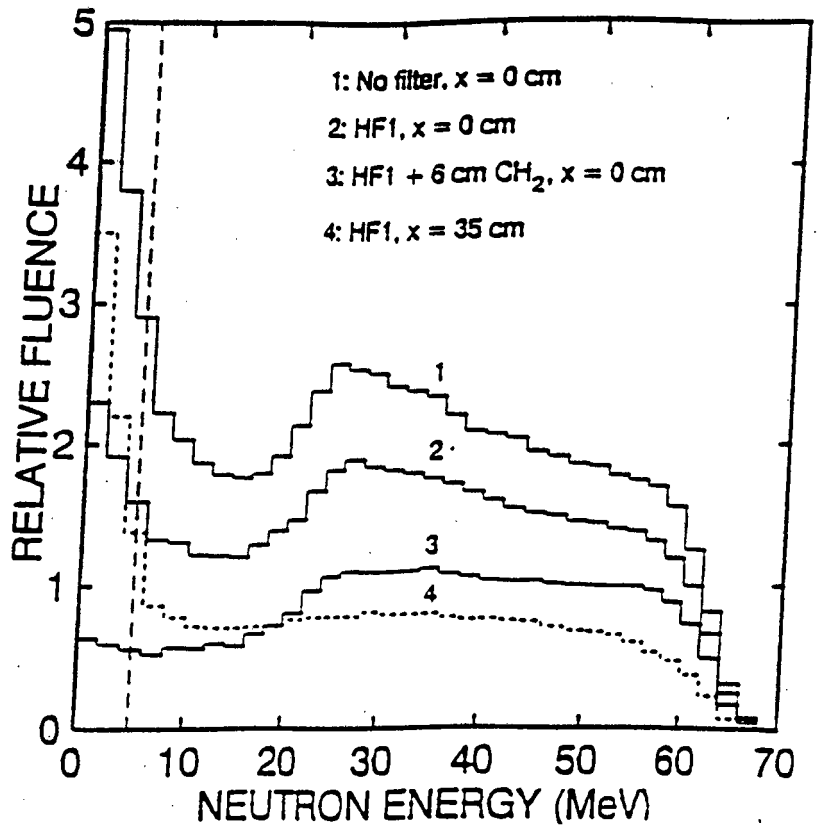

Figure 1.3 Neutron fluence spectrum in a 10x10 cm^2 field showing the effect of different filter combinations on the spectrum, where x is the off-axis distance [Jo92].

(F1) is always in the beam and is used for fields with sides ≤ 16 cm in length while for fields with longer sides, an additional filter (F2) is placed in the beam and a 2.5 cm thick polyethylene $[(CH_2)_n]$ hardening filter (H). The purpose of the flattening filters is to maintain an approximately uniform neutron dose distribution on the field area. The hardening filter is used to reduce the proportion of low energy (≤ 16 MeV) neutrons in the beam. Figure 1.3 shows the effect which different filter combinations have on the dose distribution of the neutrons. It can be seen in the figure that the distribution of the neutrons is almost uniform over the energy range 20 to 60 MeV, while there is a drop in the neutron dose distribution in the region immediately below 20 MeV and a rise in the region below 10 MeV. Three tungsten wedge filters (W_1, W_2, W_3) can be inserted in the beam to tilt the beam

profiles at a depth of 10 cm in water by 25^{o}, 35^{o} and 45^{o}, respectively. This is important for the treatment of tumours of the head and neck region, which may extend from the surface to a depth of several centimeters, to ensure a uniform dose distribution in the tumour sites of interest. The "book-end" collimator consists of five layers of four interlocking blocks of iron and borated polyethylene, geared to provide a tapered aperture and is rotable through 360^{o}. The patient treatment couch is capable of horizontal, longitudinal and vertical movement as well as rotation about a vertical axis through the isocentre and rotation about the support pedestal.

The planning of neutron radiotherapy treatments at such a centre requires accurate knowledge of the physical behavior of the neutron beam as it progresses through the treatment region. This information is used to calculate the energy deposited in tumour sites under treatment and to understand the associated biological effects produced by the neutrons [Be89]. Information is gained in terms of the neutron energy spectrum of the beam in the treatment region

1.3 INTERACTION OF THE NEUTRON BEAM WITH TISSUE

The penetration power of the neutron radiotherapy beam in human tissue depends on the energy spectrum of the neutron beam. The neutron spectrum incident on a patient will depend on the nature of the neutron-producing reaction as well as on the nature of the neutron beam collimation, field size and, the filtration located in the path of the incident beam.

As the neutron beam progresses through the body tissue,

the neutrons interact with the nuclei in their path and transfer their energy by elastic and inelastic processes. The energy distribution of the neutron beam changes as the beam traverses the tissue because the scattering and reaction cross-section of nuclei with neutrons are energy dependent. The interactions between the neutron beam and the nuclei are: (1) elastic scattering on hydrogen nuclei, which produce recoil hydrogen nuclei in the tissue; (2) recoils of heavier nuclei present in tissue such as carbon, nitrogen and oxygen, and (3) nuclear reactions such as $^{12}C(n,p)^{12}B$, $^{12}C(n,d)^{11}B$ or $^{12}C(n,\alpha)^{9}Be$. The various charged particles to which the neutron interactions give rise deposit their energy in many different ways, i.e. they have different LET which has important biological consequences. At low energies, the process which contributes most of the absorbed dose is elastic scattering of neutrons by hydrogen. However, with increasing neutron energy, the probability of interaction with other nuclei, mainly C, N and O increases. At energies greater than about 50 MeV these contributions exceed those of the interactions with H.

For treatment planning and radiobiological studies of neutrons it is important to know how the neutron spectrum varies at different positions within the treatment region under irradiation. To determine the neutron spectra as a function of position we use a tissue-like phantom (tissue-equivalent phantom) which consists of a water-based solution containing materials so as to simulate the chemical composition of body tissue. This also has the advantage that neutron detectors can be immersed in the liquid and moved to different positions relative to the entry point and axis of the incident beam to measure neutron spectra as a function of position. In addition to this, the neutron detectors should be able to discriminate

against gamma rays that arise from neutron interactions with the shielding, collimating materials and body tissue.

1.4 PREVIOUS MEASUREMENTS OF NEUTRON RADIOTHERAPY SPECTRA

At energies below 20 MeV there are a range of spectrometric methods which have been used to measure neutron radiotherapy spectra in air and in tissue-equivalent phantom, including recoil telescopes [Pa72], gas proportional counters and scintillation detectors [Sc81], as well as activation foils [Bo82, Pa82]. Neutron therapy beam characteristics and the charged particles produced by them could thus be investigated experimentally as well as computationally when used in therapy trials. Since the information on the neutron energy spectra data of these beams are well documented at energies below 20 MeV.

However, at higher neutron energies, the charged particle production cross-sections and reaction mechanisms are less well known. In addition, the experimental methods used to measure spectra are more demanding [Cr88]. Measurements of neutron radiotherapy spectra in air and in tissue-equivalent phantom for neutron energies between 10 and 60 MeV have been made by Crout et al. [Cr91] using NE213 recoil spectrometry and, by Moyers et al. [Mo90] using a method that involves the iterative fitting of water-attenuation measurements to derive the neutron spectrum. Measurements in air have

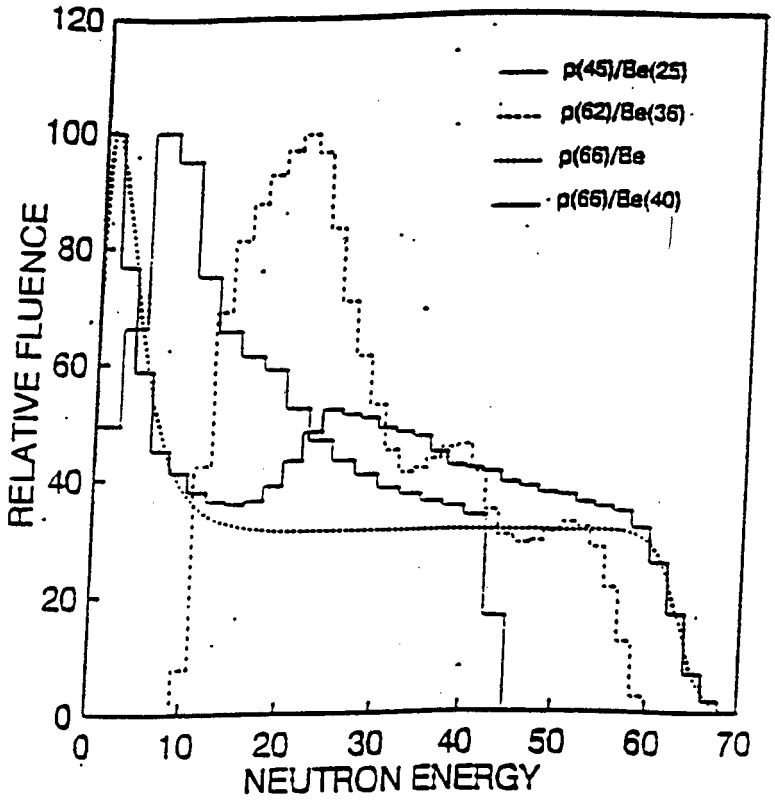

Figure 1.4 Comparison of different neutron fluence spectra normalised to 100 at maximum fluence. Note the differences in the spectrum measured at NAC (solid lines) and the one measure at Clatterbridge Hospital (dotted line) [Jo92].

also been made by Jones et al. [Jo92] using a pulsed-beam and time of flight at the NAC radiotherapy unit. The results from the investigations made by Jones et al. at NAC and of Crout et al. made at a nearly identical neutron therapy unit at Clatterbridge Hospital, UK, differ significantly, as shown in figure 1.4. The cause of the difference in the spectra is not understood [Jo92]. However, the investigations show that the measured neutron energy spectra are affected by the filters and the field size of the incident neutron beam system (see figures 1.3 and 1.5). Also, the work of Crout clearly shows that the neutron energy spectra measured within a tissue-equivalent phantom change as a function of position (see figure 1.6).

These results indicate that if valid intercomparisons between different neutron radiotherapy centres are to

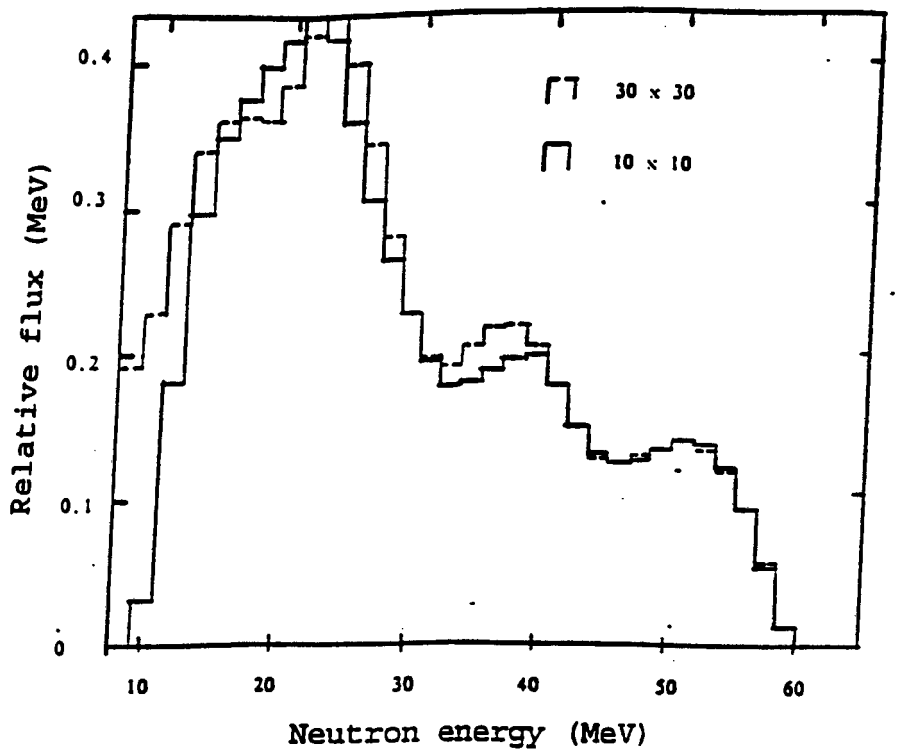

Figure 1.5 Neutron spectra measured in air for the 10x10 cm^2 and 29x29 cm^2 field sizes on the Clatterbridge Hospital cyclotron [Cr91].

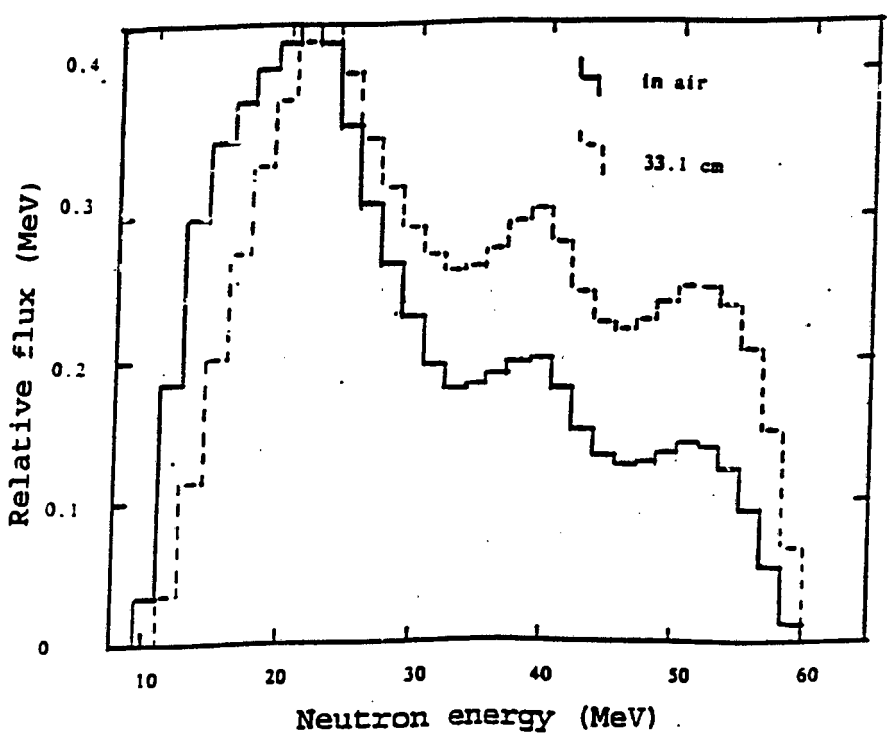

Figure 1.6 Neutron spectrum measurements for a 10x10 cm^2 field size in air and in a phantom on the Clatterbridge Hospital cyclotron [Cr91].

be made when clinical data are exchanged between them, determination of the neutron spectra of the neutron beams of these centres are important. This is particularly so in the energy range 10 to 60 MeV where few experiments have been performed to measure the neutron energy spectra of these radiotherapy beams in tissue-equivalent phantoms.

1.5 OBJECTIVES OF THE PROJECT

This research is a preliminary investigation to test a new technique for determining neutron radiotherapy spectra within a phantom. The new technique was tested by measuring the neutron radiotherapy spectra at different positions within a tissue-equivalent phantom at energies between 0 and 63 MeV, simulating a patient under treatment at the NAC radiotherapy unit. The effects of field size and filtration in the incident neutron beam on the spectra in the tissue were also investigated.

The work of Crout et al. [Cr91] and others have demonstrated the feasibility of using organic liquid scintillators for the measurement of neutron energy spectra within a phantom. They used an NE213 liquid scintillator and Pulse Shape Discrimination (PSD) to measure the proton pulse height spectra resulting from the interaction of neutrons in the NE213 scintillator. A computer code RADAK was used to determine the neutron spectra from the measured proton pulse height spectra.

In the new technique an NE230 deuterated liquid scintillator was used as a deuteron recoil spectrometer. Pulse height spectra were measured for the deuterons resulting from the interaction of neutrons in the

scintillator. The neutron spectra were determined from the pulse height spectra by using a computer spectrum unfolding package HEPRO [Ma94].

The neutron energy spectra referred to in the above section, determined by Jones et al., were derived from TOF spectra, rebinned from equal time bin to equal energy bin and corrected for the variation of neutron detector efficiency with neutron energy. In this research all measured neutron energy spectra will be presented in TOFB, i.e as if measured by TOF. They could be rebinned from equal time bin to equal energy bin. However this was not done because the objectives of the research was to test a new technique for determining the changes in the energy spectra for different beam defining conditions with position within a phantom. These changes in the energy spectra can be seen quite adequately in the time of flight representations (TOFB) of the spectra. Hereafter, therefore, the term neutron spectrum, without further qualification will be used to denote an energy spectrum presented in time of flight binned (TOFB) form, regardless of the method (TOF or other) used to determine the spectrum.

CHAPTER 2

MEASUREMENT OF NEUTRON ENERGY SPECTRA

Neutron spectrometers can generally be classified into three categories, neutron time of flight (TOF), recoil spectrometers and those based on nuclear reactions. The TOF method, which is basically a measurement of the velocity of the neutrons, is the most popular and versatile of these categories today. However, it requires that neutrons be detected with good timing, in order that their time of travel over a known distance can be measured. Recoil spectrometers are based on measuring the energy of recoil (charged) nuclei associated with neutron elastic scattering, the most common being ^{1}H and ^{2}H. The energy of the recoiling nucleus is related to that of the incident neutron through the conservation of momentum and energy [Dy81]. There are not many nuclear reactions suitable for use as neutron spectrometers. However, one such reaction is the $^{3}He(n,p)^{3}H$ reaction in which the measured total energy, E, of the charged products (p and ^{3}H) is directly related to the neutron energy, E_n, by

$$E = E_n + Q \qquad where\ Q = 0.765\ MeV \qquad (2.1)$$

Neutron spectrometers based on this reaction are generally ion chambers filled with ^{3}He or proportional counters. Their use is generally confined to neutron energies $E_n \leq 3$ MeV due to the decline in reaction cross-section and the increase in the "wall effect" (escape of reaction products from the counter with increasing neutron energy). For our work, involving

neutron energy up to ~ 63 MeV, we therefore confine our interest to the TOF and recoil based spectrometers.

2.1 THE TIME OF FLIGHT SPECTROMETER

In the neutron time of flight method, the velocity, v, of neutrons is determined from the time, t, taken to travel a flight path of length, d. In such time of flight experiments, the neutron source is usually a pulsed ion beam [Fi79]. For low neutron energies, the kinetic energy may be approximated by the non-relativistic equation

$$E_n = \left[\frac{72.3d}{t_n} \right]^2 \qquad (2.2)$$

where: E_n = *neutron energy (in MeV);*
t_n = *time of flight (in ns); and*
d = *flight path (in m)*

However, at high neutron energies (≥ 50 MeV) the relativistic equation should be used to calculate the kinetic energy of the neutrons. For E_n = 63 MeV, the maximum energy used in this work, the error introduced by using equation (2.2) is only about 1.05%, which is considered tolerable for our purpose. The uncertainty, ΔE_n, in the neutron energy is given by the equation

$$\Delta E_n = 2E_n \sqrt{\left[\frac{\Delta t_n}{t_n} \right]^2 + \left[\frac{\Delta d}{d} \right]^2} \qquad (2.3)$$

where: Δt_n = *the time uncetainty from all sources; and*
Δd = *the uncertainty in the flight path*

2.2 RECOIL SPECTROMETERS

Recoil spectrometers measure the energy of recoiling nuclei in elastic scattering processes. Using the conservation of momentum and energy, the recoil nucleus kinetic energy, as a function of recoil angle, ϕ, in the laboratory frame, is

$$E_r = \left[\frac{2M}{M + m}\right]^2 E_n . \cos \phi \qquad (2.4)$$

where: E_r = *kinetic energy of the recoiling nucleus;*
M = *mass of the recoiling nucleus;*
E_n = *incident energy of the neutron; and*
m = *mass of the neutron*

The recoil nucleus may have any energy between 0 (ϕ = 90^0) and $\left[\frac{2M}{M + m}\right] . E_n$ (ϕ = 0^o). As a result, the relationship between the neutron energy spectrum and the pulse height spectrum of the recoiling nucleus is non-linear. The energies of the recoil nuclei are measured in different ways and the results are then used to determine the neutron spectra. For example, photographic emulsions, proportional counters, recoil telescopes and solid and liquid scintillators, are among the methods that may be used [Kn89].

Most of these types of neutron spectrometers are based on hydrogen recoils or deuteron recoils from elastic scattering of neutrons. For neutron spectroscopy by the recoil or time of flight methods, organic liquid scintillators have proven to be particularly suitable detectors because they can be large and therefore efficient. They also have good timing resolution and pulse shape discrimination properties. They are the main detectors used for neutron spectroscopy from ~ 10 keV to 200 MeV today.

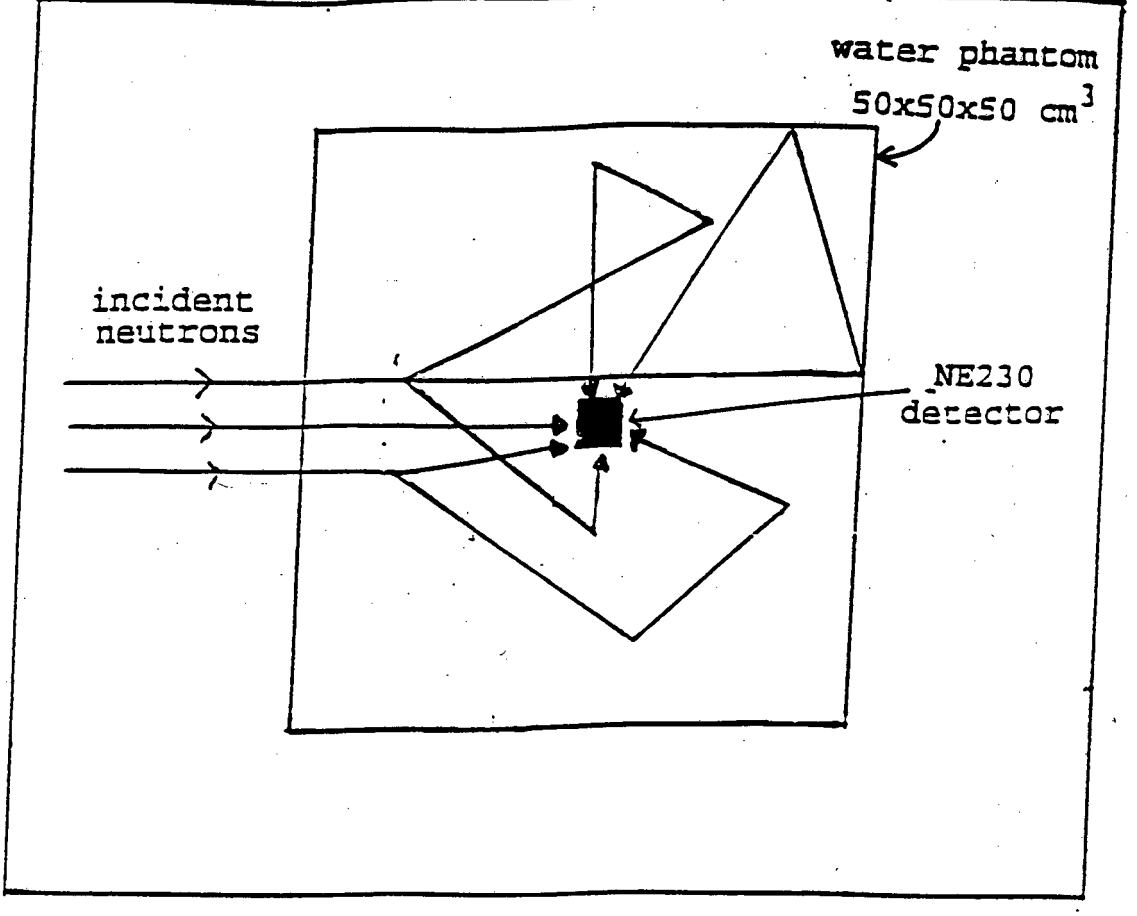

Figure 2.1 Possible flight paths which a neutron may follow on entering a phantom before reaching the detector, due to scattering.

2.3 DETECTOR REQUIREMENTS FOR NEUTRON SPECTROMETERY IN A PHANTOM

The detector used in this work had to be small and had to have scattering properties similar to the phantom to reduce neutron flux perturbation in the phantom. Also, the detector had to have pulse shape properties to discriminate against the gamma rays which always accompany the neutrons (section 1.3). The detector also had to be capable of accurately measuring the energy of the neutrons regardless of the direction from which they could arrive at the detector when placed in the phantom.

Neutrons entering the phantom may arrive at the detector from any direction (see figure 2.1) due to

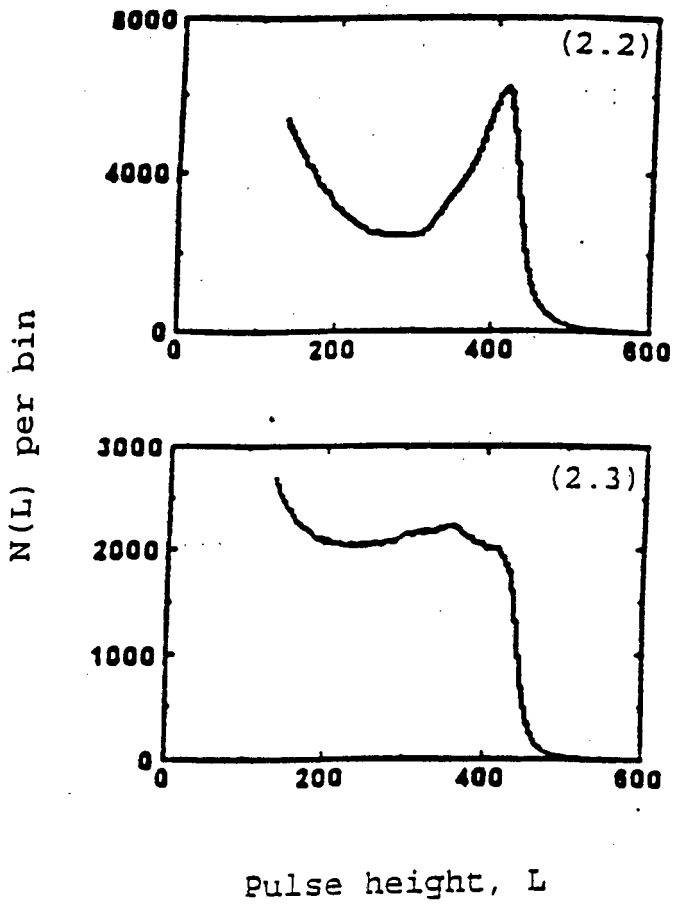

Figures 2.2 and 2.3 Lineshapes, N(L), versus pulse height, L, for 7.5 MeV neutrons measured for the liquid scintillators (2.2) NE230 and (2.3) NE213 [Bu97].

scattering. Therefore, the incident energy with which a neutron enters the phantom may change before it reaches the detector. As a result of this the recoil method was preferred over the TOF method for measuring the neutron spectra in the phantom since the flight path for the TOF method would not be well defined (see figure 2.1).

2.4 CHOICE OF SPECTROMETER

The NE230 deuterated liquid scintillator was used as a recoil spectrometer in the present work for the following reasons. The NE230 scintillator has similar PSD properties to the NE213 scintillator [Cz70, SM68 and Bo72]. Figures 2.2 and 2.3 show the lineshapes for 7.5 MeV neutrons measured by NE230 and NE213. The lineshapes for NE230 reflect the forward-back peaking

of the angular distribution for n-d elastic scattering while that for NE213 is approximately flat due to the isotropic angular distribution of n-p elastic scattering in the CM frame [Bu97]. The features, i.e. the forward recoil peak and low valley, in the lineshape of the NE230 spectrometer should make the process of determining the neutron energy spectrum from the deuteron pulse height spectrum easier [Br79]. Also, the probability of recoil deuteron escape through the cell walls of a NE230 scintillator will be less than the recoil proton escape through the walls of a NE213 cell of the same size because recoil deuterons have a shorter range than recoil protons in a scintillator (see section 2.3). This means that the probability for deuterons to escape without depositing all their energy in the scintillator medium is lower than in the case of protons.

When the detector is immersed in a water phantom it is necessary to block out protons produced by neutron elastic scattering on the hydrogen in the water itself. When using an NE230 deuterated liquid scintillator and selecting deuteron events by PSD, these protons are automatically excluded for pulse height analysis. When using an NE213 scintillator these 'external' protons cannot be distinguished from the recoil protons selected for pulse height analysis. By using an NE230 scintillator the uncertainty in the determined neutron spectrum will therefore be reduced.

2.5 GENERAL EXPERIMENTAL PRINCIPLES

The main interaction between the neutron radiotherapy beam and the NE230 scintillator is by elastic scatter -ing with deuteron nuclei because of the large

deuterated content of the scintillator. Depending on incident neutron energy, other reactions such as inelastic scattering with carbon or deuteron nuclei and nuclear reactions with carbon (section 1.3) can occur. As the recoil deuteron nuclei and other charged particles moves in the scintillator, they deposit their energy in the scintillator which gives rise to scintillations. The scintillations time-decay may be described as the sum of a fast exponentail component (with lifetime of a few nanoseconds) and a slow exponentail component (with a lifetime of several hundred nanoseconds). The relative intensities of these fast and slow scintillation components are dependent on the type and energy of the particle producing them. This offers a method to discriminate between the different particles Figure 2.4 is an example of a perspective view of counts versus pulse height,L, and pulse shape, S, which shows the use of PSD to identify and separate different charged particles. The scintillation processes and different methods to discriminate between different particles, have been described by Birks [Bi64) and Brooks [Br79].

Say L(E) is a pulse height spectrum measured by selecting the deuteron recoil events resulting from the interaction of neutrons of a particular energy in the scintillator medium (see figure 2.2 for, example). The upper edge limit of this spectrum is a well known function of neutron energy because it peaks sharply just below maximum recoil deuteron energy. This neutron energy can be can be calculated using

$$E = \frac{8}{9} E_n \qquad (2.5)$$

where : E_n *= the neutron energy (MeV);*
E *= the maximum recoil deuteron energy (MeV)*

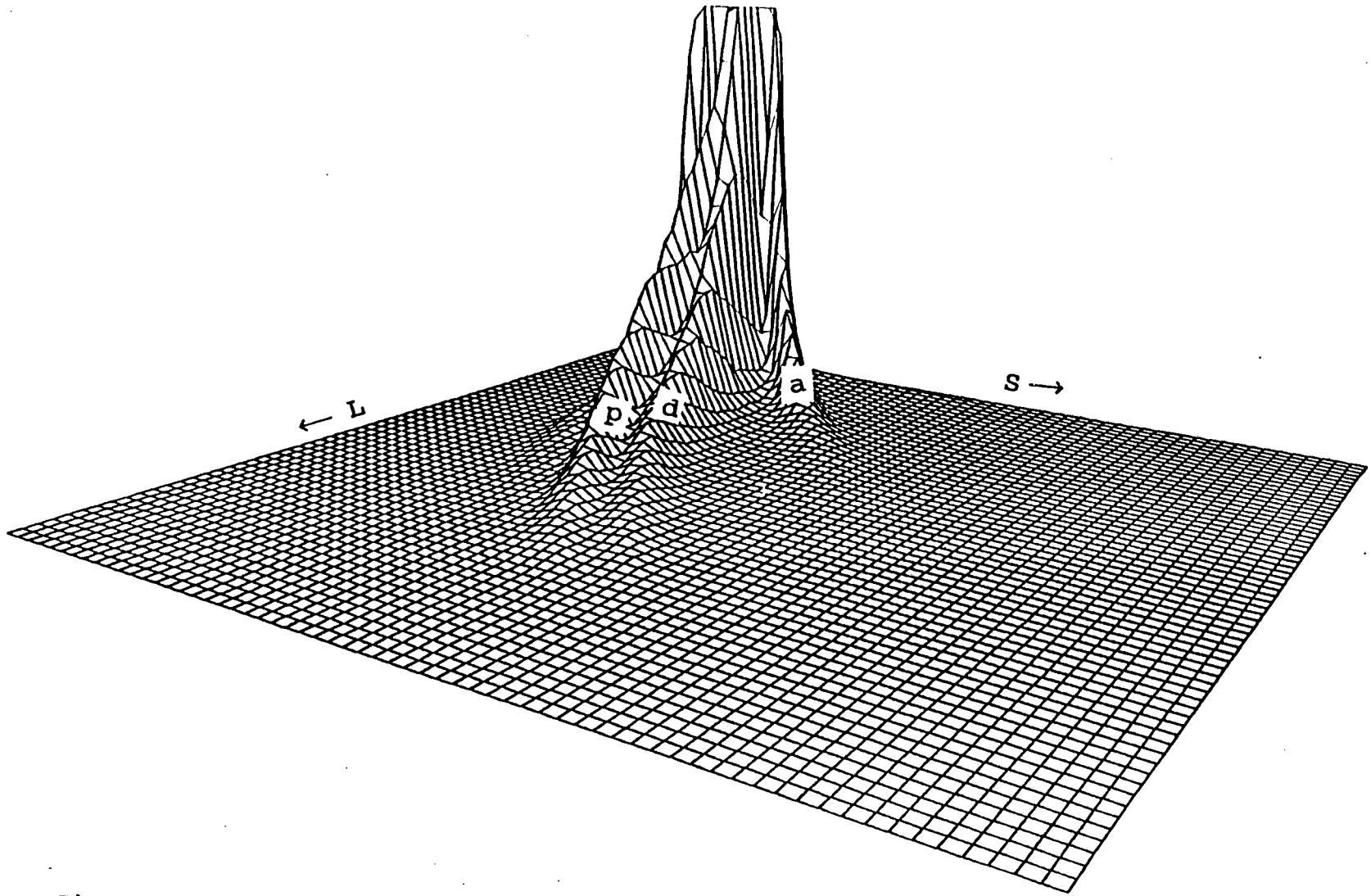

Figure 2.4 Perspective view of counts (vertical) as a function of pulse height, L, and pulse shape, S, for the events of the open beam measured by the NE230 spectrometer when exposed to neutrons of energy range 0 to 63 MeV. The ridges corresponds to protons, p, deuterons, d, and alphas, a.

and; the factor $\frac{8}{9}$ *is calculated from equation (2.4) with* $\phi = 0^{o}$ *and* $m = 2$.

The relationship between the measured pulse height spectrum, L(E), and the incident neutron spectrum, $\Phi(E_n)$, is given by the matrix equation

$$L(E) = R(E,E_n)\Phi(E_n) \qquad (2.6)$$

where $R(E,E_n)$*, the response matrix, is the probability per unit energy interval that a neutron of energy* E_n *interacting in the scintillator deposits energy E.*

From equation 2.6 it can be seen that the response matrix of the spectrometer needs to be known for the unfolding process. Figure 2.2 shows that the response of the spectrometer to neutrons of a discrete neutron energy includes a wide range of pulse heights (deuteron energies. Therefore, to unfold the neutron spectrum from the pulse height spectrum will require a matrix unfolding code.

We decided to use the NE230 spectrometer to measure the pulse height spectra within the phantom for different beam defining conditions. The neutron energy spectra were obtained by unfolding the pulse height spectra, using the HEPRO progam system developed by Matzke et al at PTB, Braunschweig, Germany.

CHAPTER 3

THE EXPERIMENT

3.1 EXPERIMENTAL DETAILS

Figure 3.1.1 is a schematic diagram showing the experimental setup for the measurements. The water phantom (60x60x60 cm^3) was mounted in the treatment room at a flight path of 5.33 m (front face of tank) from the ^9Be target. The neutron radiotherapy beam was produced by the $^9Be(p,n)^9B$ reaction as described in section 1.2 with the gantry rotation angle set at 270^o to provide a horizontal beam.

The NE230 detector consisted of a single cylindrical cell of NE230 deuterated liquid organic scintillator, (diameter 2.5 cm and length 2.5 cm). Table I lists the physical properties of the scintillator.

Table I Physical properties of the NE230 scintillator (NE)

Mass % of D	14.2
Mass % of C	85.7
Mass % of H	0.1
No of D / No of C atoms	0.984

The NE230 detector was mounted on a 10 cm long tapered (see figure 3.1.2) perspex light pipe, in order to reduce perturbations caused in the neutron spectrum by

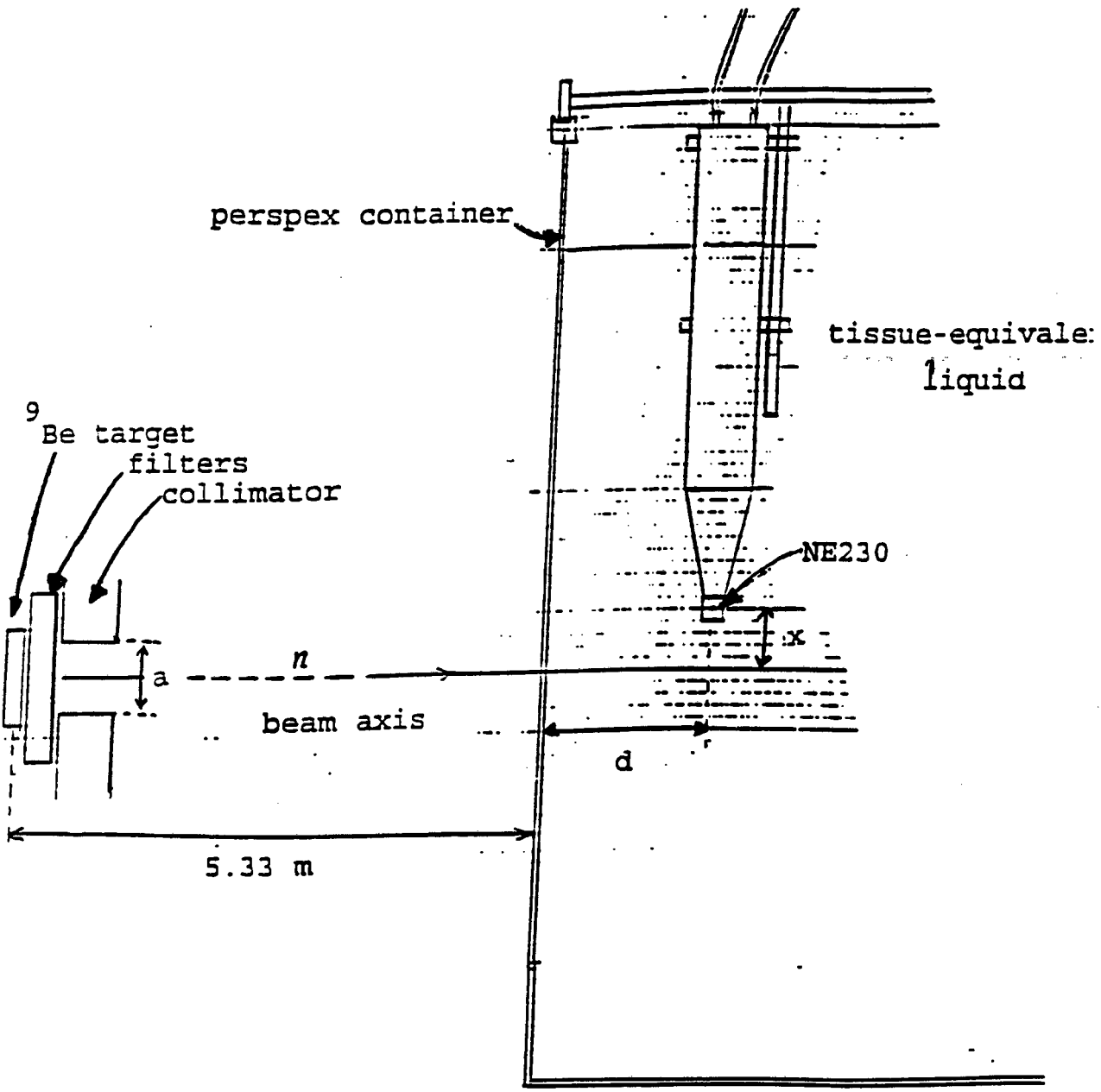

Figure 3.1.1 Schematic diagram of the experimental arrangment. The experimental variables were: the composition of the filter (see section 1.2); a is the side of the square collimator aperture; the depth d; and lateral deviation x from the beam axis.

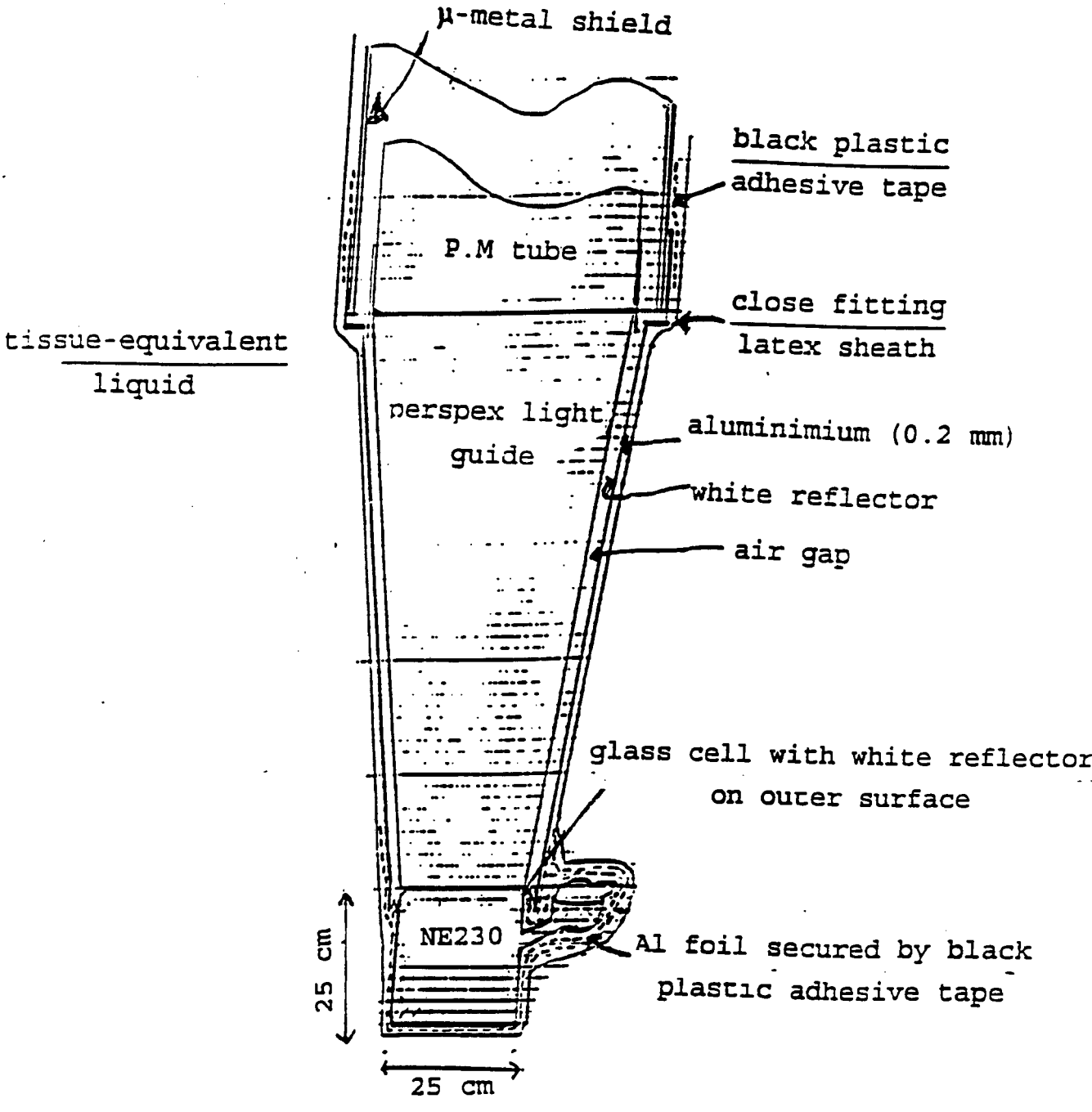

Figure 3.1.2 Diagram of the scintillation detector assembled for immersion in tissue-equivalent liquid.

the presence of the detector probe. Perspex, like tissue-equivalent liquid is composed from the light elements C, H and O. The displacement of the tissue-equivalent liquid by perspex, in the vicinity of the NE230 scintillator is therefore expected to introduce less distortion in the measured neutron spectrum than would be the case if the light pipe were omitted, leading to distortions introduced by the photomultiplier tube components being measured. The window of the cell was optically coupled to a RCA 8575 photomultiplier tube by the perspex light guide. For all measurements, the NE230 cell was oriented with its diameter parallel to the direction of the neutron radiotherapy beam.

3.2 DATA ACQUISITION SYSTEM

Figure 3.2 shows a schematic diagram of the main electronic components of the data acquisition system. A more detailed circuit diagram is shown in figure 3.3. Three parameters were recorded for each event: L, the scintillation pulse height (which is a measure of the sum of the fast and slow components of the scintillation light); F, the integral over the fast component of the scintillation pulse; and T_n, the neutron time of flight.

The output from the anode of the photomultiplier tube was fed into the LINK model 5010 pulse shape discrimination unit which generated the L and F pulses. A modification was made to the LINK in order to provide the F pulse *[Sm86]*. The F pulse is generated by integrating over a period of 3 ns which is approximately the lifetime of the fast component of the scintillation decay. The L pulse was generated in the LINK by integ-

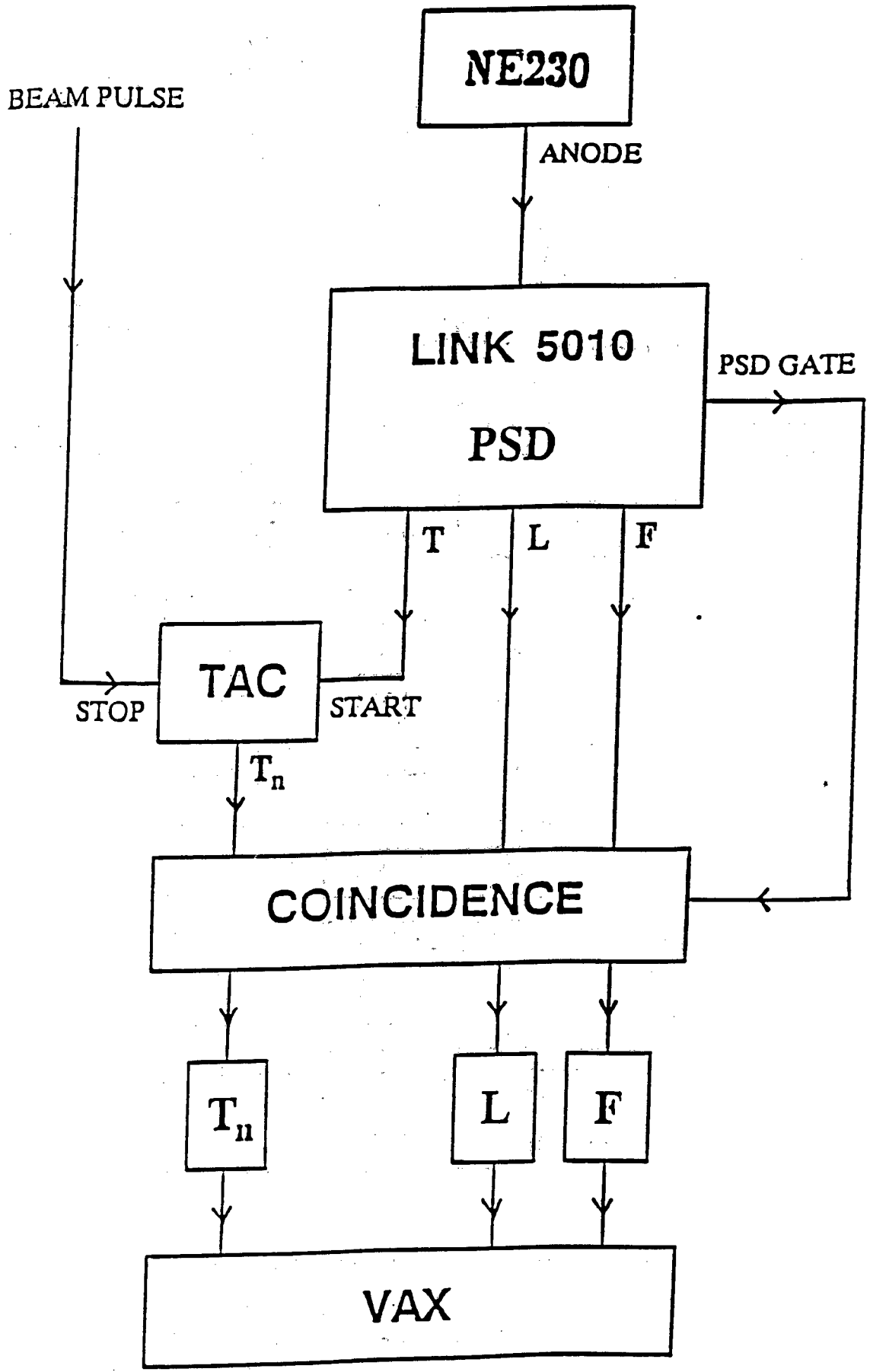

Figure 3.2 A schematic diagram of the main electronic components used for pulse processing.

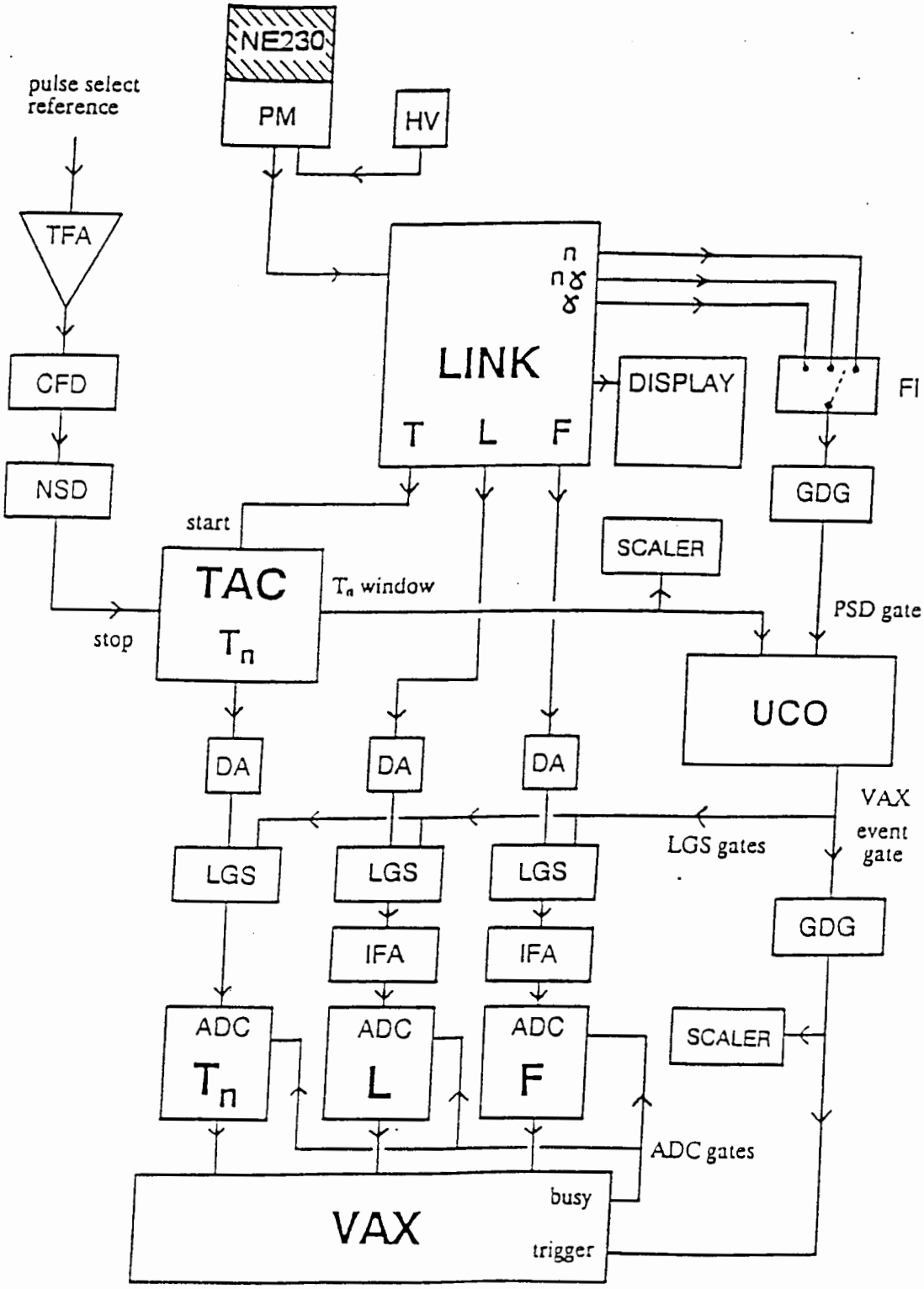

Figure 3.3 A complete circuit diagram of the electronic configuration. Standard NIM modules (Canberra or Ortec) are indicated as follows: ADC, Analog To Digital Converter; CFD, Constant Fraction Discriminator; DA, Delay Amplifer; IFA, Interface Amplifer; GDG, Gate Delay Generator; LGS, Linear Gate and Strecher; NSD, Nanosecond Delay and TFA, Timing Filter Amplifer.

rating the scintillation pulse over a period of 500 ns.

The Link also includes a constant fraction timing discriminator, which provided a timing pulse, T, which was used to start the time to amplitude converter (TAC) for measuring the neutron time of flight, T_n. The measurement of T was made relative to a fixed point in the cyclotron RF cycle. The time reference signal for this measurement was derived from the RF cycle of the injector cyclotron which operated at a frequency of 16.373 MHz for 66 MeV. Pulse selection (1 in 5) was used to give a beam frequency of 3.275 MHZ corresponding to pulse separation of 305 ns. An event was passed by the coincidence unit (UCO) whenever there was both a pulse on the TAC output and the PSD gate from the LINK (see figure 3.2). Three parameters L, F and T_n were recorded event by event in the experiment and were fed through the ADCs into a VAX computer system where they were recorded on magnetic tape using the data acquisition code XSYS. All phases of the data acquisition were monitored on a system of displays to detect any electronic drifts. The analysis of the data was executed off-line using the computer program GNU which is available at the University of Cape Town. All measurements were done overnight in a 12 hour session.

3.3 SELECTING THE DEUTERON EVENTS

The deuterons released from the neutron-induced events in the scintillator medium were identified by PSD. This was achieved by computing a pulse shape parameter, S, from the L and F outputs from the LINK module. The pulse shape parameter, S, indicates the scintillation pulse shape and hence the type of ionising particle causing the scintillation. S was computed using the

relationship:

$$S = L - kF + c \qquad (4.1)$$

where k and c are arbitrary constants.

The events corresponding to different ionising particles each have a unique set of L and S values which depend on the type and the energy of the ionising particle. Figure 2.4 is a perspective plot of counts (vertical) as a function of pulse height (L) and pulse shape (S) for the events measured by the NE230 scintillator for incident neutron energies from threshold energy (4 MeV) to 63 MeV. It can be seen from this figure that the events corresponding to different ionising particles lie on well-defined ridges in the LS-plane. The ridges identified in the spectrum are those associated with protons from the breakup of the deuterons or carbon nuclei, deuterons from the n-d elastic scattering and from the $^{12}C(n,d)^{11}B$ reaction and alphas from the reactions $^{12}C(n,\alpha)^{9}Be$ and $^{12}C(n,n)3\alpha$.

The deuteron events were selected from a density plot of L versus S, such as the one shown in figure 3.4, using a computer program GNU. This was done by specifying a series of points which defines the upper and lower limits of the region on which the events were lying in the LS-plane. The program GNU then fits smooth curves through these points and the events lying between these curves were selected. The projection of these events onto the L-axis gives the corresponding pulse height spectrum, as shown in figure 3.5.

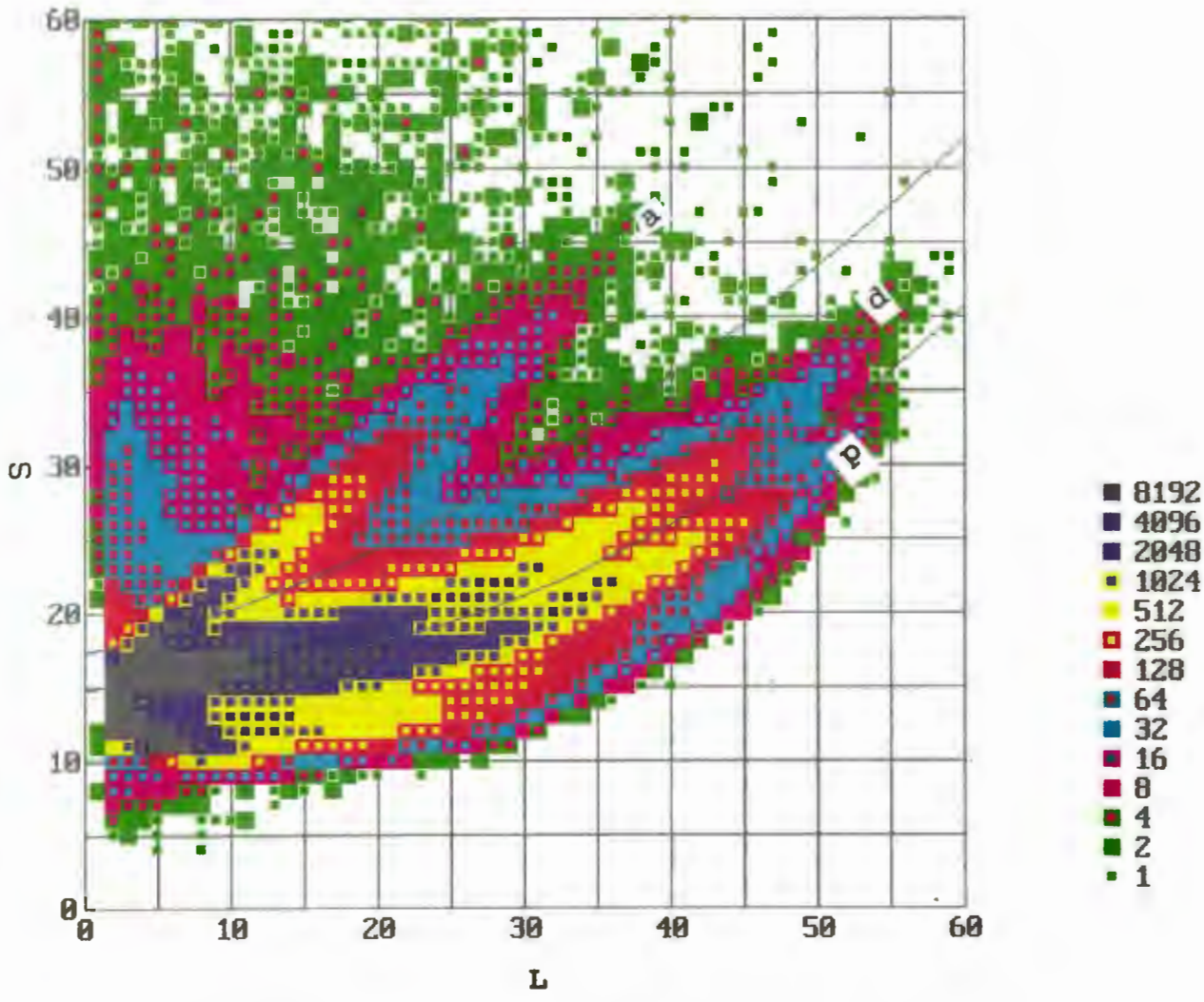

Figure 3.4 Density plot of the events detected by the NE230 spectrometer as a function of pulse height, L, and pulse shape, S, when exposed to neutrons of energy range 0 to 63 MeV. Also shown is the deuteron cut, d, used to separate the deuterons from the protons, p, and alphas, a.

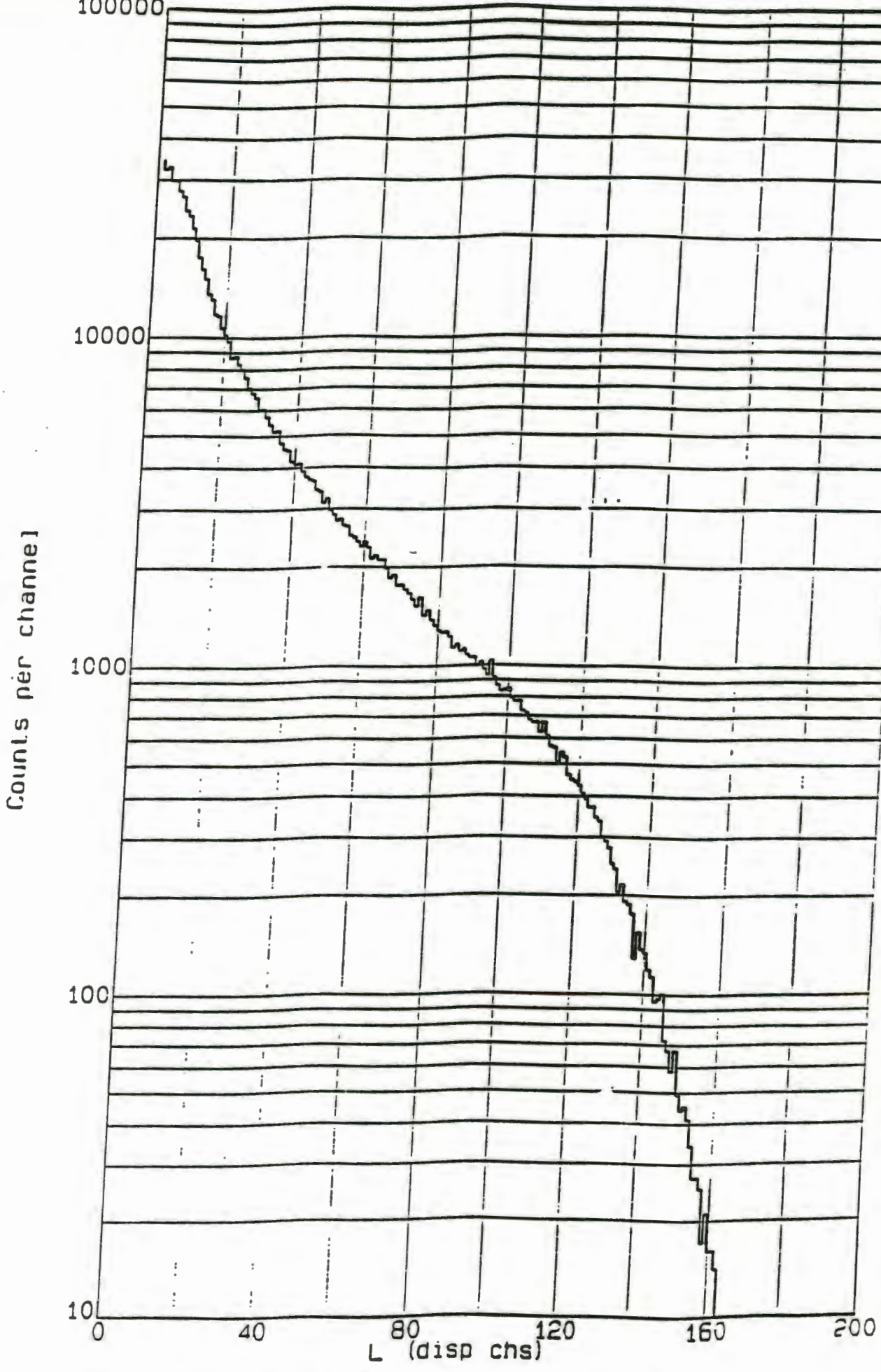

Figure 3.5 Projected pulse height spectrum of the open beam measured with the NE230 spectrometer in air.

3.4 THE TIME OF FLIGHT SPECTRUM MEASUREMENT OF THE NAC NEUTRON THERAPY BEAM

The time of flight (TOF) spectrum of the open neutron therapy beam was measured with the detector (NE230 scintillator) in air, 5.89 m from the ^{9}Be target along the beam axis. Figure 3.6 shows, a perspective plot of counts versus pulse height, L, and time of flight, T_n, for the events identified as deuterons obtained for this measurement. The figure clearly shows on the left, the forward recoiling deuteron ridge, D_f, in the LT_n-plane which can be calibrated in terms of each incident neutron energy in the neutron time of flight range (see section 2.5). Also shown in the figure is the second ridge at higher pulse height, which corresponds to deuterons, D_g, from the ground state transition of the $^{12}C(n,d)^{11}B$ reaction. The projection of all the events on the LT_n-plane onto the T_n-axis, gives the TOF spectrum of the open beam, shown in figure 3.7. The figure shows that the spectrum consists of a broad energy distribution of the neutrons. The upper limit of this distribution, T_u, corresponds to the most energetic neutrons which are released from the ground state transition of the $^{9}Be(p,n)^{9}B$ reaction. The maximum energy of the neutrons emerging from the $^{9}Be(p,n)^{9}B$ reaction was calculated to be 63 MeV [Nc93]. On the right of T_u there is a gamma peak, T_g (channel number 214), which arises from the low energy gamma rays emitted in the proton induced reactions in the Be target. These gamma rays reach the detector at a fixed time, defined by the speed of light and the flight path. The full width at half maximum of the gamma peak provides a measure of the intrinsic timing resolution of the system which is 1.5 ns. The humps observed in the spectrum between channel numbers 80 to 120 are attributed to neutrons with longer flight paths than

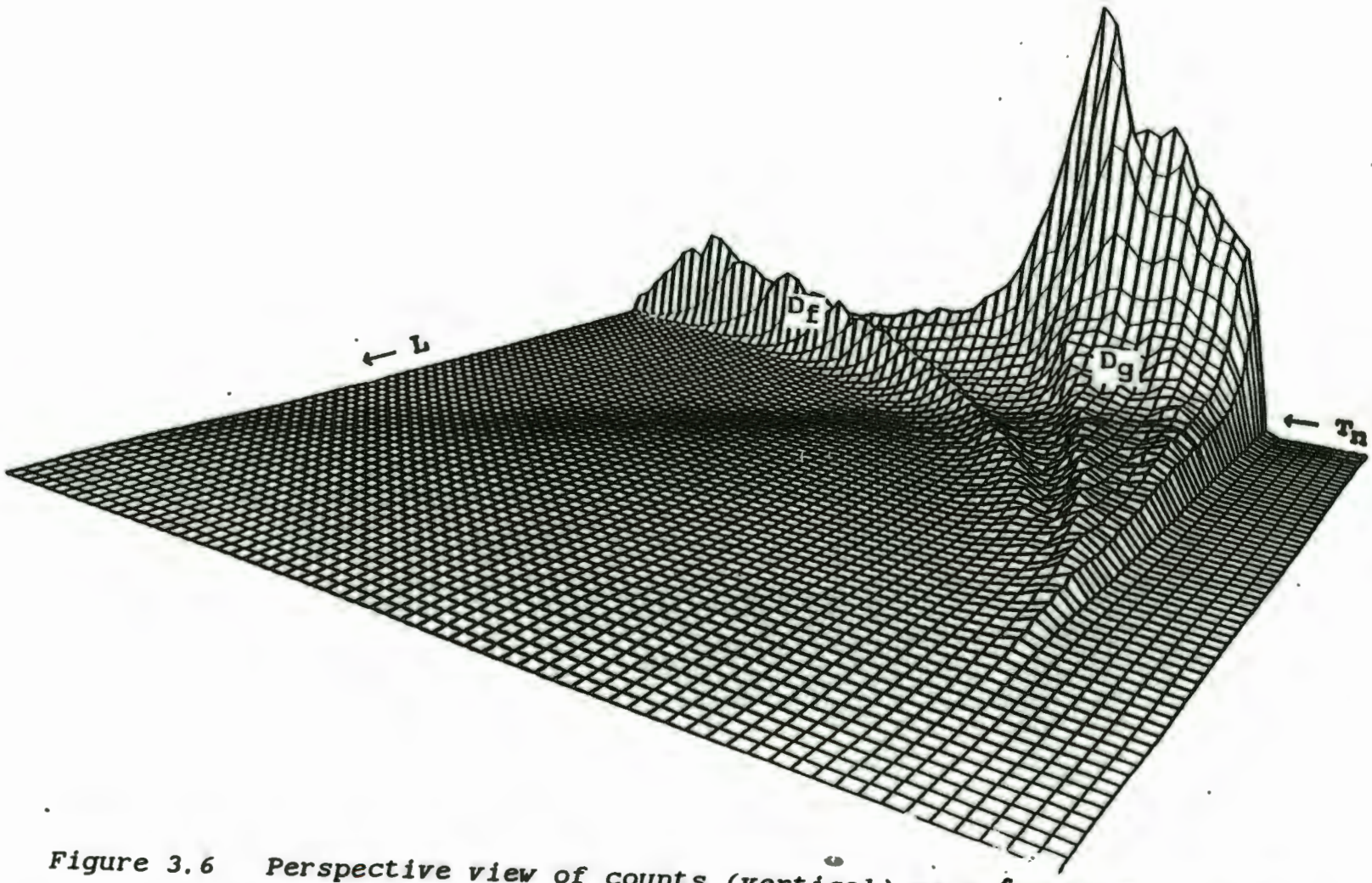

Figure 3.6 Perspective view of counts (vertical) as a function of pulse height, L, and time of flight, T_n, for the deuteron events of the open beam measured by the NE230 spectrometer when exposed to neutrons of energy range 0 to 63 MeV. See text for details.

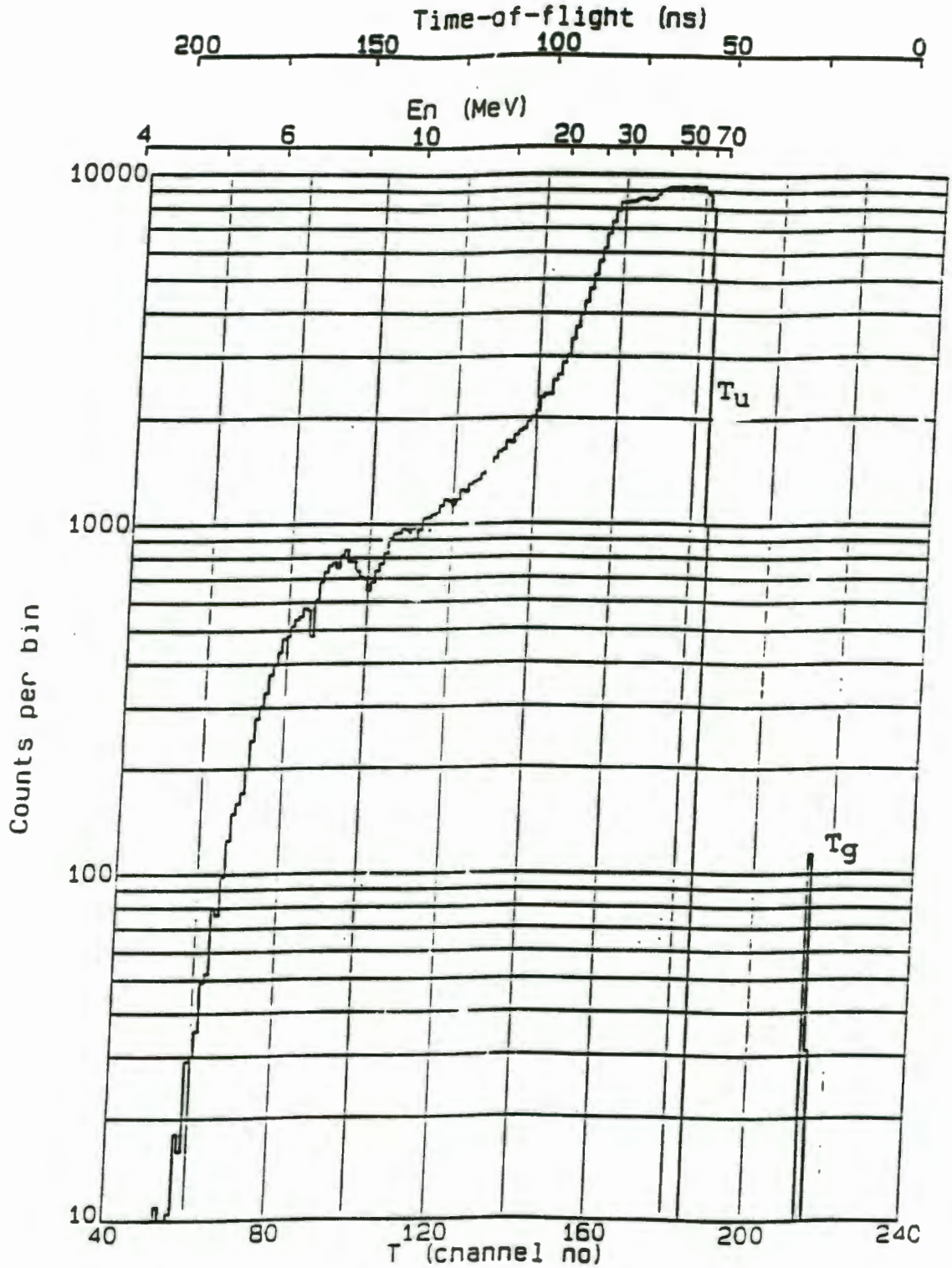

Figure 3.7 Time of flight spectrum measured in the open beam using flight path 5.89 m. Counts are plotted as a function of time bin T. The time calibration is 1.1 ns per bin. Neutron energy and time of flight calibration are shown. The prompt gamma peak, severely suppressed by pulse shape discrimination, can be seen at channel 214 (t = 19.6 ns).

5.89 m, the flight path used. Therefore, they may be due to scattering from the collimator.

3.5 NEUTRON ENERGY CALIBRATION

Time of flight spectra may be calibrated using commercially available time calibrators or coaxial cables which introduce an accurately known delay. Neither of these methods were available at the time of the experiment. Therefore, the following method was used. The flight times for the neutrons and gamma rays associated with the edge, T_u and the peak, T_g (see figure 3.7) were determined to be 53.7 ns and 19.6 ns respectively, using the known flight distance (5.89 m), the speed of light and the fact that the maximum neutron energy (corresponding to the edge T_u) is 63 MeV. The number of channels between T_u and T_g and the difference between the two flight times gave the time calibration of 1.11 ns/channel. The neutron time of flight, t, as a function of channel number, T, was then calculated using the equation:

$$t = 1.11(T_u - T) + 53.7 \quad ns \qquad (3.1)$$

where: T_u = *ADC channel number of the most energetic neutrons (=184)*

The neutron energy E_n (in MeV) corresponding to the time of flight t (in ns) was calculated by using equation (2.2).

CHAPTER 4

ENERGY SPECTRUM OF NAC NEUTRON THERAPY BEAM

The measurement of the energy spectrum of the NAC neutron therapy beam, in other words the beam which enters the water phantom (or patient), is important for three main reasons. Firstly, such a measurement is required in order to determine a set of calibration data, referred to as the response matrix of the detector, required for use in the process of unfolding pulse height spectra to obtain energy spectra. Secondly, the (TOF) spectrum of the open beam was used in different ways to verify the procedures used to determine energy spectra from pulse height spectra. Thirdly, it is important to know the spectrum of the neutron beam on entering the phantom in order to assess the changes occurring in this spectrum during its passage through the water, the primary focus of the present investigation.

4.1 UNFOLDING

4.1.1 THE HEPRO UNFOLDING PACKAGE

To unfold the neutron energy spectrum, $\Phi(E_n)$, from the measured pulse height spectrum, $L(E)$, we must solve the matrix equation 2.6 (section 2.5). Rewriting equation 2.6, in inverted matrix form

$$\Phi(E_n) = R^{-1}(E,E_n)L(E) \qquad (4.1)$$

where: $\Phi(E_n) = (\Phi(1), \Phi(2), \ldots, \Phi(R))^T$ *is the energy bin vector of the neutron energy spectrum;*

$L(E) = (L(1), L(2), \ldots, L(S))^T$ *is the pulse height vector for i = 1 to S pulse height channels; and*

$R(i,j)$ = *an element of the response matrix of the NE230 detector for i = 1 to S pulse height channels for j = 1 to R energy bins.*

The superscript T indicates transposition of a matrix. i.e. $\Phi(E_n)$ *and L(E) are column vectors.*

The unfolding of a measured pulse height spectrum, say L(i), for i = 1 to S, pulse height channels, determines the set of energy bin values $\Phi(j)$, for j = 1 to R energy bins, of the energy spectrum, $\Phi(E_n)$, such that the unfolded spectrum M(i) given by

$$M(i) = \sum_{j=1}^{R} \Phi(j)R(i,j) \qquad (4.2)$$

is a "best fit" to L(i). The energy bin values of the energy spectrum, for j = 1 to R energy bins is given by

$$\Phi(j) = \int_{j-1}^{j} \Phi(E_n)dE_n \qquad (4.3)$$

Thus the energy bin values, $\Phi(j)$, give information about the energy spectrum in energy bins j.

Most matrix unfolding codes, such as LOUHI [Ro80], DIFBAS [Ti93] and LEPRICON [Ma86] used to solve equation 4.1 use algorithms based on the least squares

method. To obtain solutions from these codes which are physically meaningful, some *prior*, or *a priori*, information is required. The SAND-II code [Mc67] is a widely used code and is based on a special least square formalism which uses *prior* information only as a first input when starting the iteration procedure. The HEPRO package [Ma94] includes the GRAVEL code which contains a modified SAND-II algorithm. The GRAVEL code gives only partially acceptable solutions [Ma94] because the solutions depend on the starting spectrum and no uncertainty analysis is possible.

If the *a priori* information is incomplete, the least square method leads to difficulties since no unique solution to equation 4.1 exists. The MIEKE code [Ma94], also part of the HEPRO package, was developed for these cases. The MIEKE algorithm is based on probability arguments which uses the Monte Carlo method to construct a probability density for the solutions to equation 4.1. The probability density which would properly represent the a *priori* information, i.e. the measured data, was derived from the Bayesian theory of measurement uncertainty [We89] based on Bayesian statistics [Le89] and the principle of maximum entropy [Ja57]. The resulting probability density derived is a multivariate normal density with a chi-squared exponent. Thus the probability density numerically describes the present state of incomplete knowledge of the spectrum to be determined and requires no *prior* information about the form of the spectrum. With this probability density one can determine the most probable solution to equation 4.1, as well as the expectation values, standard deviations and confidence limits of this solution. The code was successfully used in a number of applications, including the response of a ^{3}He detector to neutrons [Di93], estimations of dose equivalents from reaction rates of Bonner spheres [Ma88] and response measure-

ments of NE213 detectors to photons [Bu93].

4.1.2 ENERGY BINS

In the present work equation 4.1, was solved for $\Phi(E_n)$ constructed with 18 energy bins. The response data of the NE230 detector to neutrons were used to construct these energy bins. This information was obtained in the form of a set of response functions (pulse height spectra), where each response function in the set is a measure of the response of the detector to neutrons of a discrete neutron energy.

Much of the detail concerning the measurement of the open beam of the NAC neutron therapy beam has already been described in section 3.5. The energy bins were defined in terms of the neutron time of flight, T_n (see figure 3.7). The time of flight scale, between 145.4 - 52.7 ns, was divided into 18 time bins of equal width (5.2 ns). The distribution in figure 4.2.1 is a schematic representation of the perspective plot of counts versus pulse height, L, and time of flight, T_n (see figure 3.6) where the horizontal lines illustrate how the time of flight parameter was divided into the 18 time bins. The corresponding time bin centres were each calibrated to neutron energy, using equations 2.2 and 3.1. Each time bin of equal width corresponds to an energy bin. However, each consecutive energy bin have a different energy width. Table II displays the results obtained.

TABLE II Results of neutron energy calibration of the time bins.

j	j centres (T_n-channel no.)	j central $E_n(j)$ (MeV)
1	975	8.86
2	1025	9.58
3	1075	10.3
4	1125	11.1
5	1175	12.2
6	1225	13.2
7	1275	14.5
8	1325	15.9
9	1375	17.6
10	1425	19.5
11	1475	21.8
12	1525	24.5
13	1575	27.7
14	1625	31.5
15	1675	36.3
16	1725	42.2
17	1775	49.8
18	1825	59.5

4.1.3 THE RESPONSE MATRIX DETERMINATION, ILLUSTRATION AND DISCUSSION

The events selected by each cut (energy bin) on the LT_n-plane were projected onto the L-axis. Eighteen response functions were obtained, each of i = 1 to 200 pulse height channels. These response functions were then assembled into a 200x18 matrix, the response matrix for the NE230 detector for neutrons.

Figure 4.1 shows the eighteen response functions of the response matrix. The peak which corresponds to the forward recoiling deuterons, D_f (see figure 3.6), is clearly identifiable in response functions 1-11. It can be seen in these response functions that the peak D_f shifts to higher pulse heights with increasing neutron energy. In response functions 12 to 18 the peak D_f starts to diminish and the peak, D_g, attributed to deuterons from the $^{12}C(n,d)^{11}B$ reaction becomes more visible. It can also be observed in these response functions that as the neutron energy increases, the peak D_g shifts towards the peak D_f until they overlap at high neutron energy. This is the result of the kinematic effect caused by the relatively larger increase in the energy of the outgoing deuterons from the $^{12}C(n,d)^{11}B$ reaction compared to the increase in the energy of the forward recoil deuterons in the detector. We can also see that in the response functions the peaks D_f and D_g diminish with increasing neutron energy. This is because as the neutron energy increases the range of the recoiling deuterons in the detector medium increases. For example the ranges for 15 MeV, 30 MeV and 55 MeV deuterons are respectively, 0.14 cm, 0.66 cm and 1.48 cm in the NE230 detector. These ranges are respectively 5.7%, 26.4% and 59.2% of the size of the detector diameter, meaning that a large fraction of deuterons escapes through the walls of the detector with increasing neutron energy. This effect distorts the response functions of the NE230 detector significantly at high energies. Note however that an even larger effect would occur if a NE213 detector of the same size were used. For,example, since the range of a 50 MeV proton in NE213 is 2.49 cm, all protons above this energy would escape from the detector before coming to rest.

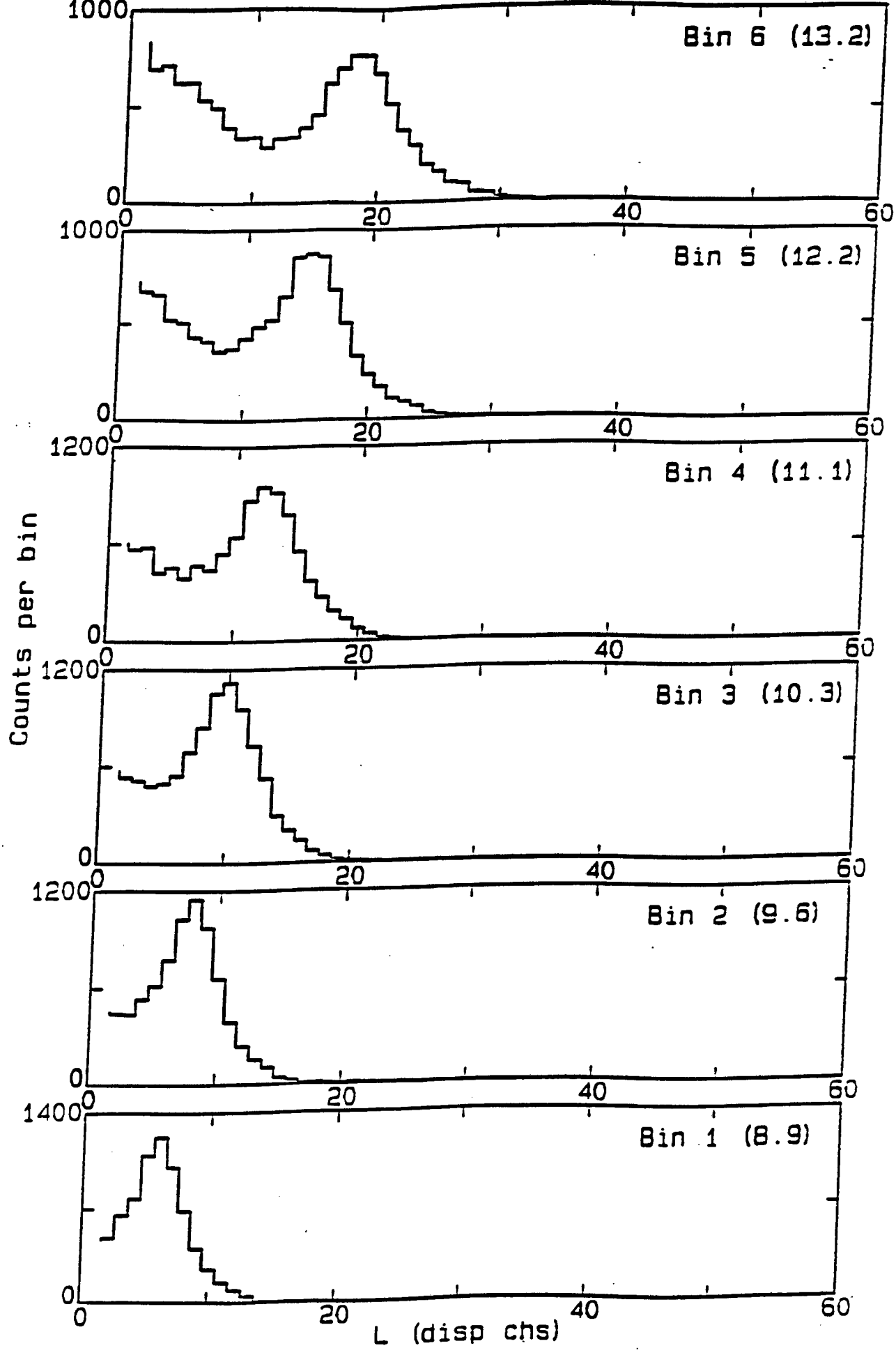

Figure 4.1 The eighteen (3x6) response functions of the NE230 spectrometer for neutrons, used in the MIEKE analysis. The energy bin number and the neutron energy (see table III) is given with each response function.

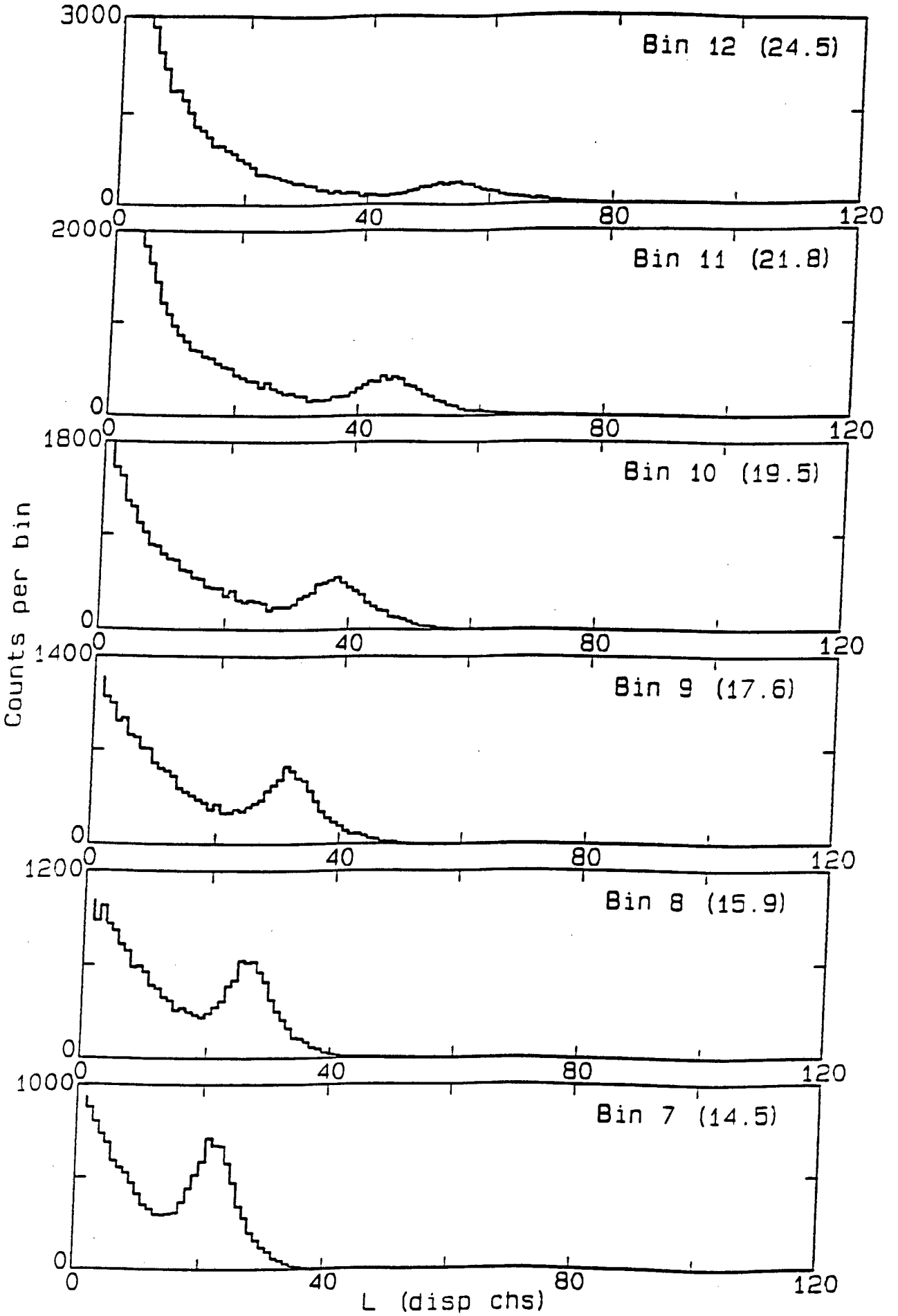
Bin 12 (24.5)
Bin 11 (21.8)
Bin 10 (19.5)
Bin 9 (17.6)
Bin 8 (15.9)
Bin 7 (14.5)
Counts per bin
L (disp chs)
3000
2000
1800
1400
1200
1000
0
40
80
120

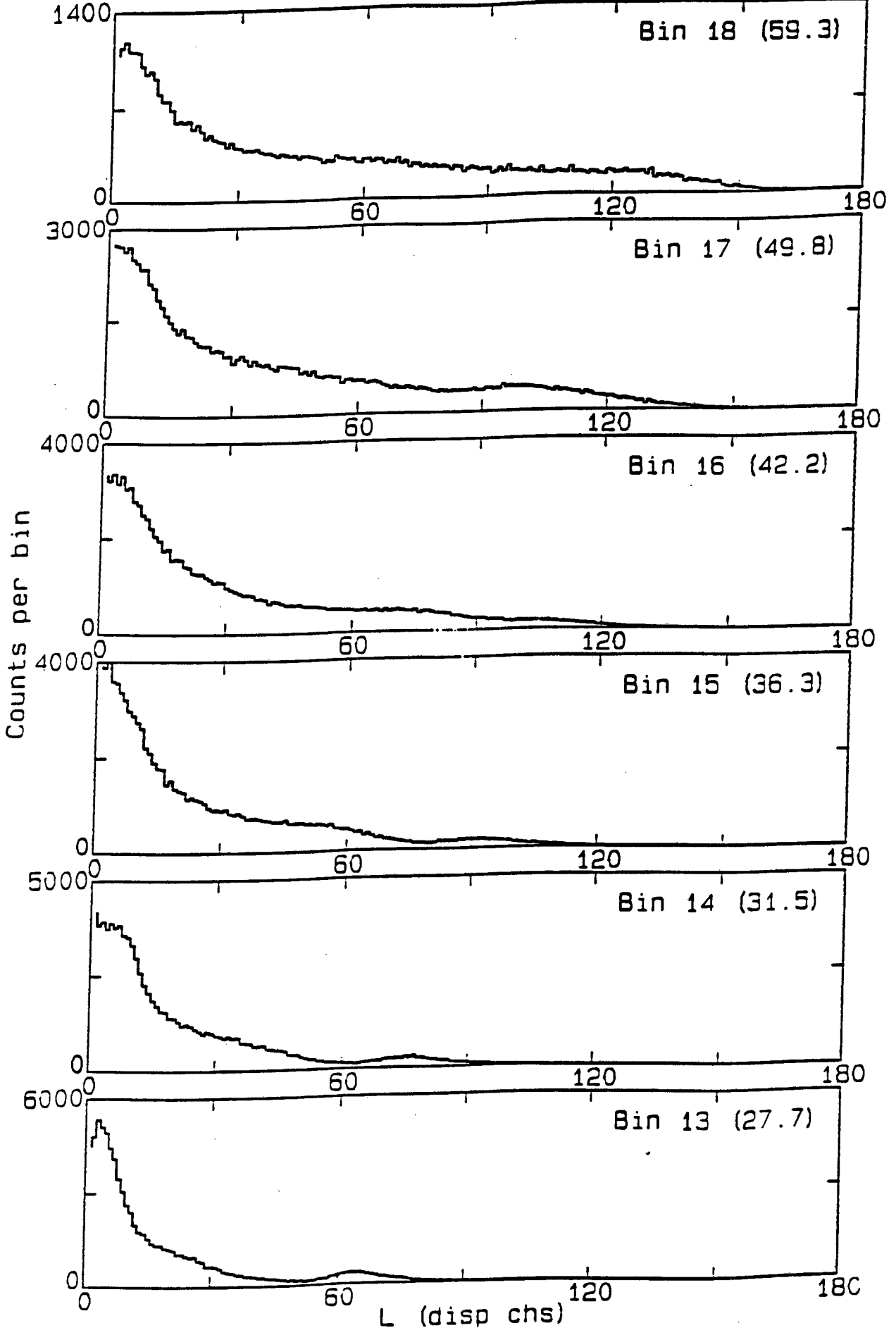
Bin 18 (59.3)
Bin 17 (49.8)
Bin 16 (42.2)
Bin 15 (36.3)
Bin 14 (31.5)
Bin 13 (27.7)
Counts per bin
L (disp chs)
0
60
120
180
1400
3000
4000
4000
5000
6000

4.2 TESTS OF THE UNFOLDING PROCEDURES

4.2.1 DETERMINATION OF THE TOF SPECTRUM OF THE OPEN BEAM USING MIEKE

Figure 4.2.1 shows the density plot of the LT_n-plane for the open beam measurement. The projection of the rows of the response matrix onto the T_n-axis gives the TOF spectrum of the open beam which is shown figure 4.2.2. The pulse height spectrum of this beam, shown in figure 4.2.3, was obtained by projecting the events selected in the LS-plane by the deuteron cut onto the L-axis. The TOF spectrum and pulse height spectrum are clearly related to one another because they were generated from the same data. This is very useful because we can check whether the TOF spectrum obtained by unfolding the pulse height spectrum, using the code MIEKE [Ma94], is in agreement with the measured TOF spectrum.

The MIEKE code was used to unfold the pulse height spectrum for the open beam, L(i), for i = 1 to 200 pulse height channels. A set of energy bin values, $\Phi(j)$, were determined for j = 1 to 18 energy bins, of the TOF spectrum, such that calculated M(i) is a "best fit" to L(i). If the MIEKE analysis of TOF spectrum of the open beam was reliable we would expect the measured spectrum and the derived spectrum to be in good agreement because the pulse height spectrum and response matrix used in the unfolding was determined from the same data.

The chi-squared per degrees of freedom value of 4.55 determined for the unfolding process indicate that the $\Phi(j)$ values, for the j = 1 to 18 energy bins, deter-

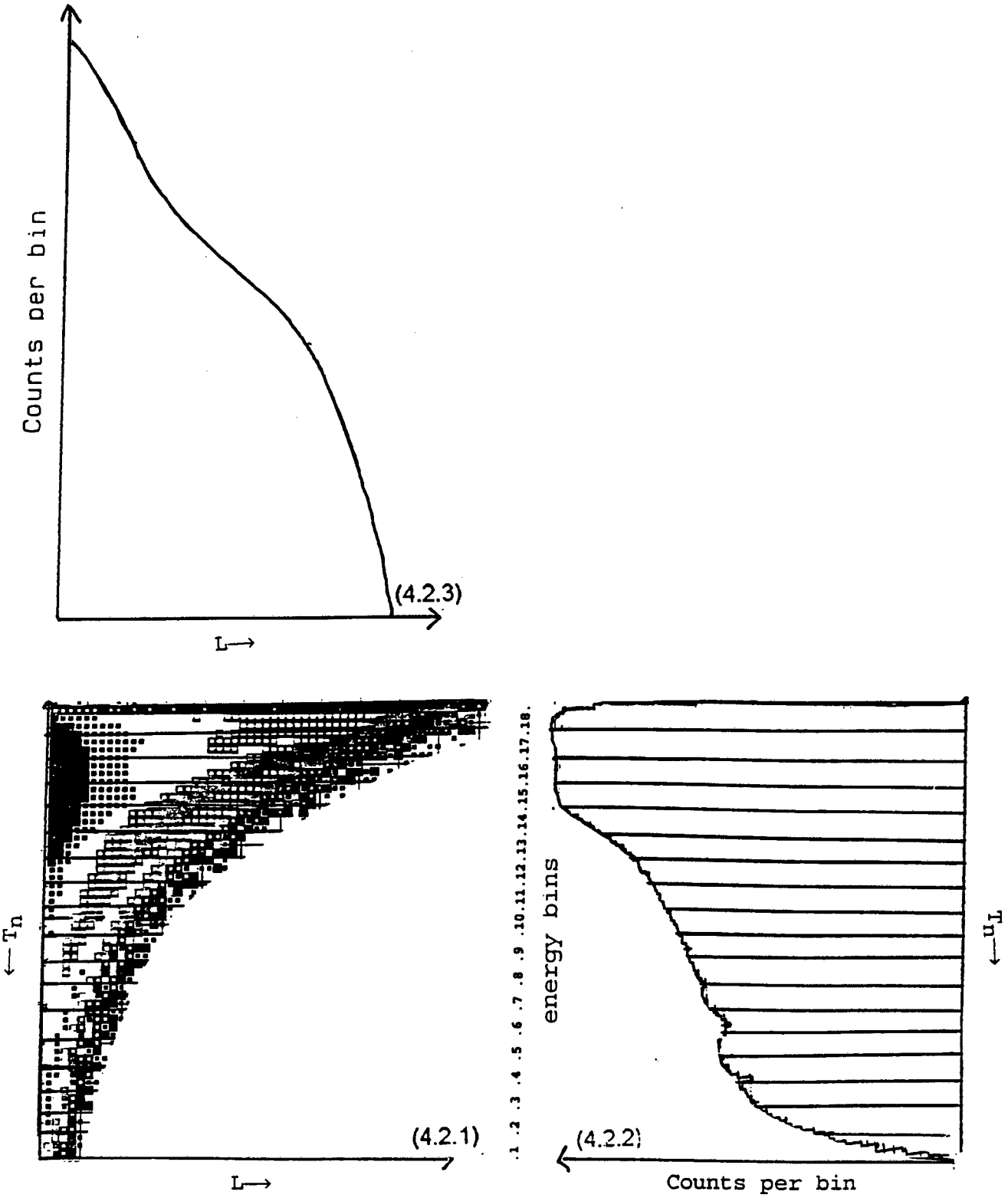

Figures 4.2.1-4.2.3 Schematic representations of the LT_n-plane (4.2.1), illustrating the relationship between the T_n-spectrum (4.2.2) and the L-spectrum (4.2.3) of the open beam. The horisontal lines show the divisions between the 18

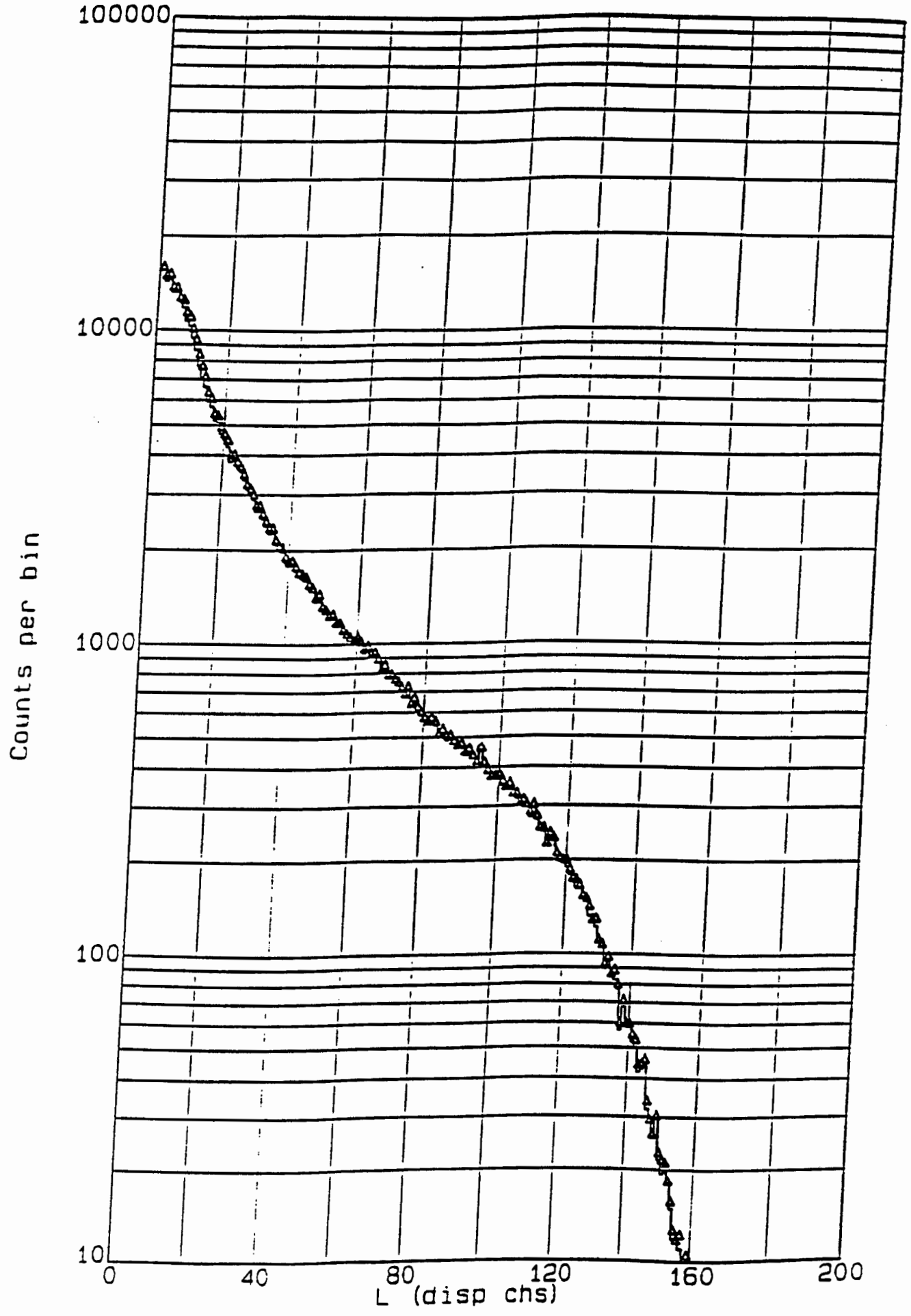

Figure 4.3.1 Measured pulse height spectrum (histogram) compared with the spectrum derived by MIEKE analysis (triangles) for the data obtained in the open beam.

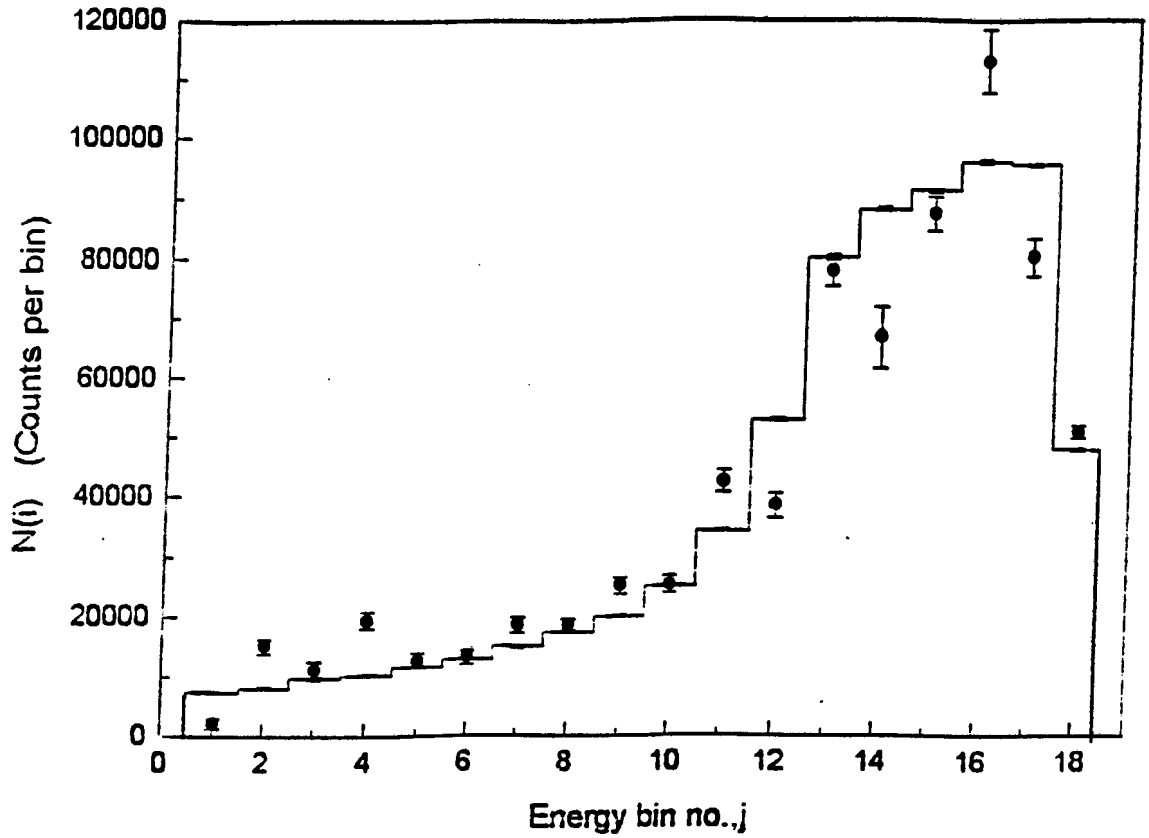

Figure 4.3.2 Measured TOF spectrum (histogram) compared with the spectrum derived by MIEKE analysis (solid circles) for the data obtained in the open beam run.

mined for the TOF spectrum are in agreement with the measured data used to derive them. The results obtained by MIEKE analysis and measurement are shown for comparison in figures 4.3.1-4.3.2. Figure 4.3.1 shows that the "best fit" to the measured pulse height spectrum derived by MIEKE analysis and the actual measured spectrum is in excellent agreement. Figure 4.3.2 shows the corresponding TOF spectrum derived by MIEKE analysis and the measured TOF spectrum. The figure shows that the measured spectrum is well reproduced in shape by the MIEKE analysis. However, the MIEKE derived TOF spectrum have systematic fluctuations in it. Also, the spectrum is in good agreement with the measured spectrum, except for energy bins ,2 ,4 ,12, 14 16 and 17. The possible reasons for this will be discussed below in section 4.3.

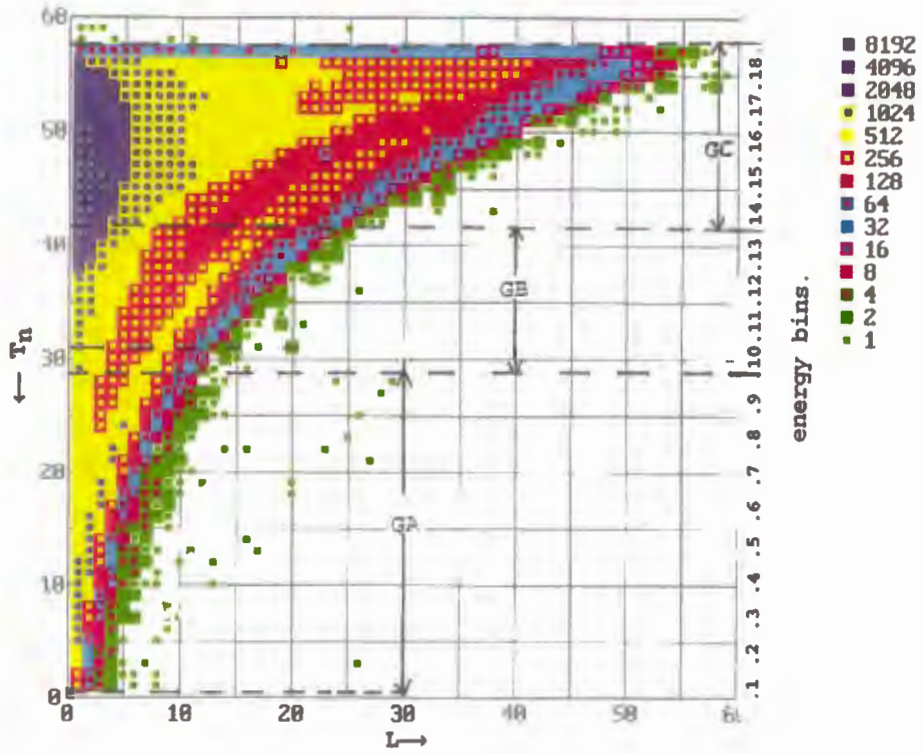

Figure 4.4.1 Density plot of the LT_n-plane, illustrating how the broader energy groups GA, GB and GC were constructed using the 18 energy bins.

4.2.2 ADDITIONAL TEST SPECTRA

The determination of the TOF spectrum from the pulse height spectrum for the open beam measurement provided one test of the unfolding process using MIEKE. Further tests were devised to check the reliability of MIEKE to provide the energy spectra. In these tests three broad energy groups GA, GB and GC were defined at " low ", " intermediate " and " high " neutron energies by combining the events in energy bins 1-9, 10-13 and 14-18 respectively, as shown together in figure 4.4.1. Three projected pulse height spectra were then generated for each one of these groups and a fourth spectrum generated from the sum of the events in GA and GC. These four pulse height spectra are shown in figure 4.4.2.

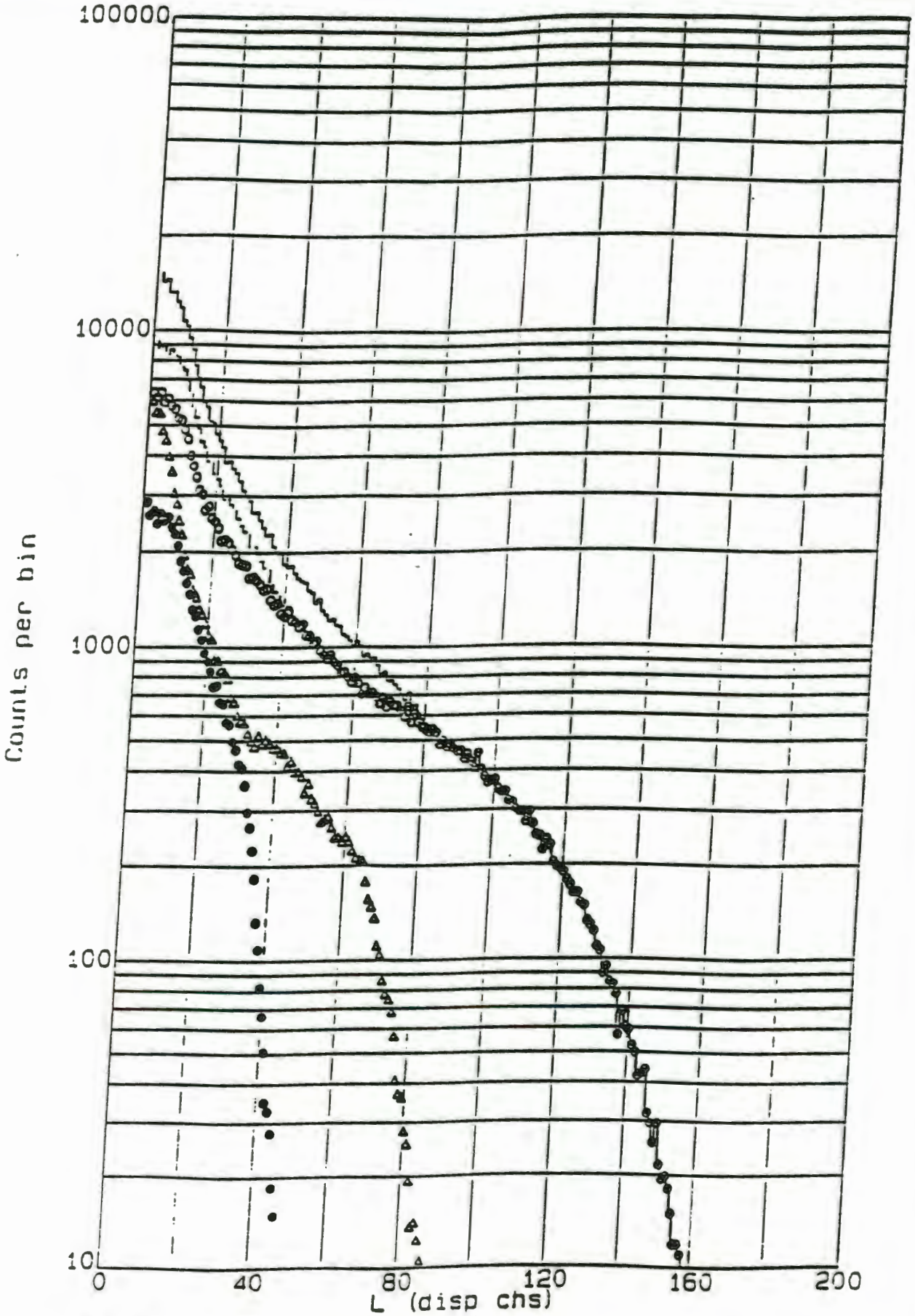

Figure 4.4.2 Pulse height spectrum measured in the open beam (histogram) shown together with the pulse height spectra obtained by selecting only events in the energy groups (see figure 4.4.3) GA (solid circles), GB (triangles), GC (open circles) and GA+GC (dashed histogram) respectively.

The figure shows that the spectra are of different pulse height ranges (neutron energies) which is in agreement with the cuts (energy groups) selected on the LT_n-plane as shown in figure 4.4.1. These spectra were then unfolded, using MIEKE analysis as for the spectrum of the beam.

Table III. The chi-squared per degrees of freedom values determined by MIEKE analysis for the spectra in the energy groups, GA, GB, GC and GA + GC respectively.

$\Phi(E_n)$	χ^2/dof
GA	1.20
GB	1.64
GC	3.36
GA+GC	3.81

The results were then plotted as in the open beam analysis of the TOF spectrum and are shown in figures (4.5.1-4.5.4) and (4.6.1-4.6.4). Figures 4.5.1-4.5.4 show that the "best fits" to the measured pulse height spectra derived by MIEKE analysis and the actual measured spectra are in excellent agreement for each of the groups. Figures 4.6.1-4.6.4 show that the corresponding energy spectra derived by MIEKE analysis are well reproduced in shape for each of the energy groups. Small systematic fluctuations can also be seen in each of the spectra but they are in general good agreement with the measured spectra for these groups.

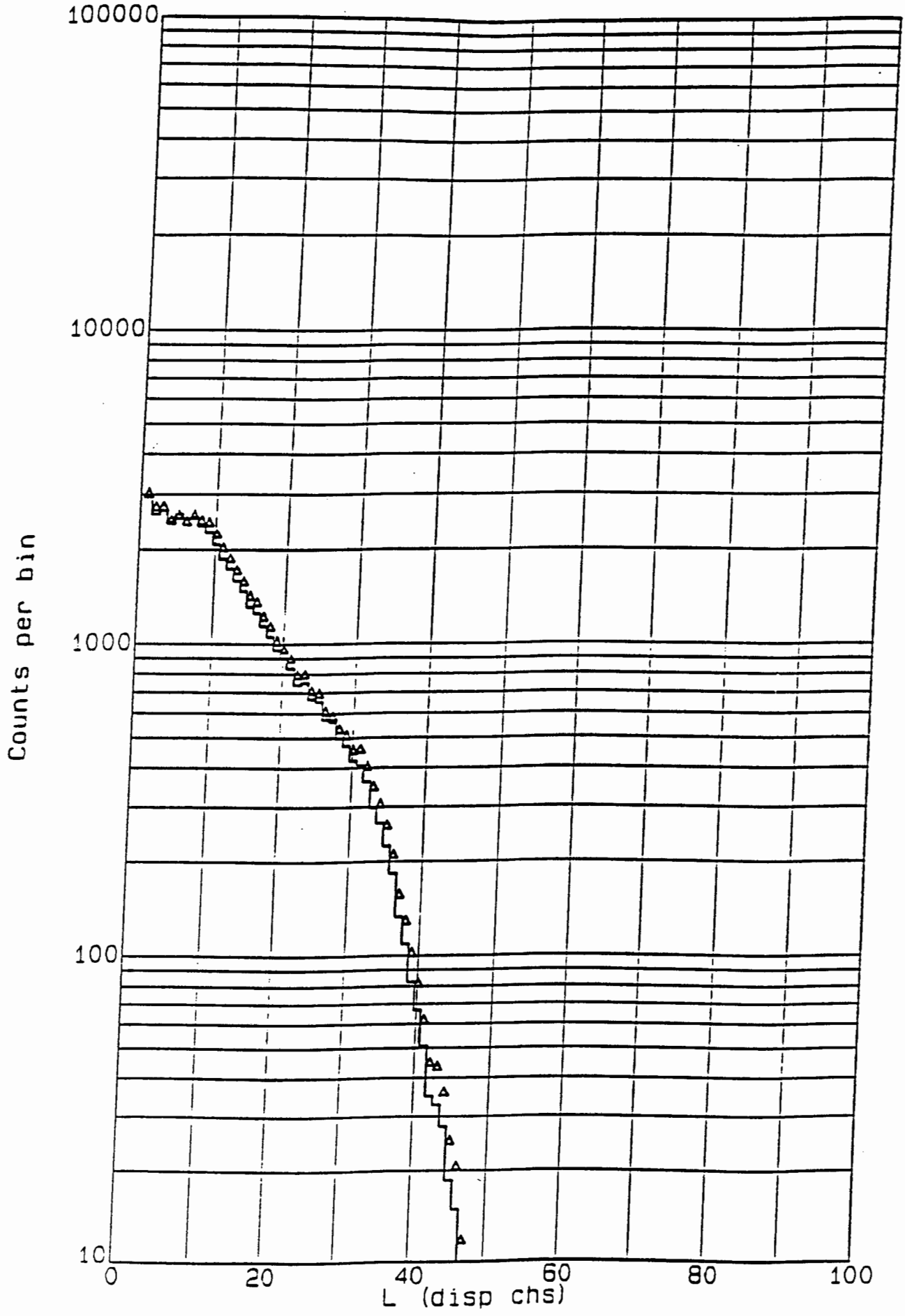

Figure 4.5.1 Comparison as in figure 4.3.1 for the spectrum obtained selecting energy group, GA.

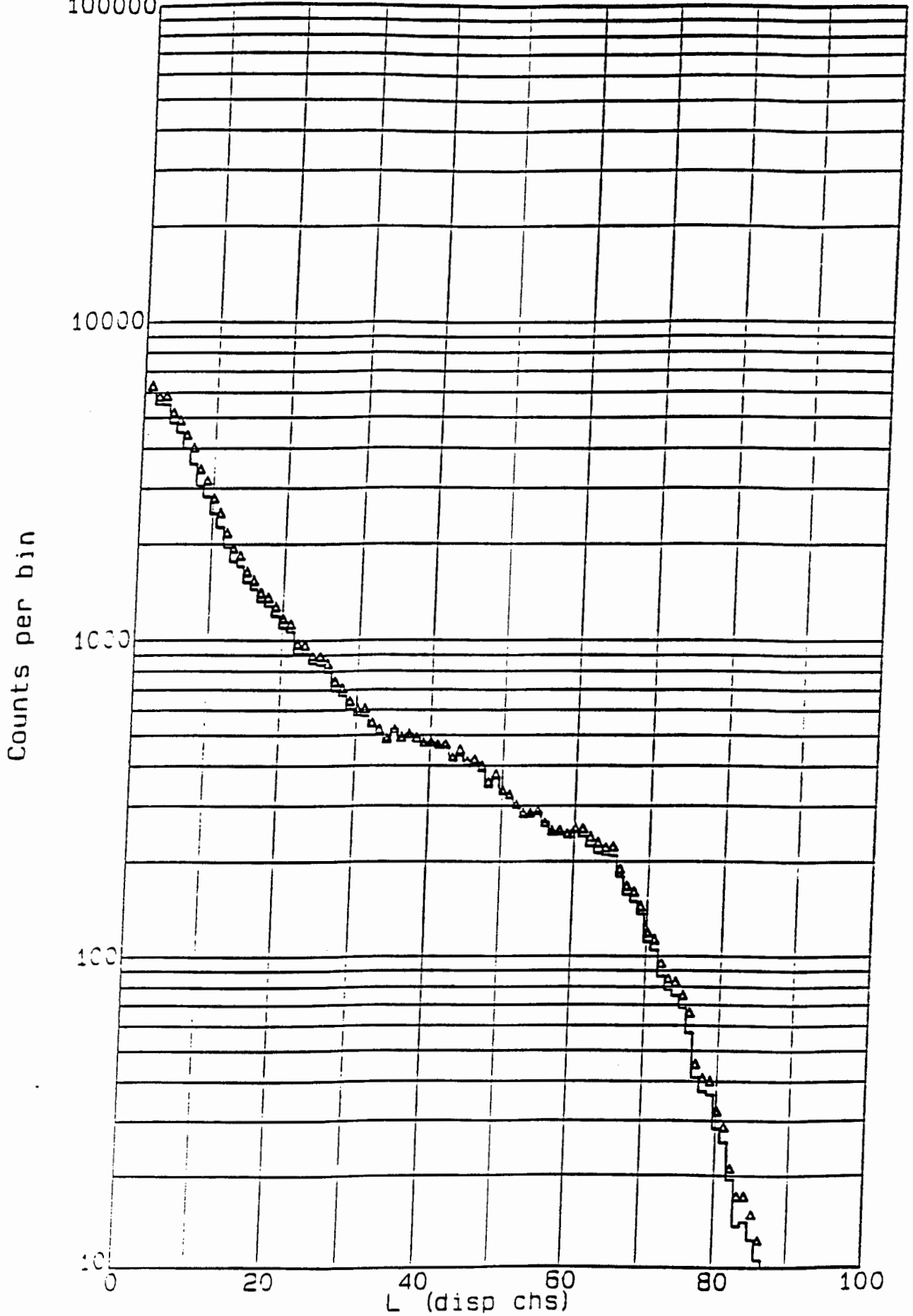

Figure 4.5.2 Comparison as in figure 4.3.1 for the spectrum obtained selecting energy group, GB.

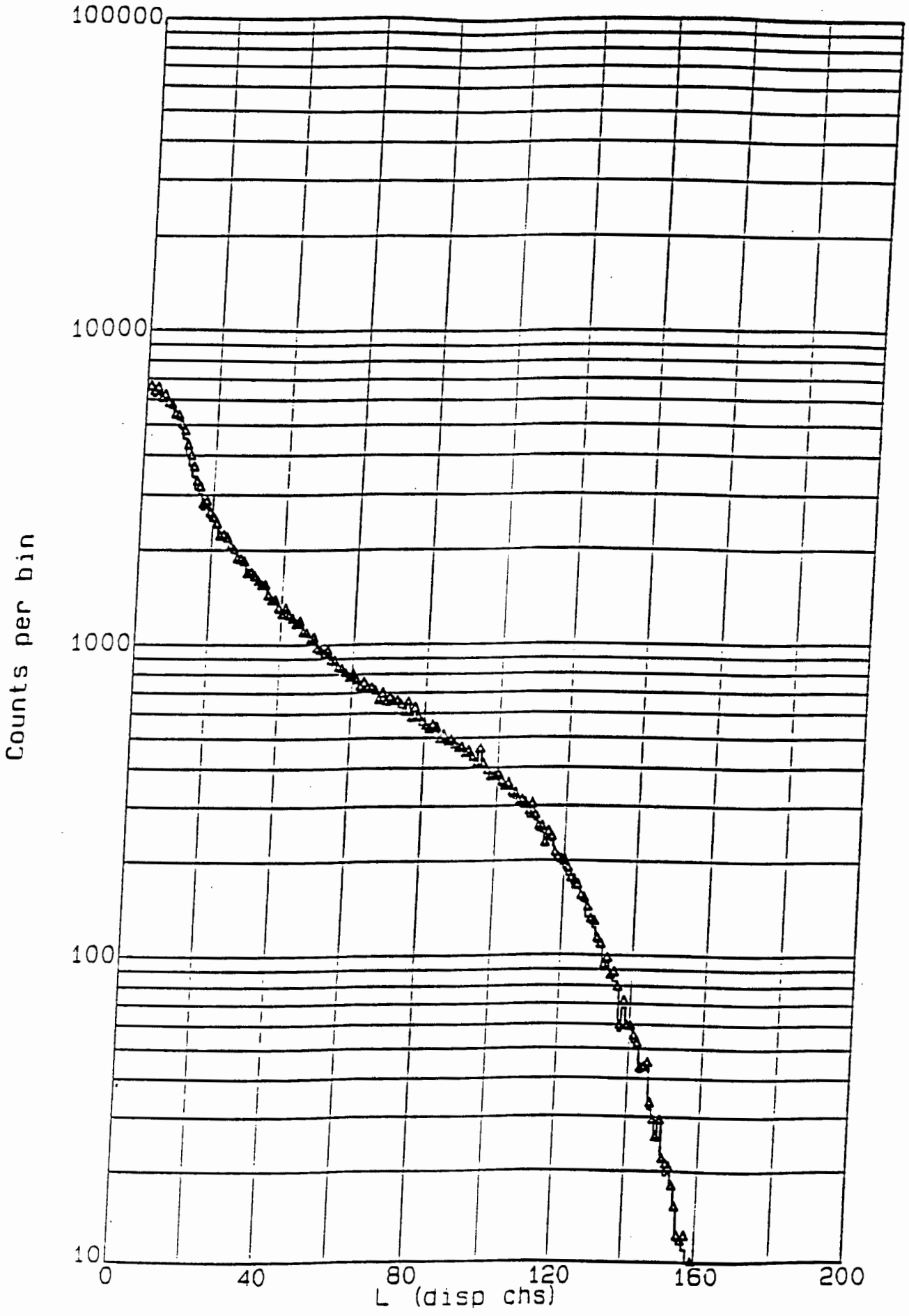

Figure 4.5.3 Comparison as in figure 4.3.1 for the spectrum obtained selecting energy group, GC.

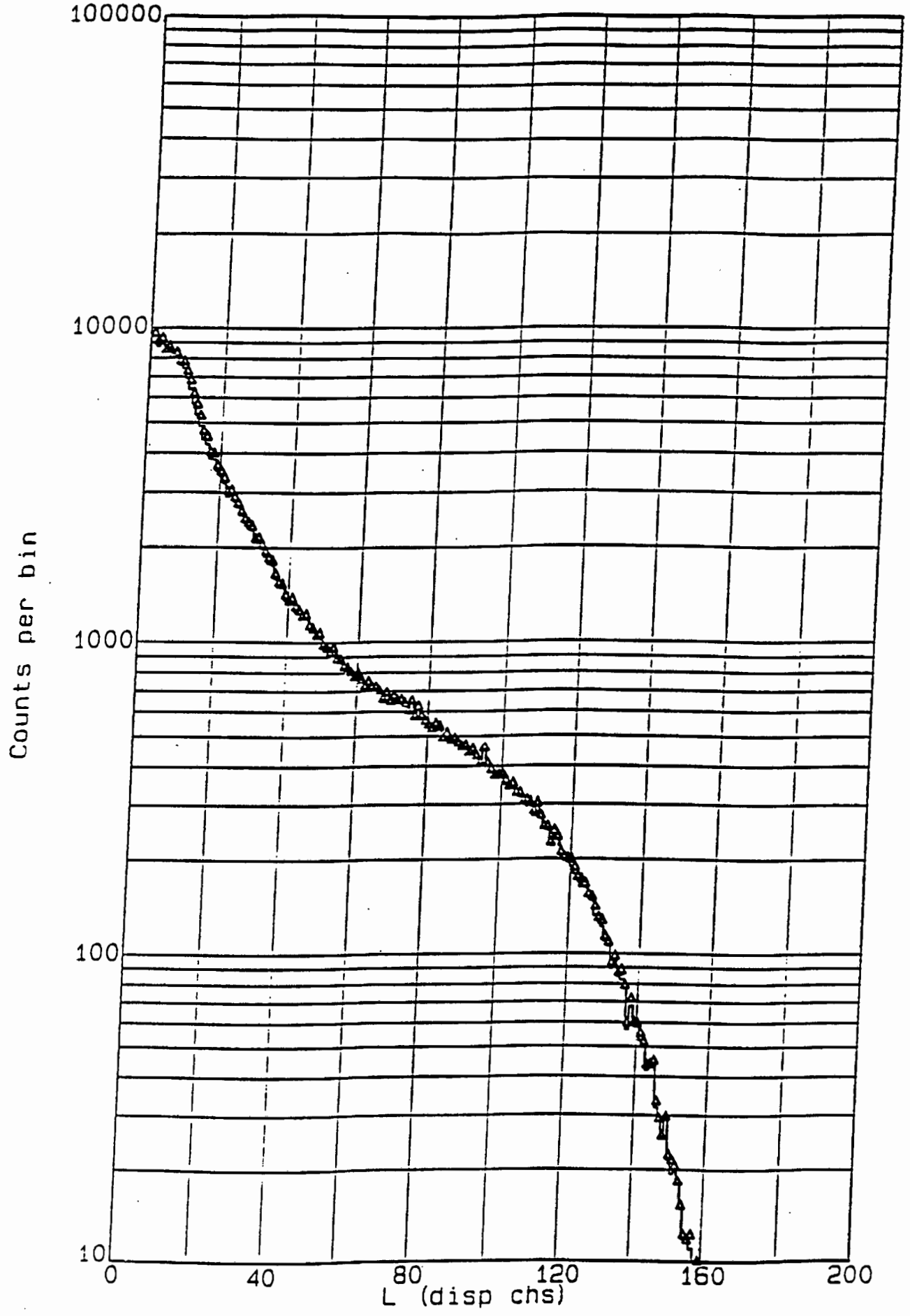

Figure 4.5.4 Comparison as in figure 4.3.1 for the spectrum obtained selecting energy group, GA+GC.

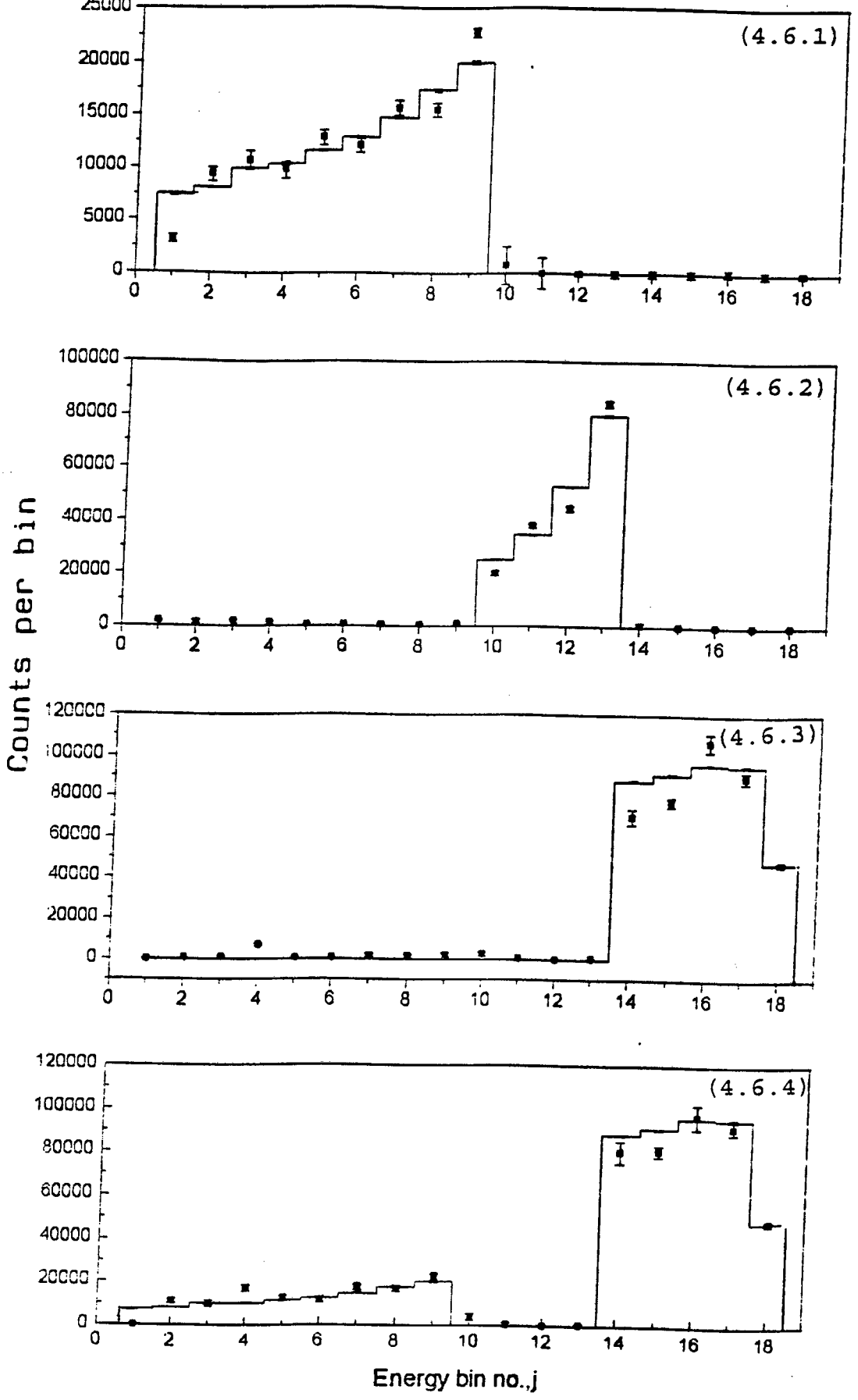

Figures 4.6.1-4.6.4 Neutron spectrum measured in the open beam (histogram) shown together with neutron spectra (solid circles) obtained by selecting only events in the energy groups (see figure 4.3.1) GA (4.6.1), GB (4.6.2), GC (4.6.3) and GA+GC (4.6.4) respectively.

4.3 CONCLUSION

From all the tests performed it was concluded that the MIEKE analysis would be reliable in determining the energy spectrum from measured pulse height spectrum However, the results did indicate that the energy spectrum also contained some systematic fluctuations. When the spectrum was unfolded for all 18 energy bins these fluctuations increased for energy bins 2, 6, 12, 14, 16 and 17. These systematic fluctuations could be attributed to high energy deuterons escaping through the walls of the detector and protons and alphas which were not excluded by the deuteron cut on the LS-plane. The effect would be to introduce distortions in the response functions 12-18 at lower energies which would result in the differences in the counts per pulse height bin for response functions 1-11 and 12-18 as shown in figure 4.1. This may lead MIEKE to overestimate the spectra in the energy bins 2, 4 and 16 and, underestimate it in 12, 14 and 17. However, for this work the agreement between the MIEKE derived energy spectrum and the measured energy spectrum is adequate because we are interested mainly in the changes in the shape of the energy spectrum.

CHAPTER 5

MEASUREMENTS OF NEUTRON ENERGY SPECTRA IN THE WATER PHANTOM

The results presented in Chapter 4 demonstrated that the neutron spectra determined, using MIEKE, from the pulse height spectra measured for the open beam (run 49) are consistent with those obtained directly from the TOF measurement made during that run. This lends confidence that this unfolding process would be reliable for determining neutron energy spectra from measurements of pulse height spectra, and more specifically encourages the possibility that the unfolding method could be useful to determine neutron energy spectra as a function of position within a water phantom. The time of flight method is unsuitable for such measurements for the reasons outlined in Section 2.5.

Pulse height spectra were therefore measured as a function of position and other parameters such as collimator settings (field size) and beam filter geometry in a water phantom (60x60x60 cm^3) and the results were analysed using MIEKE. These measurements and analyses are described in this chapter.

5.1 MEASUREMENTS OF DEUTERON PULSE HEIGHT SPECTRA IN THE WATER PHANTOM

Pulse height spectra were measured with the detector system (NE230 scintillator) immersed in the water phan-

tom, using exactly the same electronics and method as for the open beam measurement, run 49, as described in sections 3.1 and 3.2 . The detector was inserted into a thin latex sheath to ensure that it was completely water tight (see figure 3.1.2). Measurements were made as a function of the following variables (see figure 3.1.1)

(a) depth, d, within the phantom along beam axis, measured from the face closest to the neutron source, for d = 8 to 36 cm;

(b) lateral position x relative to the beam axis, for x = 0 and 22 cm;

(c) field size 10x10 cm^2 or 29x29 cm^2, referred to as a = 10 or 29 respectively; and

(d) the different beam filters, referred to as F_1, F_2 and H (see section 2.4).

Table IV Summaries of the different measurements made for the runs in the phantom.

Run #	d (cm)	x (cm)	a (cm)	Filters
52	8	0	10	F1
53	15	0	10	F1
54	22	0	10	F1
55	29	0	10	F1
56	36	0	10	F1
57	8	0	29	F1, F2
59	22	0	29	F1, F2
60	36	0	29	F1, F2
61	8	0	10	H, F1
62	8	22	10	F1

Each measurement, except run 62, was processed in the same way as for the open beam measurement (see section 3.3), that is by applying the deuteron cut in the LS-plane to select deuteron events and projecting these events onto the L-axis to obtain the pulse height spectrum. Run 62 could not be processed due to technical problems encountered with the data. The resulting pulse height spectra, obtained from runs 52-61 are shown in figures 5.1.1-5.1.9. To facilitate comparisons between different spectra each spectrum (shown by circles) is plotted together with run 49, the open beam spectrum (shown by the histogram). Each spectrum is normalised to the same total number of counts as for run 49. Hence, these plots show directly, but qualitatively, the effect of the water environment on the neutron spectrum. For example, Figure 5.1.1 shows that the pulse height spectrum at depth 8 cm has fewer high-L pulses, and more low-L pulses, than the open beam spectrum. This means that the spectrum at depth 8 cm is poorer in high energy neutrons and richer in low energy neutrons, in other words that it is a " softer" spectrum. Figures 5.1.1-5.1.8 show that for both the 10x10 cm^2 and 29x29 cm^2 fields, that the "softening" of the beam spectrum diminishes with increasing depth, until at d = 36 cm it appears to again be very similar to the open beam spectrum.

5.2 DERIVATION OF THE NEUTRON SPECTRA USING MIEKE

The MIEKE code was used to determine neutron spectra from the pulse height spectra obtained in runs 52-61 (see figures 5.1.1-5.1.9). As described in section 4.1 the response matrix used for the unfolding was a 200x18 matrix derived from the open beam measurement (run 49). The element R(i,j) expresses pulse height spectra in

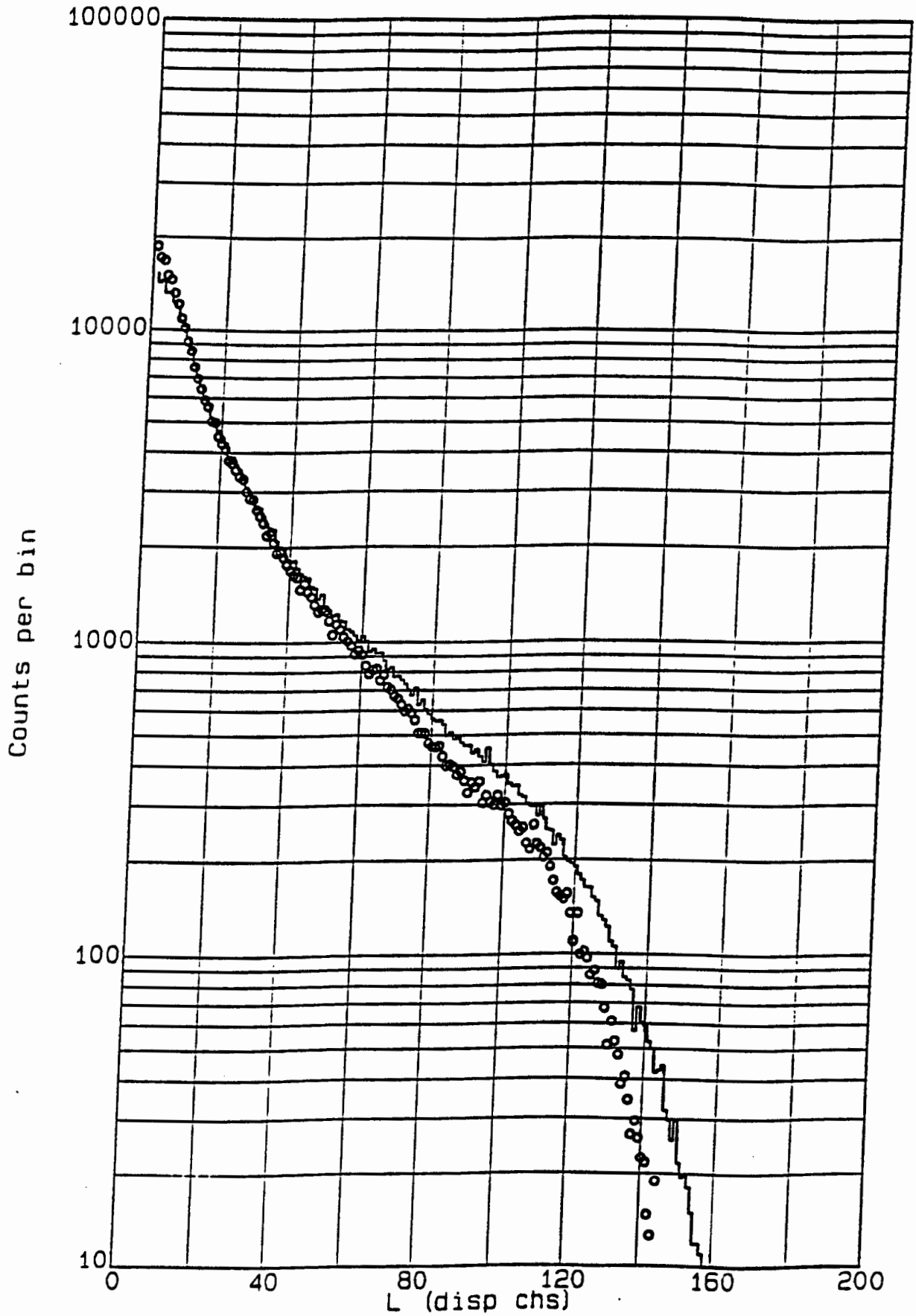

Figures 5.1.1 Pulse height spectrum measured in the open beam (histogram) compared with the spectrum (open circles) in the phantom at position, (d,x) = (8,0) cm for a = 10 cm with F1.

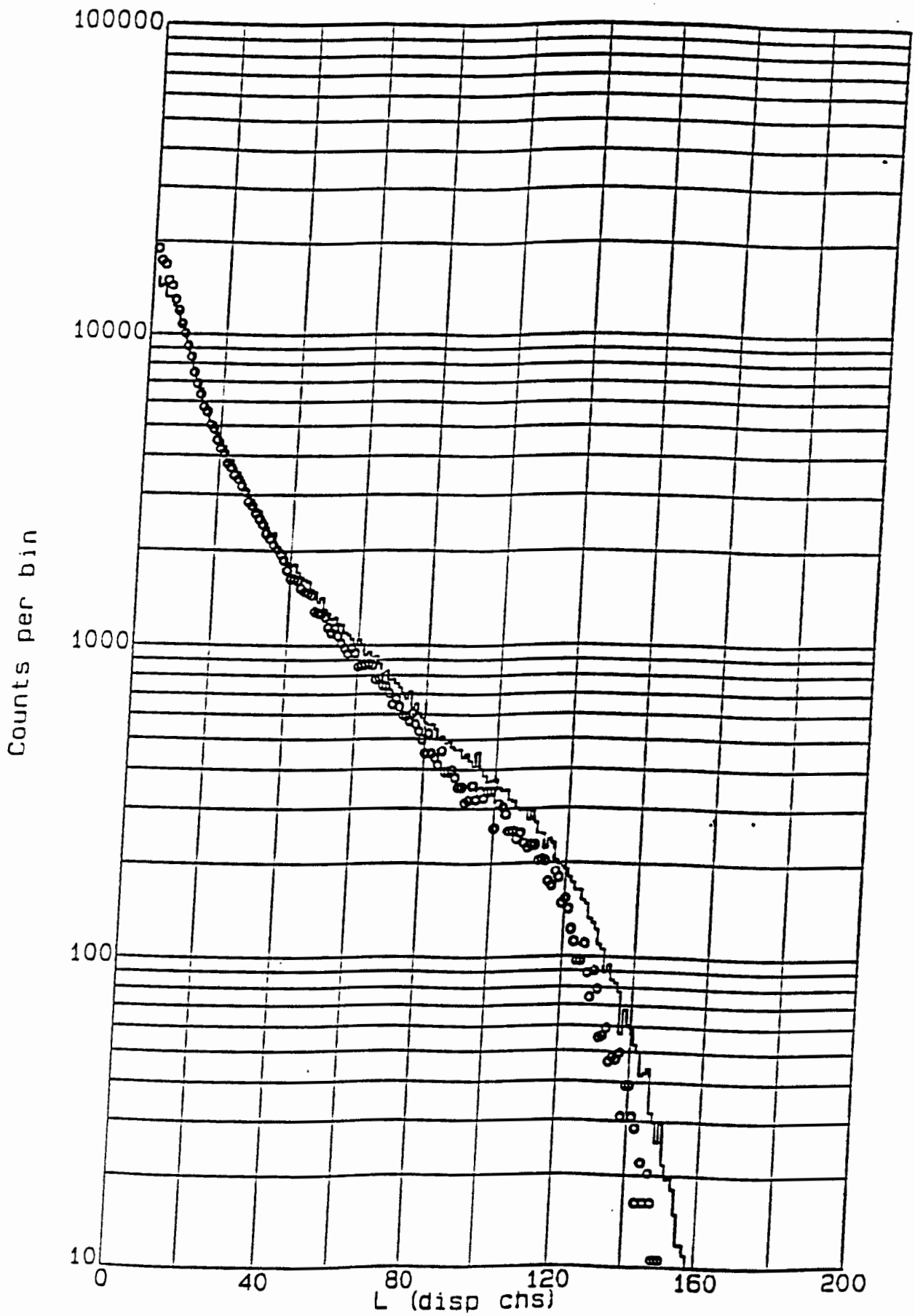

Figure 5.1.2 Comparison as in figure 5.1.1 for the spectrum measured at (d,x) = (15,0) cm for a = 10 cm with F1.

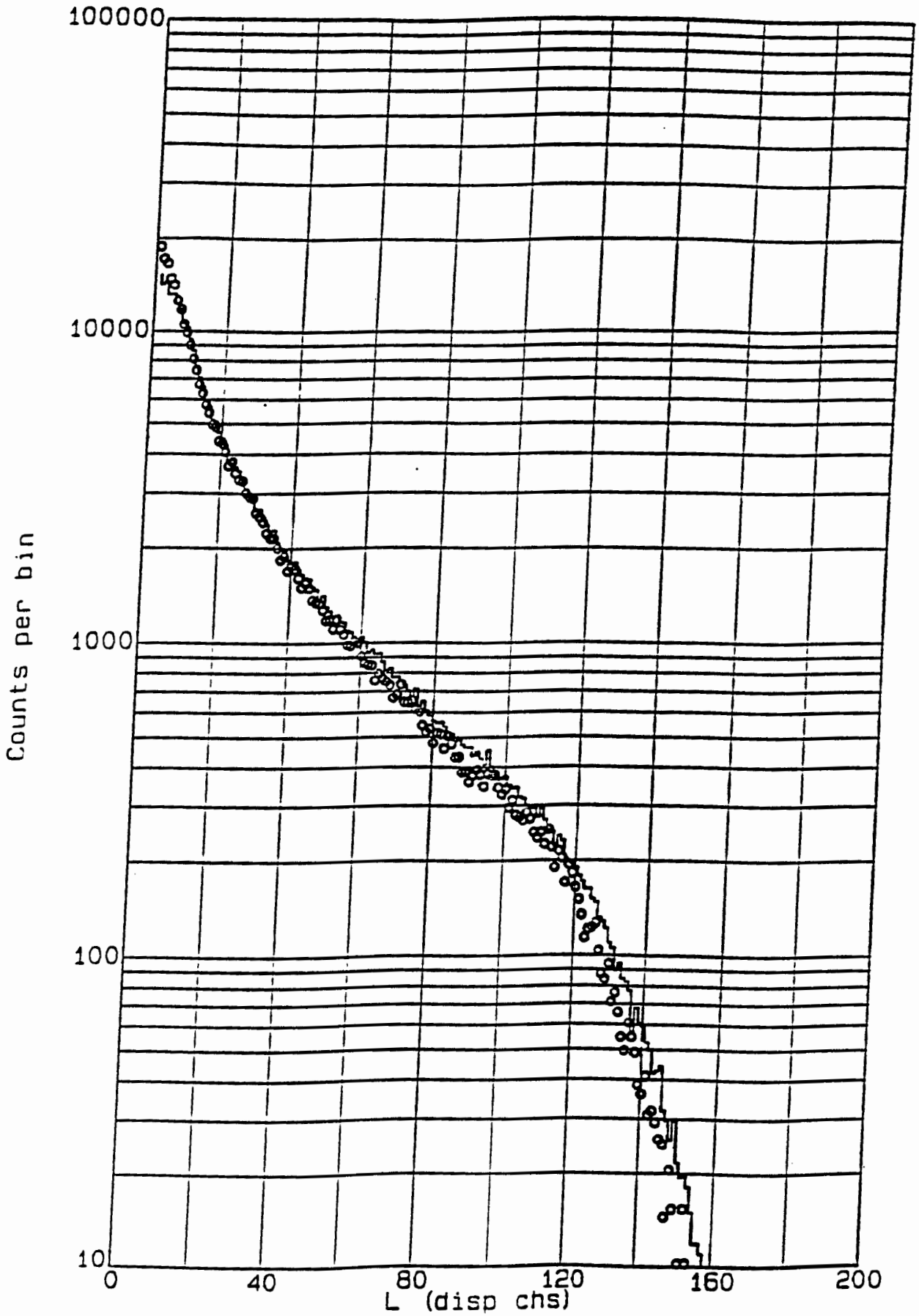

Figure 5.1.3 Comparison as in figure 5.1.1 for the spectrum measured at (d,x) = (22,0) cm for a = 10 cm with F1.

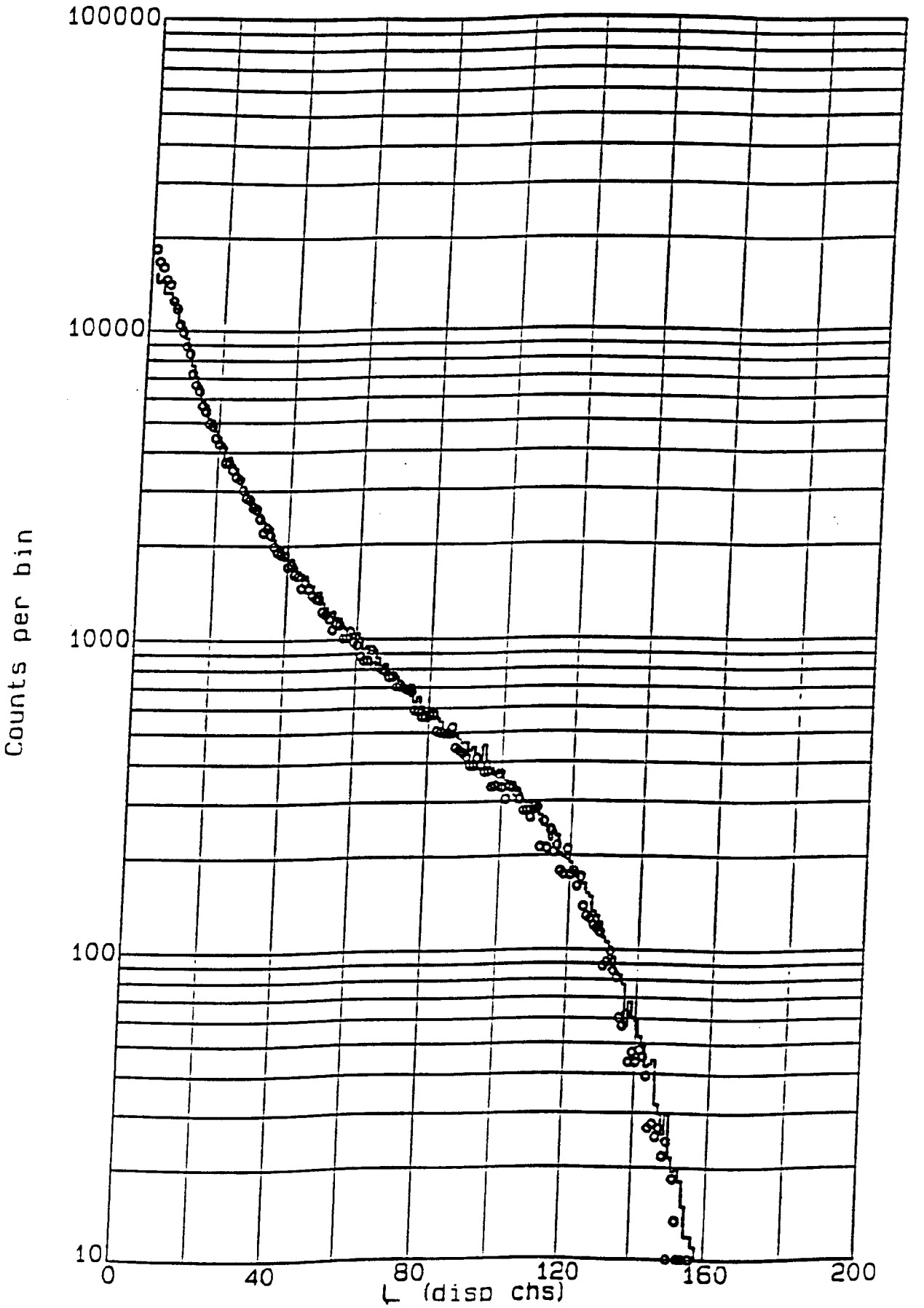

Figure 5.1.4 Comparison as in figure 5.1.1 for the spectrum measured at (d,x) = (29,0) cm for a = 10 cm with F1.

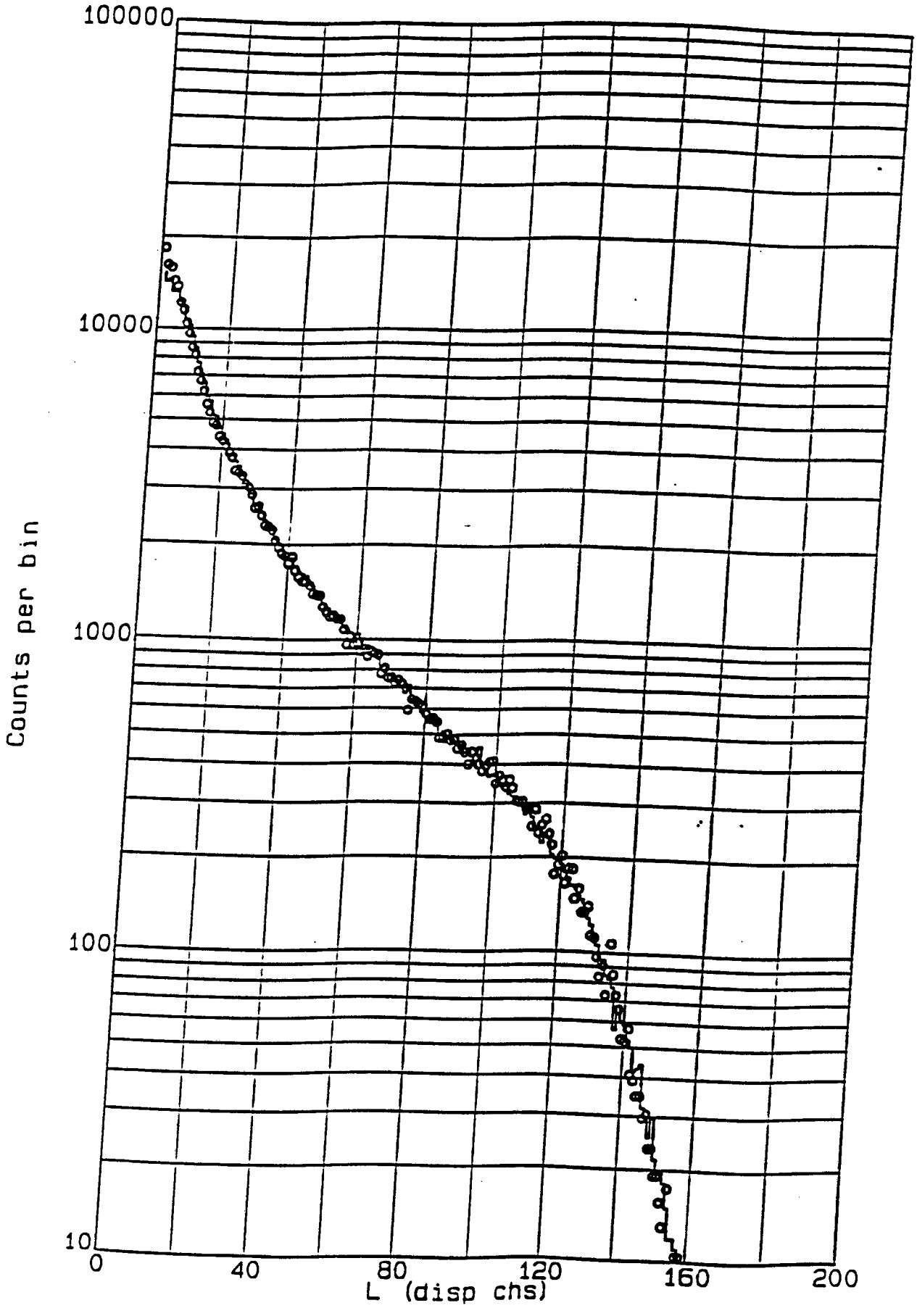

Figure 5.1.5 Comparison as in figure 5.1.1 for the spectrum measured at (d,x) = (36,0) cm for a = 10 cm with F1.

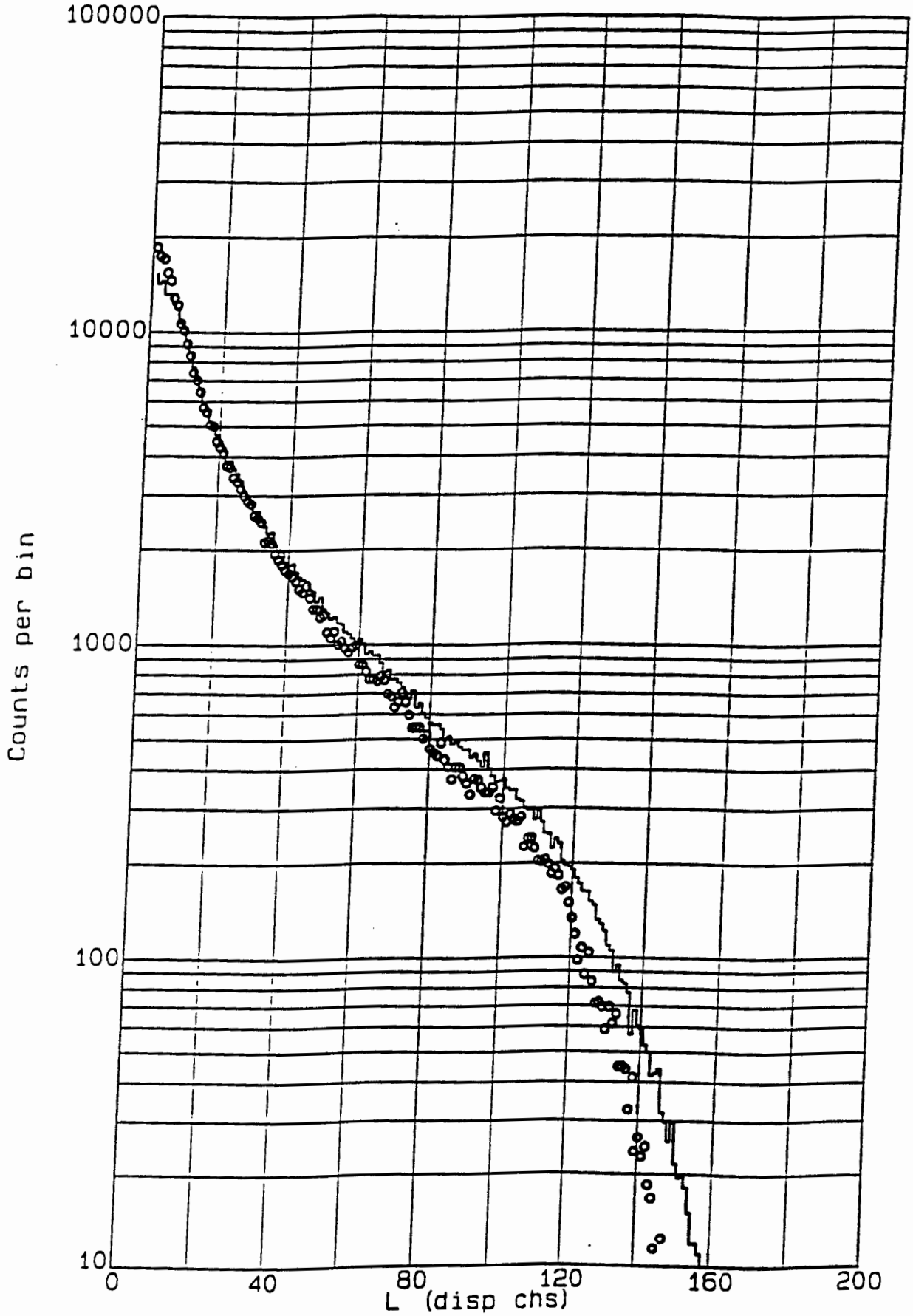

Figure 5.1.6 Comparison as in figure 5.1.1 for the spectrum measured at (d,x) = (8,0) cm for a = 29 cm with F1, F2.

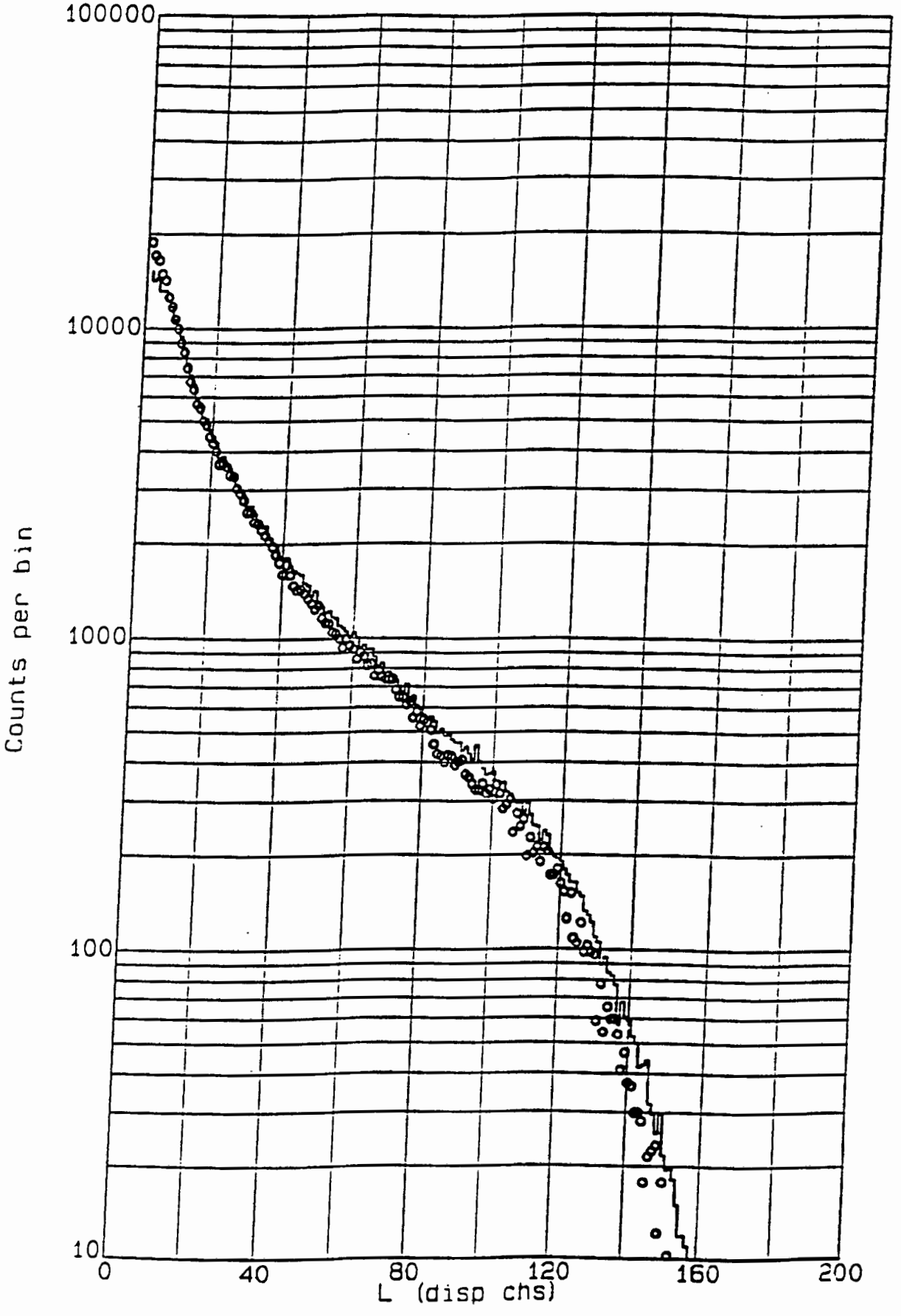

Figure 5.1.7 Comparison as in figure 5.1.1 for the spectrum measured at (d,x) = (22,0) cm for a = 29 cm with F1, F2.

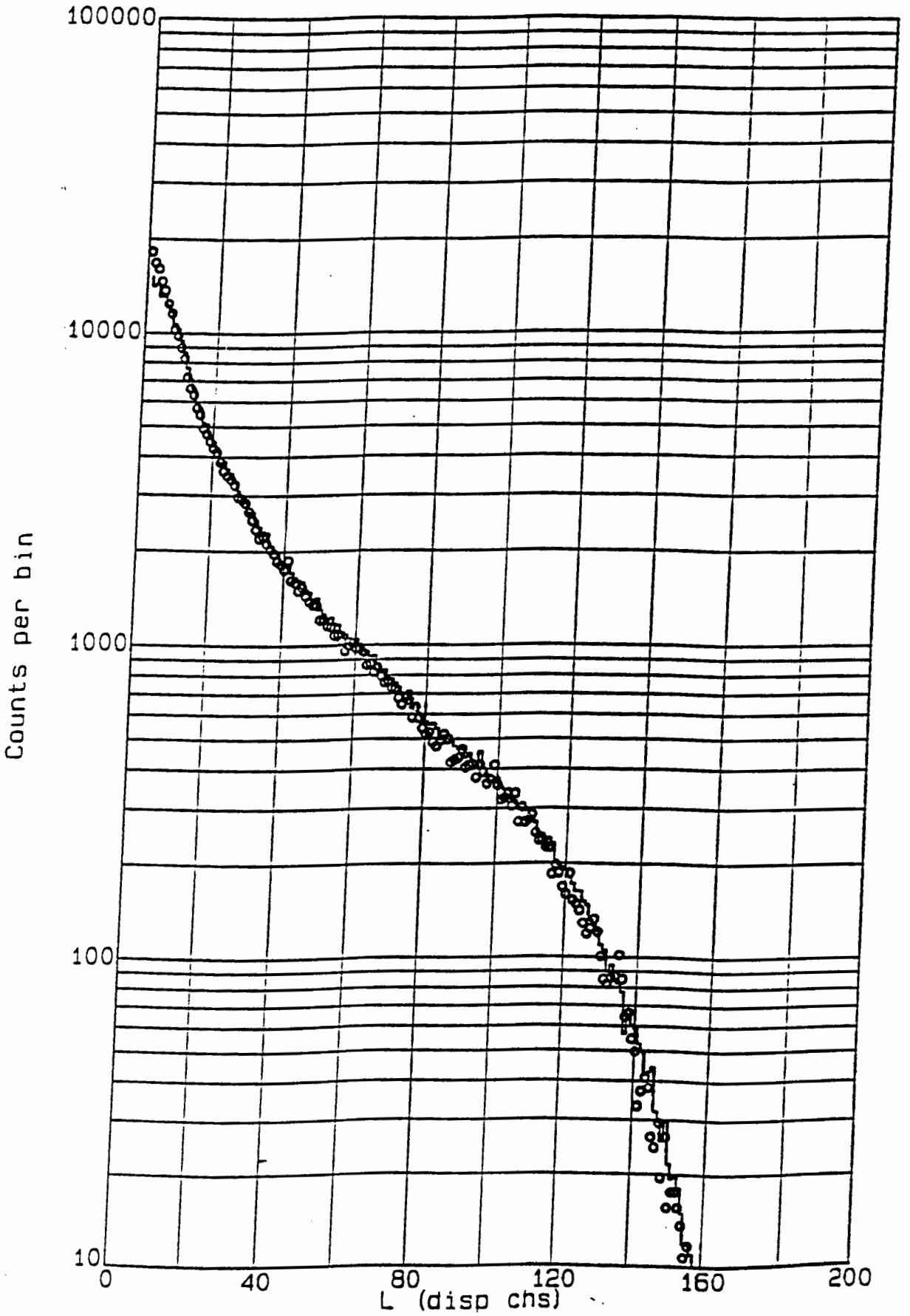

Figure 5.1.8 Comparison as in figure 5.1.1 for the spectrum measured at (d,x) = (36,0) cm for a = 29 cm with F1, F2.

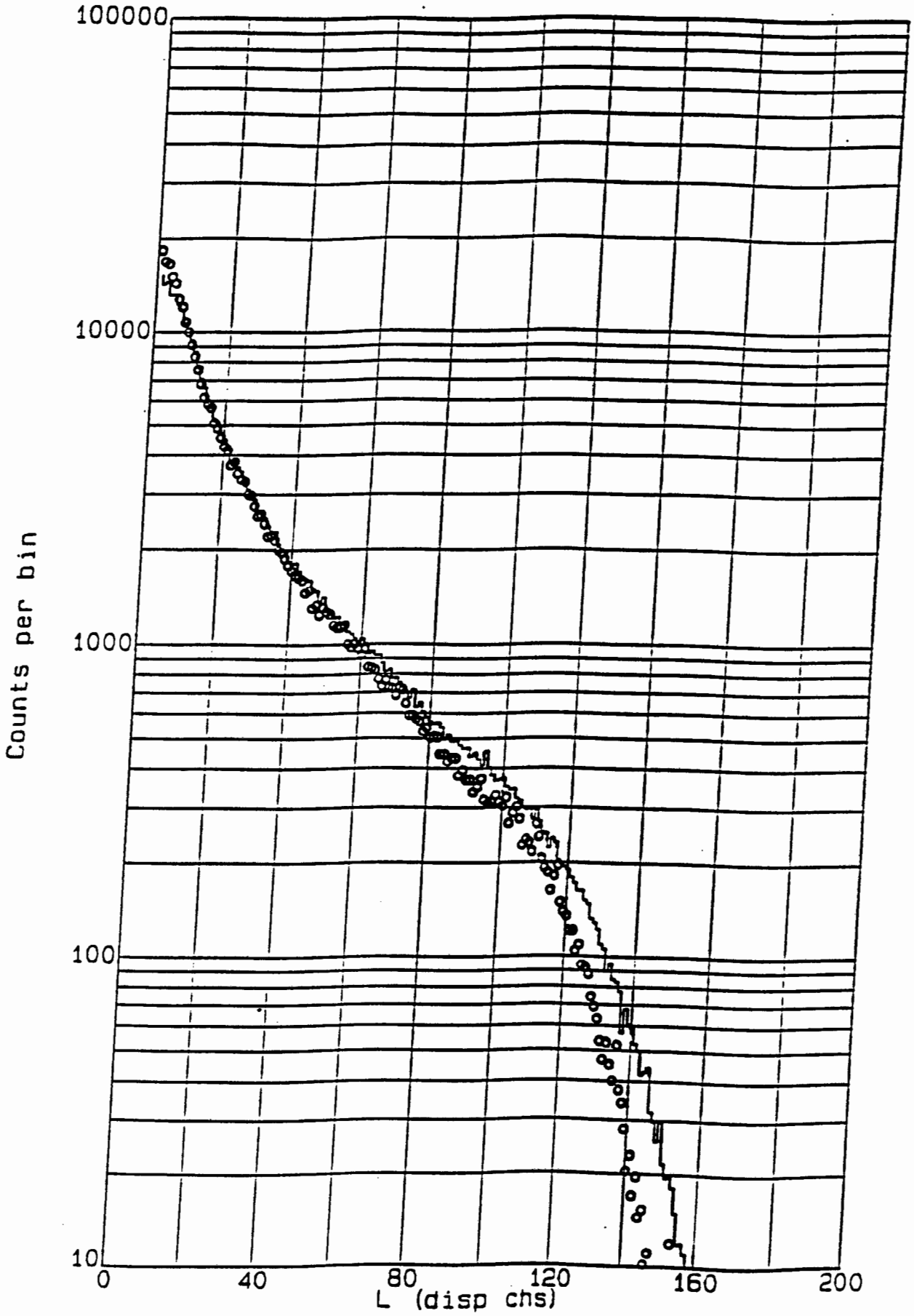

Figure 5.1.9 Comparison as in figure 5.1.1 for the spectrum measured at (d,x) = (8,0) cm for a = 10 cm with H, F1.

i = 1 to 200 channels for j = 1 to 18 energy bins defined in terms of the time of flight measurement for run 49, in other words 18 response functions at different neutron energies (see table II), each of 200 pulse height channels. The MIEKE analysis of a measured pulse height spectrum $L_K(i)$, for i = 1 to 200, for run K, determines the set of energy bin values, $\Phi(j)$, for j = 1 to 18 energy bins, of the neutron spectrum ,$\Phi_K(E_n)$, such that the calculated $M_K(i)$ is a "best fit" to $L_K(i)$ (see section 2.1). The spectrum derived for each run, K, have been normalised to the same total number of counts to that in the spectrum of run 49, to facilitate comparisons between the spectra. The normalised spectrum for run, K, was calculated using

$$N_K(i) = F_K \sum_{j=1}^{R} \Phi_K(j) R(i,j) \qquad (5.1)$$

where F_K is the normalising factor required to normalise the total number of counts in spectrum K to that in spectrum 49.

5.2.1 MIEKE ANALYSIS NUMBER 1

The chi-squared, χ^2, per degree of freedom and normalised factors, F_K, calculated for the neutron spectra derived using MIEKE analysis, for the different runs are displayed in table V. The chi-squared per degree of freedom values indicates that the neutron spectra derived using MIEKE analysis for runs K = 52-61 are reasonably compatible with the measured data used to derive them. Figures 5.2.1-5.2.9 show the normalised neutron spectra, N(i), determined for runs K = 52-61. In each figure N(i) is shown by solid squares and the open beam spectrum, are shown, for comparison, by

TABLE V. The chi-squared per degrees of freedom values and the normalised factors determined for the unfolded spectra in the phantom using MIEKE analysis number 1.

K	χ^2/dof	F_K
49	4.55	1.00
52	3.75	1.58
53	3.93	1.83
54	4.39	1.93
55	3.96	1.89
56	3.99	1.96
57	4.18	1.98
59	4.12	2.10
60	3.46	2.20
61	3.23	1.92

histogram. The spectra for the runs in the phantom show some systematic fluctuations from the open beam spectrum in the lower energy region, but in the high energy region the fluctuations were more excessive which are difficult to accept as realistic indicators of changes in the shape of the neutron spectra. In particular it is seen that $N_K(i) \approx 0$, for j = 2, 6 and 15 in every spectrum for run K = 52-61. These deep minima are unlikely to be valid features of the neutron spectra in the phantom and are probably artifacts associated with instabilities in the experiment, the data reduction before unfolding, or the unfolding process itself.

If we attribute these artifacts to instabilities in the experiment, or to the data reduction before unfolding, we need to consider the distortions which protons and alphas can introduce in the determined response matrix and the measured deuteron pulse height spectrum (see

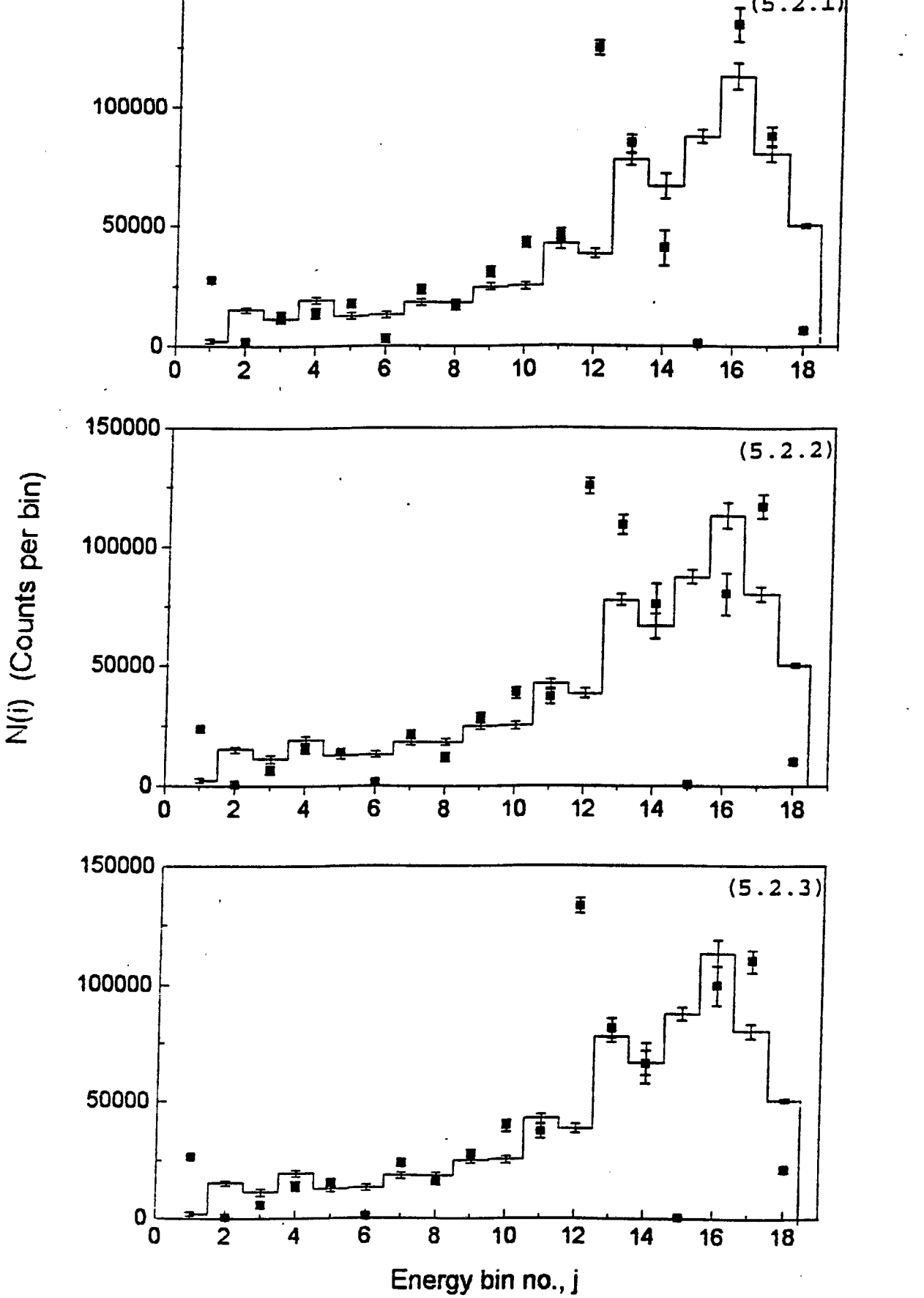

Figures 5.2.1-5.2.3 The neutron spectrum derived for the open beam (histogram) compared with spectra derived (solid squares) in the phantom at positions, (d,x) = (8,0) cm (5.2.1), (15,0) cm (5.2.2) and (22,0) cm (5.2.3) for a = 10 cm with F1. All the spectra were derived by MIEKE analysis.

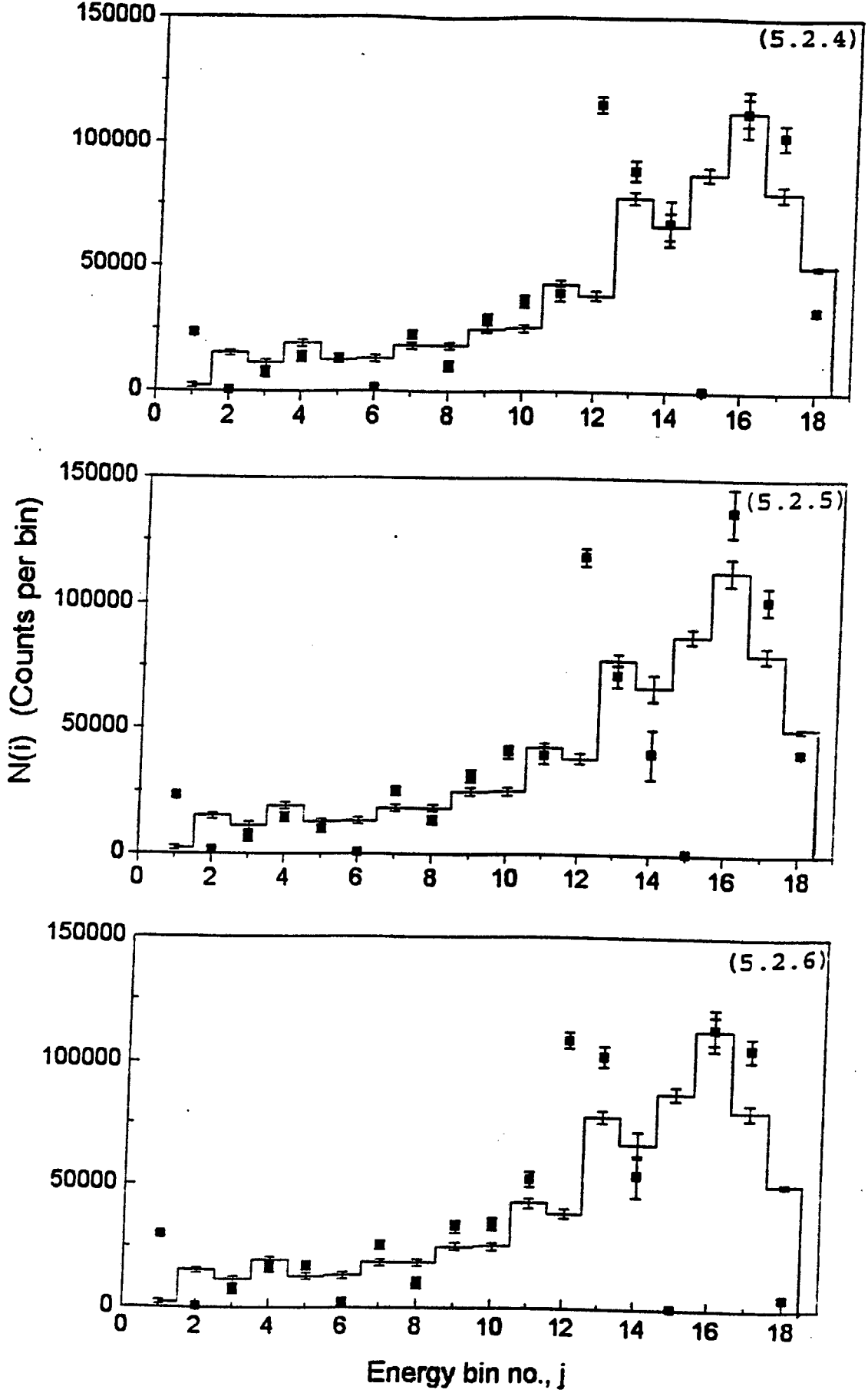

Figures 5.2.4-5.4.6 Comparisons as in figures 5.2.1- 5.2.3 for the spectra at (d,x) = (29,0) cm (5.2.4) and (36,0) cm (5.2.5) for a = 10 cm with F1. Also at (8,0) cm (5.2.6) for a = 29 cm with F1, F2.

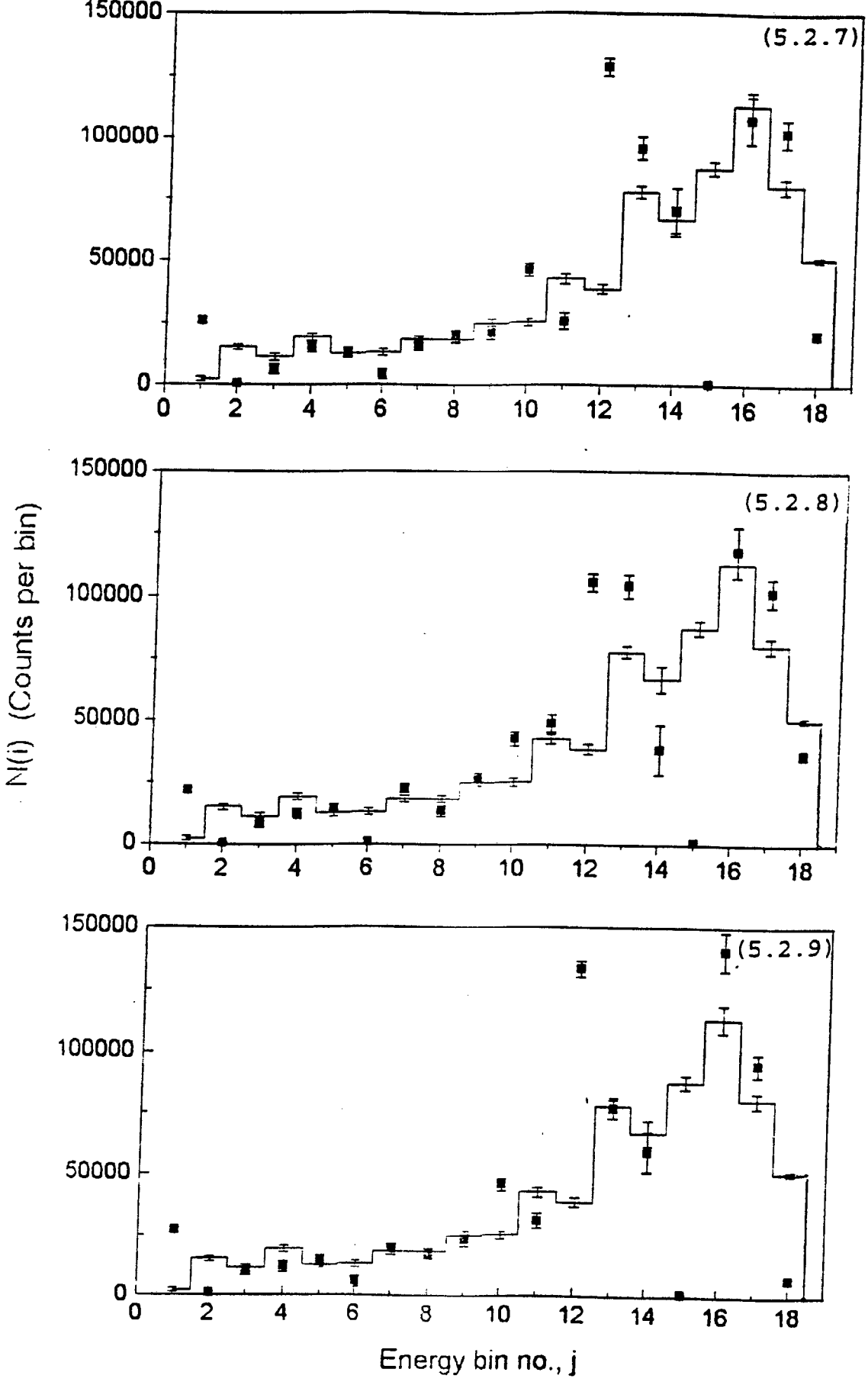

Figures 5.2.7-5.2.9 Comparisons as in figures 5.2.1-5.2.3 for the spectra at (d,x) = (22,0) cm (5.2.7) and (36,0) cm (5.2.8) for a = 29 cm with F1, F2. Also at (8,0) cm (5.2.9) for a = 10 cm with H, F1.

section 2.4). As pointed out in Section 4.1.3 figure 4.1 shows that at low pulse heights (channels 0 to 20) the counts per pulse height bin is much higher for energy bin 11 to 17 than those for bins 1 to 10 and 18. This may result from the fact that at low pulse height pulse shape discrimination is less effective in separating proton, alpha and deuteron events, because of poorer photomultiplier statistics. Protons and alphas which are not excluded by the deuteron cut (section 3.3) may contribute significantly to the lower region of the projected pulse height spectra which are subjected to MIEKE analysis. The proton contribution could include some externally incident protons, recoils from neutron scattering in the water which penetrate the light proof cover and glass capsule surrounding the NE230 scintillator. This contribution to the pulse height spectrum might interfere with the MIEKE analysis in an unpredictable manner.

It was therefore decided to carry out an additional MIEKE analysis modified in a way which might avoid or diminish this type of problem.

5.2.2 MIEKE ANALYSIS NUMBER 2

The modified MIEKE analysis, excluded the lower pulse height region (the first 18 pulse height channels) in order to avoid problems of the type just outlined (section 5.2.1). This change also implied an increase in the threshold neutron energy corresponding to the removal of energy groups 1-4 (the first 4 columns, of the response matrix) of the initial MIEKE analysis. Also the first 18 channels (of 200) of each column of the modified response matrix and in phantom runs were

removed. The response matrix now had 14 columns instead of 18 columns and formed now a 182x14 matrix. The MIEKE analysis was repeated using this response matrix and the pulse height spectra measured in the phantom with the first 18 channels of the spectra removed. Table VI displays the chi-squared, χ^2, per degree of freedom values and normalised factors, F_K, calculated for the neutron spectra derived using MIEKE analysis number 2.

TABLE VI. The chi-squared per degrees of freedom values and the normalised factors determined for the unfolded spectra in the phantom, using MIEKE analysis number 2

K	χ^2/dof	F_K
49	3.54	1.00
52	3.32	1.76
53	3.57	2.02
54	3.70	2.08
55	3.59	1.99
56	3.73	2.02
57	3,65	2.20
59	2.61	2.28
60	3.00	2.32
61	2.93	2.09

These chi-squared per degree of freedom values indicates that the neutron spectra derived using MIEKE analysis number 2 for runs K = 52-61 are more compatible with the measured data used to derive them than in the MIEKE analysis number 1. The results obtained are again plotted as in the MIEKE analysis number 1 and are shown in the plots in figures 5.3.1-5.3.9. The results show that the spectra for all the runs in the phantom have similar shape to the open beam

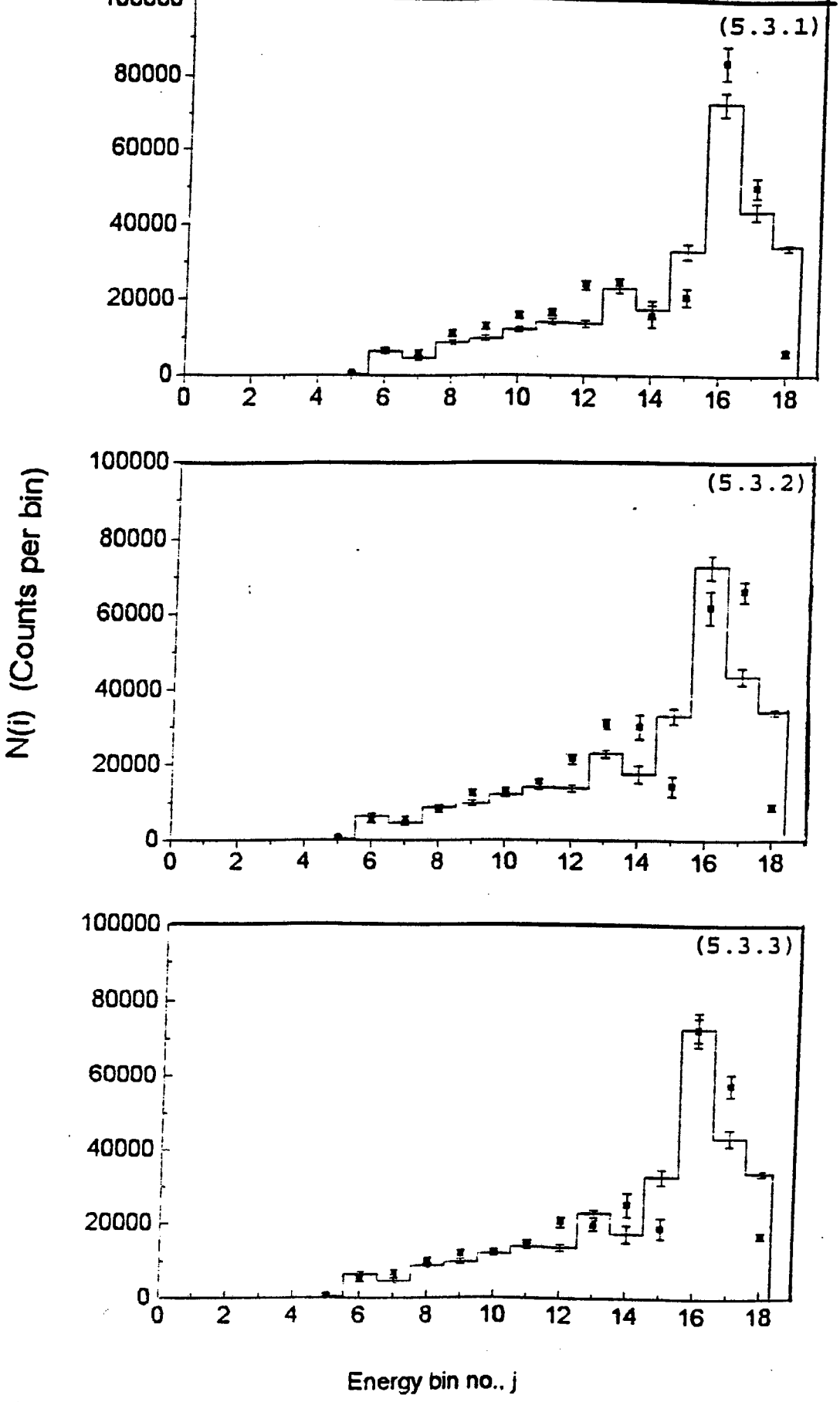

Figures 5.3.1-5.3.3 The neutron spectrum derived for the open beam (histogram) compared with spectra derived (solid squares) in the phantom at positions, (d,x) = (8,0) cm (5.3.1), (15,0) cm (5.3.2) and (22,0) cm (5.3.3) for a = 10 cm with F1. All the spectra were derived by MIEKE analysis.

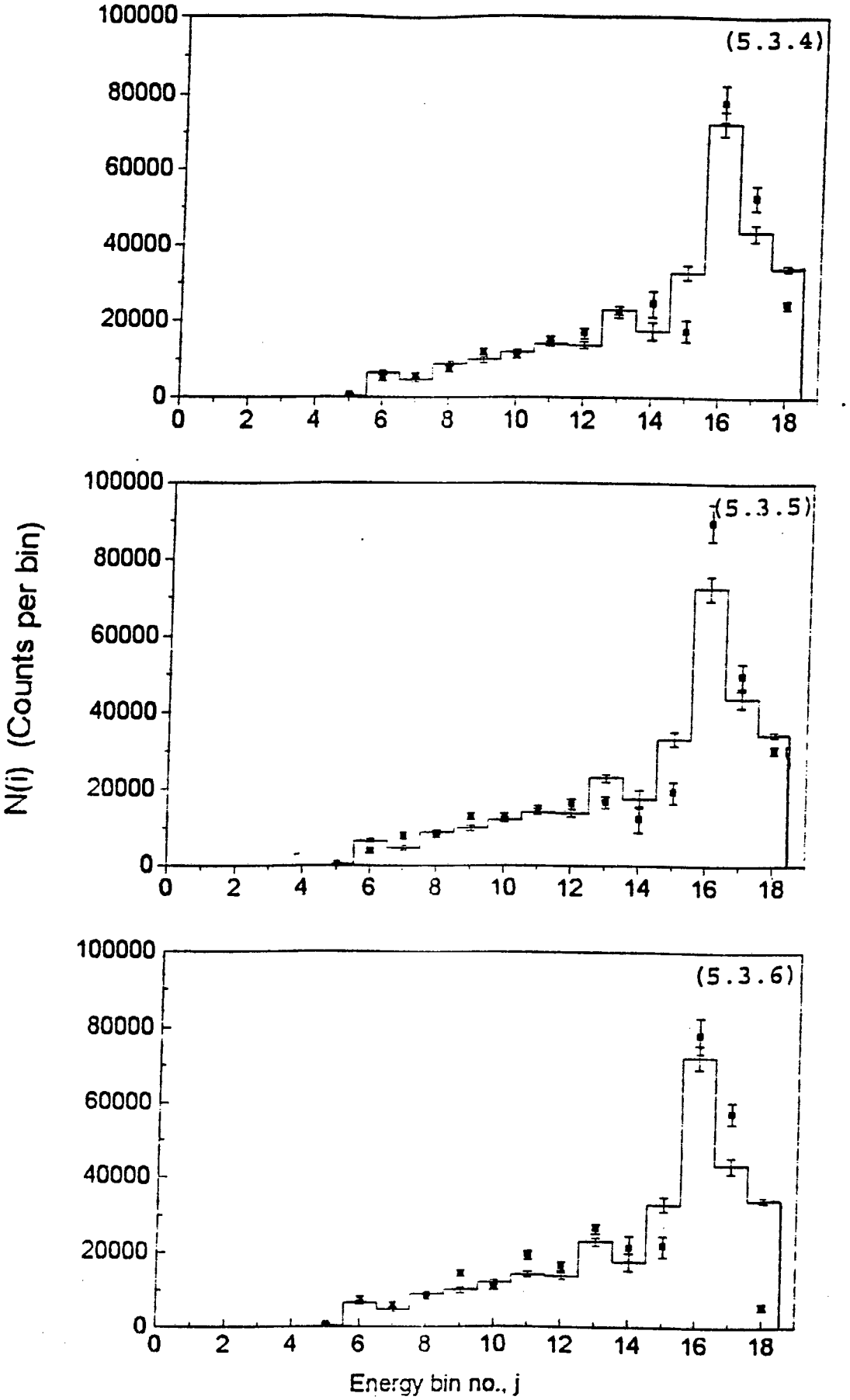

Figures 5.3.4-5.3.6 Comparisons as in figures 5.3.1- 5.3.3 for the spectra at (d,x) = (29,0) cm (5.3.4) and (36,0) cm (5.3.5) for a = 10 cm with F1. Also at (8,0) cm (5.3.6) for a = 29 cm with F1,F2.

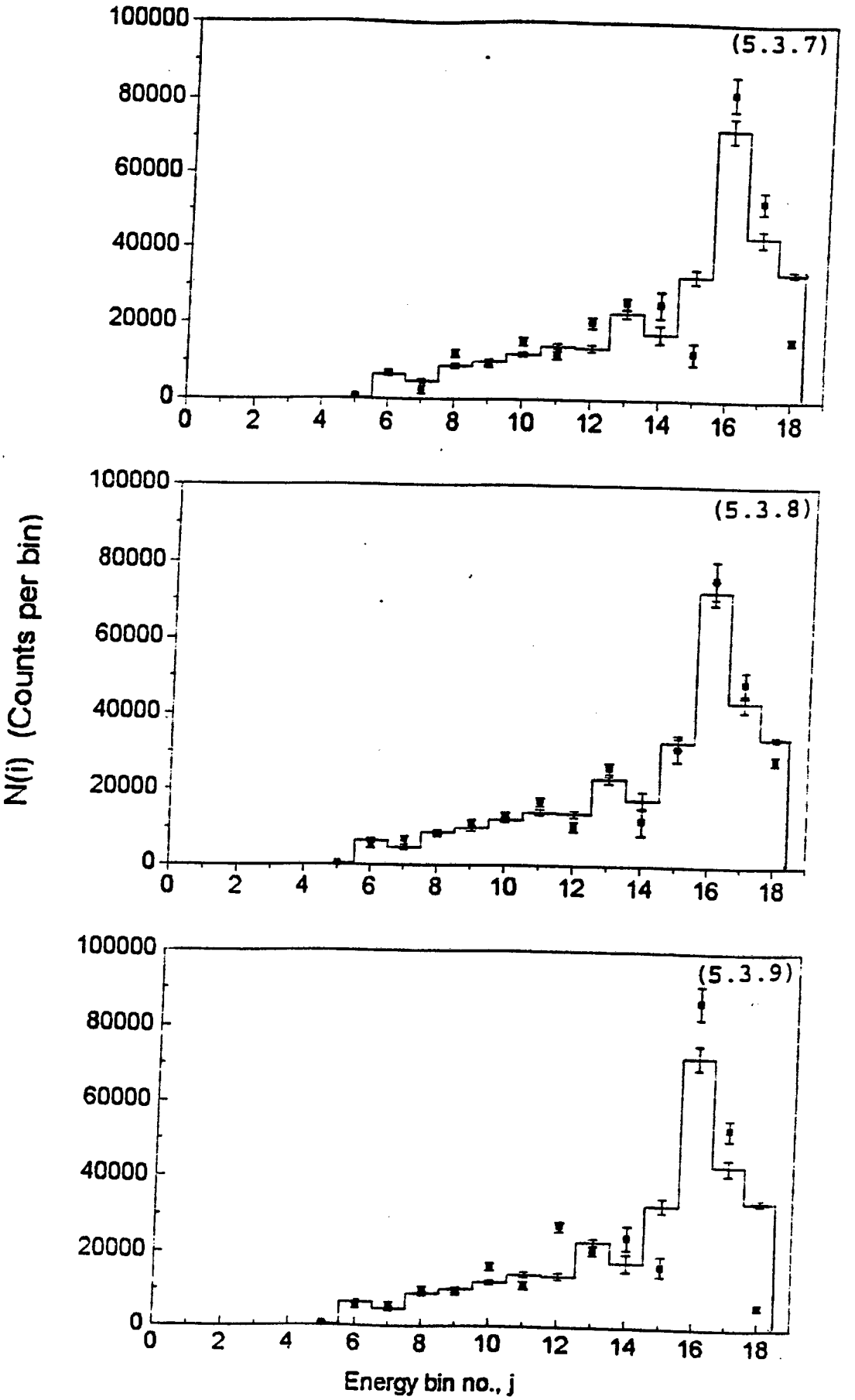

Figures 5.3.7-5.3.9 Comparisons as in figures 5.3.1-5.3.3 for the spectra at (d,x) = (22,0) cm (5.3.7) and (36,0) cm (5.3.8) for a = 29 cm with F1, F2. Also at (8,0) cm (5.3.9) for a = 10 cm with H, F1.

spectrum and that the deep minima at energy bins 2, 6 and 15 are removed from the spectra. It can also be seen in the figures that the excessive systematic fluctuations in the high energy region are much reduced. The results in figures 5.3.1-5.3.8 also shows similar changes as observed in the pulse height spectra (figures 5.1.1-5.1.8), that for both the 10x10 cm^2 and 29x29 cm^2 fields, that the "softening" of the beam spectrum diminishes with increasing depth, until at d = 36 cm it appears again to be very similar to the open beam spectrum.

Further investigation is needed to account for the systematic fluctuations observed in the neutron spectra, N(i). Since these systematic fluctuations are similar in all the N(i) spectra we may conclude that the changes observed in the shapes of the N(i) spectra are real.

5.3 RESULTS

5.3.1 VARIATION OF THE NEUTRON SPECTRUM WITH DEPTH ALONG THE BEAM AXIS INTO THE PHANTOM

Figure 5.4 shows comparisons between the neutron spectra measured for the open beam and at depths 8 cm and 36 cm along the beam axis into the phantom, using a 10x10 cm^2 field. The results for 15 cm, 22 cm and 29 cm are omitted for clarity, but fall between those shown. The results indicate that on entering 8 cm into the phantom, the proportion of low energy neutrons is increased, but with increasing depth, i.e. from 8 cm to 36 cm the proportion of low energy neutrons decreases while the proportion of high energy neutrons increases. This observation can be explained as follows. On

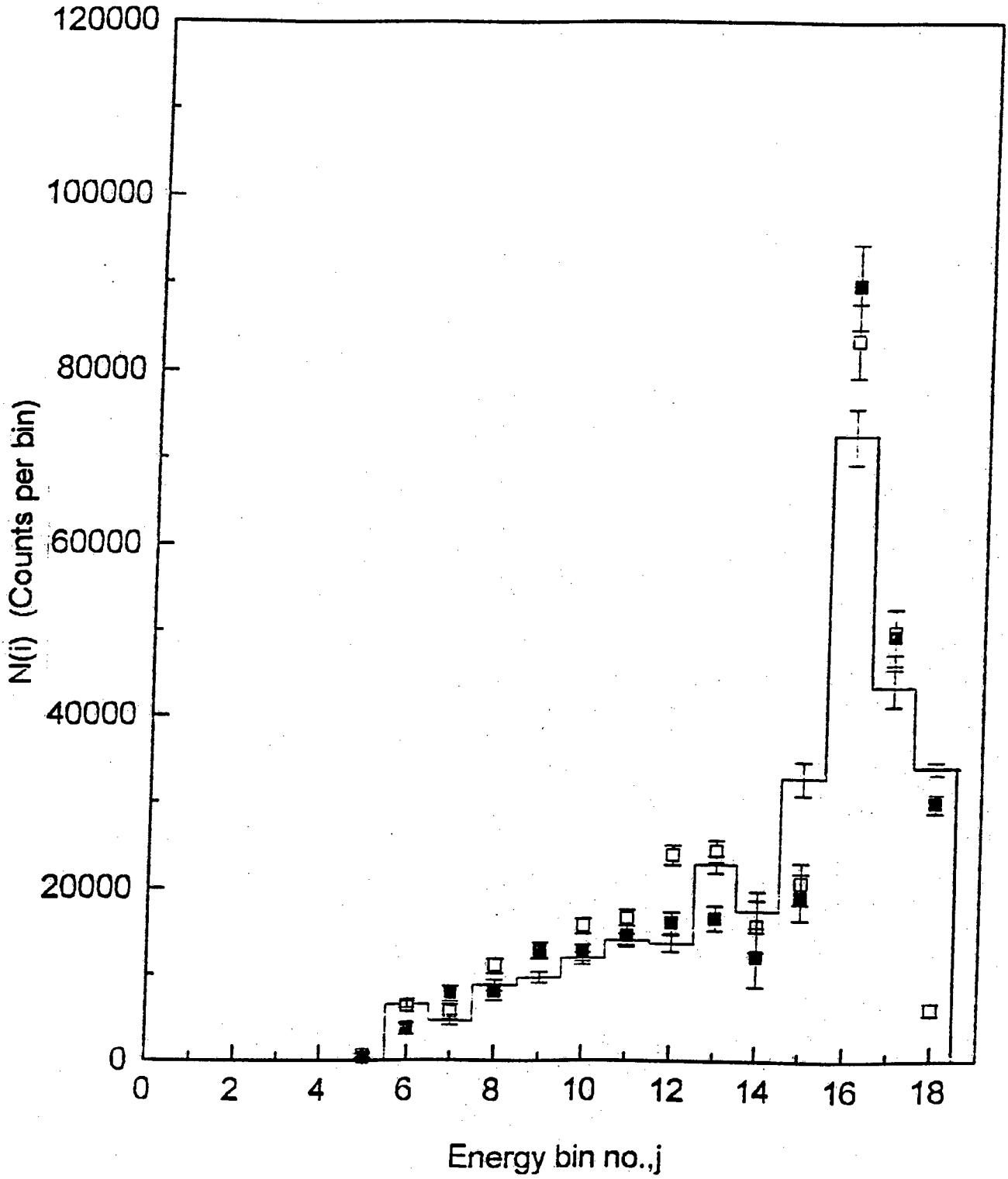

Figure 5.4 Neutron spectra measured in the open beam (histogram) and in the phantom at positions, (d,x) = (8,0) cm (open squares) and (36,0) cm (solid squares) for a = 10 cm with F1.

entering the phantom higher energy neutrons off beam axis are scattered towards the beam axis at lower energies, hence, the increase in the proportion of low energy neutrons. However, at greater depth into the phantom more low energy neutrons are scattered away from the beam axis than towards it because of the hydrogen neutron scattering cross-section decline with increasing neutron energy [Hu58], hence the increase in the proportion of high energy neutrons. The results show that with increasing depth into the phantom that the neutron spectrum hardens.

5.3.2 VARIATION OF THE NEUTRON SPECTRUM WITH FIELD SIZE ALONG THE BEAM AXIS INTO THE PHANTOM

Figures 5.5.1-5.5.2 show comparisons between the neutron spectra measured for the open beam and field sizes 10x10 cm^2 and 29x29 cm^2 at depths 8 cm and 36 cm along the beam axis into the phantom. The results shows again that the proportion of low energy neutrons in the spectra increased at depth 8cm into the phantom, but that the increase is greater in the spectrum of the 29x29 cm^2 field than in the spectrum of the 10x10 cm^2 field. The figures also show that with increasing depth into the phantom the increase in the proportion of high energy neutrons is greater in the spectrum of the 10x10 cm^2 field than for that in the spectrum of the 29x29 cm^2.

This observation can be explained using similar arguments as in Section 5.3.1. In this case the proportion of low energy neutrons at depth 8 cm scattered off beam axis towards the beam axis are greater for the 29x29 cm^2 field than for 10x10 cm^2 field, hence, the greater increase in the proportion of low energy

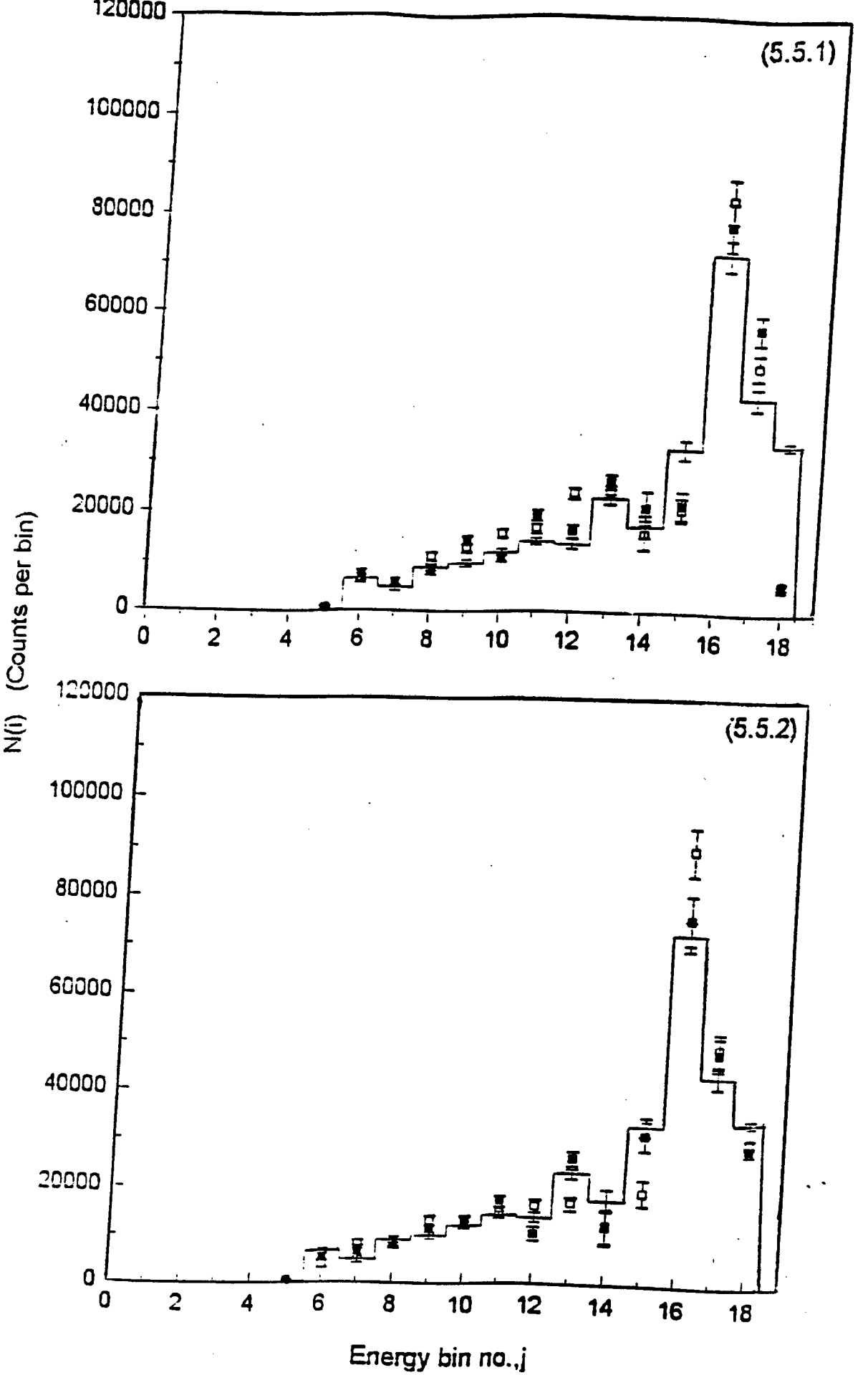

Figures 5.5.1-5.5.2 Neutron spectra measured in the open beam (histogram) and for a = 10 cm (open squares) and a = 29 cm (solid squares) at positions, (d,x) = (8,0) cm (5.5.1) and, (36,0) cm (5.5.2) cm in the phantom.

neutrons in the spectrum of the 29x29 cm^2 field. At depth 36 cm, a greater proportion of low energy neutrons are scattered away from the beam axis for the 29x29 cm^2 field than the for the 10x10 cm^2, hence, the smaller increase in the proportion of high energy neutrons in the spectrum of the 29x29 cm^2. The results do not show a significant difference in the spectra of the different fields, but it indicate that the degree of hardening is larger in the smaller field (10x10 cm^2) than in the larger field (29x29 cm^2) with increasing depth into the phantom.

5.3.3 VARIATION OF THE NEUTRON SPECTRUM WITH A BEAM FILTER ALONG THE BEAM AXIS INTO THE PHANTOM

Figure 5.6 shows a comparison between the measured spectra for the 10x10 cm^2 field made without and with a beam hardening filter at a depth 8 cm along the beam axis into phantom. The results indicate that the neutron spectrum hardens slightly with the beam filter. This is expected because the filter used preferentially filters out the lower energy neutrons.

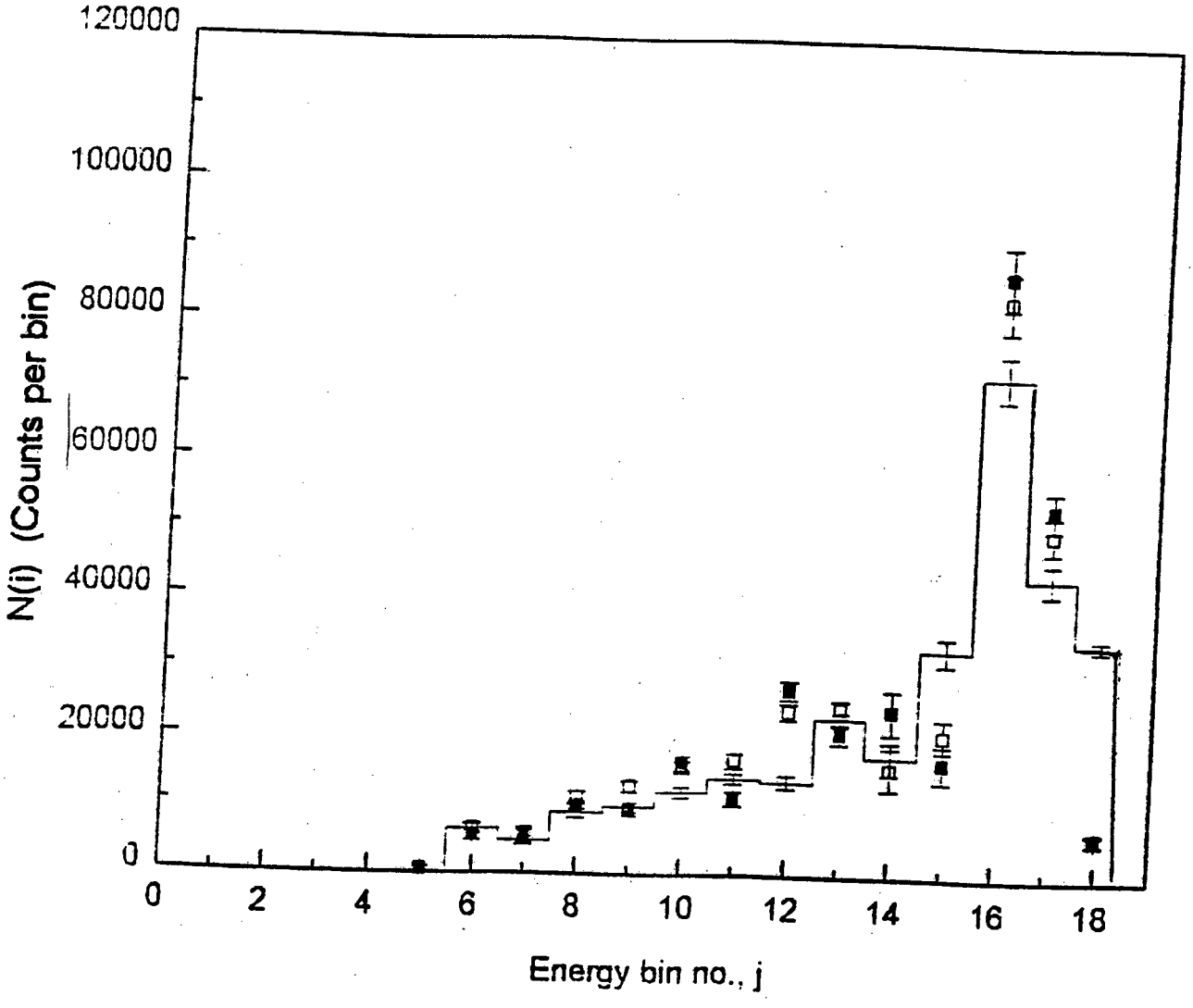

Figure 5.6 Neutron spectra measured in the open beam (histogram) and in the phantom and at positions, (d,x) = (8,0) cm for a = 10 cm with F1 (open squares) and H, F1 (solid squares).

CHAPTER 6

6 1 CONCLUSION

The pulse height spectrum measurements for the NE230 detector show that it can be use as neutron spectrometer to measure neutron spectra within a phantom. The tests performed on the HEPRO unfolding package, using the open beam data, demonstrated that the HEPRO unfolding package would be reliable to unfold neutron spectra from pulse height spectra.

The neutron energy spectra obtained using the HEPRO unfolding package from the projected pulse height as a function of position and also of other beam variables such as collimator settings (field size) and beam filter geometry in a water phantom (50x50x50 cm^3) indicated that:

(a) the neutron energy spectrum hardens with increasing depth into the phantom;

(b) the hardening is greater for the smaller field than for the larger field with increase in depth into the phantom; and

(c) that a hardening beam filter, hardens the neutron beam.

These results are consistent with the results obtained by other researchers [Jo92, Bo82 and Cr91]. These results show good prospects for the use of the NE230

detector as a neutron spectrometer for measurement of neutron spectra in a phantom. However, much still needs to be investigated, especially the factors which can lead to reducing the distortions in the neutron energy spectra.

6.2 FURTHER WORK

Most of the distortions in the measured neutron spectra are due to distortions in

(a) the response matrix used in the unfolding process; and
(b) the measured pulse height spectra .

It has been shown that these distortions may be due to high energy deuterons escaping through the wall of the detector or to errors in the response matrix. These errors appear to arise from the failure of the deuteron cut (see figure 3.4) to exclude protons at low pulse heights. The present work suggests that, in future work, the size of the detector needs to be reconsidered in order to reduce deuteron escapes through the detector walls. A better PSD cut could also be used to separate the deuterons from the protons and alphas at low pulse heights of the LS distribution. With these improvements the technique should be capable of verifying the reliability of neutron spectra determined by Monte Carlo calculations.

REFERENCES

Bi64 J.B. Birks, "Theory and practice of scintillation counting", Pergamon Press, (1964).

Be89 M. Beauduin, J. Gueulette, V. Gregoire, B. de Coster, S. Vynckier and I. Wambersie, EUR 12165 EN (CEC, Luxembourg 1989) pp. 101-135.

Bo72 E. Bovet, P. Boschung and J. Rossel, Nucl. Inst. and Meth 101 (1972) 315.

Bo78 D.E. Bonnet, PhD. Thesis, University of Birmingham (unpublished) 1978.

Bo82 D.E. Bonnet and C.J. Parnell, Br. J. Radiol. 55 (1982) 48.

Br79 F.D. Brooks, Nucl. Inst. and Meth 162 (1979) 477.

Bu90 A. Buffler, MSc Thesis, University of Cape Town (unpublished) 1990.

Bu93 L. Buermann, S. Ding, S. Guldbakke, H. Klein, T. Novotny and M. Tichy, Nucl. Inst. and Meth. A332 (1993) 483.

Bu97 A. Buffler, K. Bharuth-Ram, F.D. Brooks, M.S. Allie, M. Herbert, M.R.Nchodu, and B.R.S. Simpson, Proc. Int. Soc. Opt. Eng. 2867 (1997) 192.

Ca79 M. Catterall and D.K. Bewley, in "Fast Neutrons and the Treatment of Cancer", Academic Press, London, (1979).

Cr88 N.M.J. Crout, J.G. Fletcher and M.C. Scott, Radiat. Prot. Dosim. 23 (1988) 381.

Cr91 N.M.J. Crout, J.G. Fletcher, S. Green, M.C. Scott, and G.C. Taylor, Phys. Med. Biol. 36 (1991) 507.

Cz70 J.B. Czirr, Nucl. Inst. and Meth 88 (1970) 321.

Di93 E. Dietz, M. Matzke, W. Sosaat, G. Urbach and M. Weyrauch, Nucl. Inst. and Meth. A232 (1993) 521.

Dy81 N.A. Dyson, Nuclear Physics with applications in Medicine and Biology, Ellishorwood Publishers, (1981).

Fi79 F.W.K Firk, Nucl. Inst. and Meth 162 (1979) 539.

Gr57 L.H. Gray, Br. J. Radiol. 30 (1957) 403.

Hu58 D.J. Hughes and R.B. Schwartz, Brookhaven National Laboratory Report BNL 325 ICRU Microdosimetry Report 36 (Bethesda, MD:ICRU 1983).

Ja57 E.T. Jaynes, Phys. Rev 106 (1957) 620.

Jo92 D.T.L. Jones, J.E. Symons, T.J. Fulcher, F.D. Brooks, M.R. Nchodu, M.S. Allie, A. Buffler and M.J. Oliver. J. Med. Phys 19 (1992) 1285.

Kn89 G.F. Knoll, Radiation Detection and Measurement, second edition, John Wiley and sons (1989).

Le89 M.L. Lee, "Bayesian statistics: an introduction" Oxford Univerrsity Press: New York (1989)

Ma86 R.E. Maerker, B.L. Broadhead and J.J. Wagschal, Nucl. Sci. Eng. 91 (1986) 137.

Ma88 M.Matzke, Rad. Prot. Dosim. 23 (1988) 297.

Ma94 M. Matzke, "Unfolding of pulse height spectra: the HEPRO program system", Report PTB-N-19, Physikalisch-Technische Bundesanstalt, Braunschweig, 1994.

MC67 W.N. McElroy, S. Berg, T. Crockett and R.G. Hawkins, "A computer-automated iterative method for neutron flux spectra determination by foil activation, SAND-II, "Report AFWL-TR-67-41, U.S. Air Force Weapons Laboratory, 1967.

Mo90 M.F. Moyers and J.L. Horton, Med. Phys. 17 (1990) 607.

Nac87 Annual Report of the National Accelerator Centre, Faure, South Africa (1987)

Nc93 M.R. Nchodu, MSc Thesis, University of Cape Town (unpublished) 1993

NE Table of Physical Constants of Scintillators, previously available from NUCLEAR ENTERPRISES Technology Limited, Sighthill, Edinburg, Scotland, EH11 4BY.

Pa72 C.J. Parnell, Br. J. Radiol. 45 (1972) 452.

Ra80 M.R. Raju, Heavy Particle Radiotherapy, Academic Press, (1980).

Ro80 J.T. Routti and J.V. Sandberg, "General purpose unfolding program LOUHI78", Comput. Phys. Comm. 21 (1980) 119.

Sc81 M.C. Scott, J.W. Bennett and J.S. Petler, Proc. 4th Symp. Neutron Dosimetry, 2 (1981) 167.

Sm68 D.L. Smith, R.G. Polk and T.G. Miller, Nucl. Inst. and Meth. 64 (1968) 157.

Sm86 F.D. Smit, neutrons in PhD Thesis, University of Cape Town (unpublished) 1986

Sh71 G.E. Shelin, T.L Phillips, S.B. Field, J.T. Brennan, and A. Raventos, Am. J. Roentgen, 111 (1971) 31.

St40 R.S. Stone, J.H. Lawrence and P.C. Aebersold, Radiology, 35 (1940) 322.

Ti93 M. Tichy, "The DIFBAS program, description and user's guide", Report PTB-7.2-93-1, Physikalisch-Technische Bundesanstalt, Braunscweig, 1993.

We89 K. Weise and M. Matzke, Nucl. Inst. and Meth A280 (1989) 103.

Wi93 J.R. Williams and D.I. Thuaites, Radiotherapy Physics, Oxford University Press, (1993).